CORSO DOTTORATO DI RICERCA IN

INGEGNERIA MECCANICA E INDUSTRIALE

XXX CICLO DEL CORSO DI DOTTORATO

State-Space Rotor Wake Inflow Modeling for Helicopter Aeromechanics

Dottorando: **Felice Cardito** _____

firma

Docente guida: **Prof. Massimo Gennaretti** _____

firma

Coordinatore: **Prof. Edoardo Bemporad** _____

firma

Contents

Contents ii

List of Symbols v

List of Figures vii

1 Introduction 1

1.1 State of the art: dynamic inflow modeling 3

1.2 Role of the dynamic inflow in helicopter modeling 7

1.3 Objectives and outline of the dissertation 9

2 Dynamic Wake Inflow in State Space Format 11

2.1 Inflow representation 11

2.2 Dynamic inflow models 15

2.2.1 Linear time invariant dynamic inflow model 15

2.2.2 Linear time periodic dynamic inflow model 17

2.3 Models extension to advanced rotor configuration: coaxial contra-rotating rotors 23

3 Dynamic Wake Inflow Models Extraction 26

3.1 Single frequency excitation method for linear time invariant transfer function extraction 27

3.2 Chirp excitation method for linear time invariant transfer function extraction 28

3.3 Extended single frequency excitation method to linear time periodic transfer function extraction 32
3.4 Extended chirp-based excitation method to linear time periodic transfer function extraction 33

4 Numerical results **36**
4.1 Approximated representation of wake inflow 38
4.2 Linear Time Invariant models 46
4.2.1 Time marching validation for kinematic and load based models . 74
4.3 Linear Time Periodic models 85
4.3.1 Time marching validation 88
4.4 Flight mechanics simulation results 99
4.4.1 Helicopter aeromechanics 99

Concluding remarks **104**

Appendix **107**
A. Nonlinear, separable-variable least-square approach for RMA 107
B. High-fidelity rotor aerodynamic solver 109
C. Flight mechanics simulation tool with the inclusion of dynamic inflow models from high fidelity aerodynamic solver 110
Kinematic-based inflow 111
Load-based inflow 112

Bibliography **113**

List of Symbols

$\boldsymbol{A}_1, \boldsymbol{A}_0, \boldsymbol{A}, \boldsymbol{B}, \boldsymbol{C}$	=	matrices of the rational-matrix approximation
C_T, C_L, C_M	=	thrust, rolling moment and pitching moment coefficient perturbations
$C(k)$	=	Theodorsen lift deficiency function
G	=	Green function
$\boldsymbol{G}_v, \boldsymbol{G}_\Omega, \boldsymbol{G}_\theta, \boldsymbol{G}_\beta$	=	linear time invariant transfer function matrices: kinematic perturbations vs rotor loads
$\boldsymbol{H}, \boldsymbol{H}_v, \boldsymbol{H}_\Omega, \boldsymbol{H}_\theta, \boldsymbol{H}_\beta$	=	linear time invariant transfer function matrices: kinematic perturbations vs wake inflow coefficients
$\hat{\boldsymbol{H}}_v, \hat{\boldsymbol{H}}_\Omega, \hat{\boldsymbol{H}}_\theta, \hat{\boldsymbol{H}}_\beta$	=	linear time invariant transfer function matrices: rotor loads vs wake inflow coefficients
$\boldsymbol{L}$	=	derivative matrix
$\boldsymbol{M}$	=	mass matrix
$\boldsymbol{MH}$	=	harmonic transfer function matrix: kinematic and elastic degrees of freedom vs Fourier series wake inflow coefficients
P_n^m, Q_n^m	=	normalized Legendre function of the first kind
$\boldsymbol{q}, \boldsymbol{q}_v, \boldsymbol{q}_\Omega, \boldsymbol{q}_\theta, \boldsymbol{q}_\beta$	=	vectors of kinematic perturbations
(r, ψ)	=	system of polar coordinates on the rotor disc
R, r_c	=	rotor radius and root aerodynamic cut-off
$\boldsymbol{r}$	=	wake inflow dynamics states
s	=	Laplace-domain variable
v_B	=	wake inflow perturbation evaluated on a rotor blade
v_i	=	approximated wake inflow perturbation distribution on rotor disc

$v_0, v_s, v_c, v_{N/2}$	=	wake inflow multiblade coefficients
$v^n_{1/2}, v^n_{3/4}$	=	normal velocity component evaluated at airfoil mid point and at 3/4 chord point
$\lambda_{0,j}, \lambda_{c,j}, \lambda_{s,j}, \lambda_{N/2,j}$	=	wake inflow components
$\lambda^0_{\alpha,j}, \lambda^{ks}_{\alpha,j}, \lambda^{kc}_{\alpha,j}$	=	Fourier series wake inflow coefficients
$\boldsymbol{\lambda}$	=	vector of wake inflow components
$\phi^0_j, \phi^c_j, \phi^s_j, \phi^{N/2}_j$	=	radial basis functions
χ	=	wake skew angle
$\vec{n}$	=	unit vector orthogonal to the blade surface
$\vec{u}_I$	=	velocity induced by the far wake
$\vec{v}, \vec{v}_B$	=	flow and blade velocities
$\vec{x}, \vec{y}$	=	observer and source positions
S_B, S^N_W, S^F_W	=	blade surface, near wake surface and far wake surface
ρ	=	air density
ϕ, ϕ_I, ϕ_S	=	total, incident and scattered velocity potential

List of Figures

1.1 General work-flow sketch for the typical use of the dynamic inflow model. . 9

2.1 Spectrum of the computed inflow v_B at radial station $0.7R$ and $\psi = \pi/2$ response to harmonic θ_c perturbation. Forward flight condition. 14

2.2 Spectrum of inflow coefficients at radial station $0.7R$ and $\psi = \pi/2$ response to harmonic θ_c perturbation. Forward flight condition. 14

2.3 Correlation of spectra between the computed inflow ● v_B and its approximation v_i w/o —/— differential coefficient, at radial station $0.7R$ and $\psi = \pi/2$ response to harmonic θ_c perturbation 15

3.1 Example of linear and quadratic chirp signal and their spectrogram, with a frequency band from 0 to 32 Hz 30

3.2 Example of quadratic chirp signal with a frequency band from 0 to 32 Hz . 31

4.1 Distribution of wake inflow perturbations on blades at $\psi = \pi/2$. — v_B, - - - v_i Hovering Condition. 39

4.2 Distribution of wake inflow perturbations, v_B, on blades at $\psi = \pi/2$. — upper rotor — lower rotor. Hovering condition. 40

4.3 Distribution of wake inflow perturbations, $v_B^{u,l}$ over coaxial rotor discs. Hovering Condition. 41

4.4 Distribution of wake inflow perturbations, v_B, over coaxial rotor discs. Forward flight condition. 42

4.5 Distribution of wake inflow perturbations —— v_B on blades at $\psi = \pi/2$ and its approximation v_i - - - present model considering four identical shape functions of the inflow coefficients -·-·- Pitt-Peters like (left). Spanwise error distribution (right). Hovering Condition. 43

4.6 Distribution of wake inflow perturbations v_B —— upper rotor —— lower rotor on blades at $\psi = \pi/2$ and its approximation $v_i^{u,l}$(- - - present model considering four identical shape functions of the inflow coefficients -·-·- Pitt-Peters like) **(top)**. Spanwise error distribution **(bottom)**. 44

4.7 Distribution of wake inflow perturbations, v_B **(top)**, and its approximation considering four identical shape functions of the inflow coefficients $v_i^{u,l}$ **(bottom)** over coaxial rotor discs. Forward flight condition. 45

4.8 Transfer functions between velocity kinematic variables and inflow coefficients. Hovering condition. —— RMA, ● sample. 47

4.9 Transfer functions between blade pitch controls and inflow coefficients. —— $\mathbf{H}_\theta$, —— $\mathbf{H}_\theta^L$, ——$\mathbf{H}_\theta^F$. Hover. 48

4.10 Power coherence of identification of transfer functions between blade pitch controls and inflow coefficients. ● $\mathbf{H}_\theta$, ■ $\mathbf{H}_\theta^L$, ♦ $\mathbf{H}_\theta^F$. Hover. 49

4.11 Transfer functions between blade pitch control variables and wake inflow components. Hovering condition —— RMA upper rotor —— RMA lower rotor, ● samples. 51

4.12 Transfer functions between hub kinematic variables and wake inflow components. Hovering condition —— RMA upper rotor, —— RMA lower rotor, ● samples. 52

4.13 Transfer functions between blade pitch control variables and wake inflow components, for hovering condition, free-wake analysis —— RMA upper rotor —— RMA lower rotor, ● samples. 54

4.14 Transfer functions between blade pitch controls and λ_0 . Forward flight . . 55

4.15 Transfer functions between blade pitch controls and λ_s . Forward flight . . . 56

4.16 Transfer functions between blade pitch controls and λ_c . Forward flight . . . 57

4.17 Power coherence of identification of transfer functions between blade pitch controls and inflow coefficients. ● λ_0, ♦ λ_s, ■ λ_c. Forward flight 58

4.18 Transfer functions between blade pitch control variables and wake inflow components, forward flight condition, —— RMA upper rotor —— RMA lower rotor, ● samples. 60

4.19 Transfer functions between blade pitch control variables and rotor hub loads, hovering condition. Single rotor configuration. Free wake analysis. 62

4.20 Transfer function λ_0 vs C_T : load based approach $\hat{\mathbf{H}}_\theta$, $\hat{\mathbf{H}}_V$,$\hat{\mathbf{H}}_\beta$,$\hat{\mathbf{H}}_\Omega$ compared with Pitt-Peters'one —— 63

4.21 Transfer functions evaluated by load based approach $\hat{\mathbf{H}}_\theta$, $\hat{\mathbf{H}}_V$, $\hat{\mathbf{H}}_\beta$, $\hat{\mathbf{H}}_\Omega$, and comparison with Pitt-Peters model 64

4.22 Wake shape effect on identified Pitt-Peters-like transfer functions. $\hat{\mathbf{H}}_\theta$, $\hat{\mathbf{H}}_\theta^L$, $\hat{\mathbf{H}}_\theta^F$ 66

4.23 Transfer functions evaluated by load based approach $\hat{\mathbf{H}}_\theta$, $\hat{\mathbf{H}}_V$, $\hat{\mathbf{H}}_\beta$, $\hat{\mathbf{H}}_\Omega$, and comparison with Pitt-Peters model 67

4.24 Transfer functions evaluated by load based approach, hovering condition., —— RMA upper rotor —— RMA lower rotor, ● samples. 69

4.25 Transfer functions between rotor loads and λ_0 and comparison with Pitt-Peters model. Forward flight condition. —— RMA , ● samples. 70

4.26 Transfer functions between rotor loads and λ_s and comparison with Pitt-Peters model. Forward flight condition. —— RMA , ● samples. 71

4.27 Transfer functions between rotor loads and λ_c and comparison with Pitt-Peters model. Forward flight condition. —— RMA , ● samples. 72

4.28 Transfer functions between rotor loads and inflow coefficients. Forward flight condition. —— RMA upper rotor —— RMA lower rotor, ● samples. 73

4.29 Time response to perturbations. Hovering condition. Correlation among BEM simulations and predictions given by the $\lambda - q$ state-space model. ● BEM; —— state-space model. 75

4.30 Time response to perturbations. Hovering condition. Correlation among BEM simulations and predictions given by the $\lambda - f$ state-space models. ● BEM; —— $\hat{\mathbf{H}}_\theta$; - - - - $\hat{\mathbf{H}}_V$; - - - $\hat{\mathbf{H}}_\Omega$ 76

4.31 Time response and correlation of spectra response to θ_c^+ perturbation. Hovering condition. Correlation among BEM simulations and predictions given by the $\lambda - q$ state-space model. ● BEM; —— upper rotor —— lower rotor state space model 77

4.32 Time response and correlation of spectra response to θ_c^+ perturbation. Hovering condition. Correlation among BEM simulations and predictions given by the $\lambda - f$ state-space models. ● BEM; —— upper rotor —— lower rotor $\hat{\mathbf{H}}_\theta$; - - - - upper rotor - - - lower rotor $\hat{\mathbf{H}}_{\Omega_V}$ 78

4.33 Time response to θ_c^+ perturbation. Hovering condition, free wake analysis. Correlation among BEM simulations and predictions given by the $\lambda - q$ state-space model. ● BEM; —— upper rotor —— lower rotor state space model 80

4.34 Correlation of spectra response to θ_c^+ perturbation. Hovering condition. Correlation among BEM simulations and predictions given by the $\lambda - q$ state-space model. ● BEM; —— upper rotor —— lower rotor state space model. Vertical lines indicate the $0.2/rev$ and $0.4/rev$ harmonics of Eq. 4.2 81

4.35 Time response and correlation of spectra response to θ_c^+ perturbation. Hovering condition. Correlation among BEM simulations and prediction given by $\lambda - f$ state-space model. ● BEM; —— upper rotor —— lower rotor state space model. Vertical lines indicate the $0.2/rev$ and $0.4/rev$ harmonics of Eq. 4.2 82

4.36 Time response to θ_c^+ perturbation. Forward flight condition. Correlation among BEM simulations and predictions given by the state-space models. ● BEM; —— state-space model. 83

4.37 Time response to θ_c^+ perturbation. Forward flight condition. Correlation among BEM simulations and predictions given by the state-space models. ● BEM; —— upper rotor —— lower rotor state space model 84

4.38 Transfer functions between blade pitch control and inflow coefficients. ● samples; —— RMA 86

4.39 Transfer function $\lambda_1^{0,0}$ vs θ_0. Hovering condition. ● samples —— RMA upper rotor, —— RMA lower rotor. 87

4.40 Transfer functions between blade pitch control and inflow coefficients. Forward flight condition. ● BEM; —— RMA 87

4.41 Transfer function $\lambda_3^{0,0}$ vs θ_0. Forward flight condition. ● samples —— RMA upper rotor, —— RMA lower rotor. 88

4.42 Wake inflow response at $r/R = 0.74$ **(top)**, $r/R = 0.9$, $r/R = 0.97$ **(bottom)** to θ_0 perturbation. Hovering condition. Correlation among BEM simulation and prediction given by state space models. ● BEM, —— state space present model, —— state space linear Pitt-Peters like 89

4.43 Spanwise error distribution. Hovering condition. —— present model, —— linear Pitt-Peters like 90

4.44 Wake inflow response at $r/R = 0.41$ **(top)**, $r/R = 0.62$, $r/R = 0.95$ **(bottom)** to θ_0^+ perturbation. Hovering condition. Correlation among BEM simulation and prediction given by state space models. ● BEM —— upper rotor state space present model, - - - - upper rotor state space Pitt-Peters like, —— lower rotor state space present model, - · - · lower rotor state space Pitt-Peters like 91

4.45 Spanwise error distribution for hovering condition. —— present model upper rotor, - - - - Pitt-Peters like upper rotor, —— present model lower rotor, - · - · Pitt-Peters like lower rotor 92

4.46 Time response to β_0 perturbation. Forward flight condition. Correlation among BEM simulations and state-space model. ● BEM, —— present model state space. 93

4.47 Correlation of spectra response to β_0 perturbation. Forward flight condition. Correlation among BEM simulations and prediction by the state-space model. ● BEM, —— present model state space. 93

4.48 Wake inflow response ar $r/R = 0.54$**(top)**, $r/R = 0.72$, $r/R = 1$**(bottom)** response to β_0 perturbation. Forward flight condition. Correlation among BEM simulation and prediction given by state space model. ● BEM, —— present model 94

4.49 Spanwise error distribution. Forward flight condition. Infow approximation by different number of shape functions. —— $N = 4$, - - - $N = 7$, ● $N = 12$ 95

4.50 Spanwise error distribution. Forward flight condition. —— present model , —— linear Pitt-Peters like 95

4.51 Wake inflow response at $r/R = 0.7$ **(top)**, $r/R = 0.85$, $r/R = 0.95$ **(bottom)** to θ_0^+ perturbation. Forward flight condition. Correlation among BEM simulation and prediction given by state space model. ● BEM —— present model upper rotor, —— present model lower rotor 96

4.52 Correlation of spectra response to θ_0^+ perturbation. Forward flight condition. Correlation among BEM simulation and prediction given by state-space model prediction. ● BEM, —— present model upper rotor 97

4.53 Spanwise error distributions. Forward flight condition. —— present model upper rotor —— present model lower rotor - - - w/o multi-harmonic terms; -·-·- Pitt-Peters-like model; • w/o finite-state approximation. 98

4.54 Aeromechanics roots determined by different inflow models. $\hat{\mathbf{H}}_\theta$, $\hat{\mathbf{H}}_V$, $\hat{\mathbf{H}}_\beta$, $\hat{\mathbf{H}}_\Omega$, $\mathbf{H}_q$, + $\mathbf{H}_{PP}$. 99

4.55 Aeromechanics roots determined by different inflow models, detail $\hat{\mathbf{H}}_\theta$, $\hat{\mathbf{H}}_V$, $\hat{\mathbf{H}}_\beta$, $\hat{\mathbf{H}}_\Omega$, $\mathbf{H}_q$, + $\mathbf{H}_{PP}$. 100

4.56 Eigenvectors associated to the poles in Fig. 4.54. 100

4.57 Eigenvectors associated to the poles in Fig. 4.55. 101

4.58 Transfer function w vs θ_0 $\hat{\mathbf{H}}_\theta$, $\hat{\mathbf{H}}_V$, $\hat{\mathbf{H}}_\beta$, $\hat{\mathbf{H}}_\Omega$, $\mathbf{H}_q$, - - -$\mathbf{H}_{PP}$. 102

4.59 Transfer function p vs θ_c. $\hat{\mathbf{H}}_\theta$, $\hat{\mathbf{H}}_V$, $\hat{\mathbf{H}}_\beta$, $\hat{\mathbf{H}}_\Omega$, $\mathbf{H}_q$, - - -$\mathbf{H}_{PP}$. 102

4.60 Transfer function r vs θ_p. $\hat{\mathbf{H}}_\theta$, $\hat{\mathbf{H}}_V$, $\hat{\mathbf{H}}_\beta$, $\hat{\mathbf{H}}_\Omega$, $\mathbf{H}_q$, - - -$\mathbf{H}_{PP}$. 103

4.61 Transfer function p vs θ_s. $\hat{\mathbf{H}}_\theta$, $\hat{\mathbf{H}}_V$, $\hat{\mathbf{H}}_\beta$, $\hat{\mathbf{H}}_\Omega$, $\mathbf{H}_q$, - - -$\mathbf{H}_{PP}$. 103

Chapter 1

Introduction

The relevance of the dynamical behavior of the helicopter wake is known since the early 1950s. During the last sixty years, dynamic wake models have found a firm place in rotary-wing analysis. Despite the existence of more accurate tools at evaluating the induced velocity field over the rotor disc, such as computational fluid dynamic (CFD) or free wake models, dynamic wake models are still preferred in many rotorcraft applications like stability analysis, control law synthesis and real time simulations. The strength of these models are the low computational cost required and the fast implementation that make them easy to understand and use. However, the development of these models has always been dependent on parameters to be tuned in order to overcome some discrepancy between computational results and flight test data [1]. These modifications applied on top of the physical model are justified from an engineering standpoint but while improving simulations for particular operating conditions they may be completely wrong in other flight conditions or for different classes of rotorcraft. The need to tune the model can often be related to the discrepancies of the mathematical model describing the wake dynamics. The physics involved is indeed the result of the coupling of complex phenomena like the strong aerodynamic interference effects among bodies, the interaction of the air flow with the fuselage, the main and tail rotor mutual interactions, the interaction with the ground and severe blade-vortex interactions. Investigation in the 1990's and 2000's in the USA [2, 3, 4, 5, 6, 7, 8] pointed out several deficiencies in current rotor wake modeling for real time applications and suggested that inaccurate

and incomplete modeling of transient dynamics of the rotor wake results in deficiencies in simulator behavior to pilot control inputs. In addition, concerning rotorcraft pilot couplings (RPC), recent research [9, 10, 11] highlighted the effects that wake modeling may have on pilots biodynamic simulated response. Moreover, the existing finite state models do not fit the new generation of rotorcraft (e.g., tiltrotors, coaxial and compounds). For these reasons the ability to include a more realistic behavior of wake dynamics, in state-space format, is fundamental in the development of efficient and reliable simulation tools for the design of new generation of rotorcraft.

1.1 State of the art: dynamic inflow modeling

It is well known that the wake-induced velocities at the rotor disc, also called inflow, play a crucial role in rotor unsteady aerodynamics and must be accounted for determining the blade loading. Usually the term dynamic inflow is used to indicate the unsteady response of inflow caused by changes of load conditions on the rotor. The mathematical formulation of the dynamic inflow is a natural application of the momentum equation. Indeed, in any flight condition, the rotor is supported by the air with an aerodynamic force generated by the interaction between the blades and the air itself. Consequently the rotor exerts a force of the same magnitude in the opposite direction. This force clearly accelerates the air just around the rotor. The governing equations of the accelerated air represent the dynamic inflow model and are a set of first-order differential equations relating inflow variables to aerodynamic loading variables. In particular, in its first formulation, the dynamic inflow is a mathematical model that, given the time history of blade loads on a rotor, produces the induced flow orthogonal to the tip-path-plane. The most famous and surely widely used dynamic inflow model in rotorcraft applications is the Pitt-Peters model, [12]. Based on the disc actuator theory, its basic formulation goes back to the 1980s. During the twentieth century great advances were achieved both for the non-uniform static description of the flow field over the rotor disc and its unsteady dynamics. Treasuring the results coming from the non-uniform description of the inflow from Kinner [13], Mangler-Squire [14] and starting from the first attempt of including the inertia of the air surrounding the rotor [15], Peters approximates the non dimensional wake inflow perturbation, over the rotor disc by uniform plus linear terms

$$v_i = v_0 + r(v_c cos\psi + v_s sin\psi) \tag{1.1}$$

where r denote the non dimensional distance from the disc center, v_0, v_c, v_s represent, respectively, the uniform and linear perturbations coefficients of the wake-induced downwash and ψ is the azimuth angle. Peters treats the inflow coefficients as dynamic states and relates them to the perturbed hub loads. In particular the v_0 coefficient is related to thrust coefficient C_T whereas v_c, v_s, are related to the aerodynamic rolling

and pitching moment, C_L and C_M. Thus the Pitt-Peters dynamic inflow equations are

$$\boldsymbol{M}\begin{Bmatrix} \dot{v_0} \\ \dot{v_s} \\ \dot{v_c} \end{Bmatrix} + V\boldsymbol{L}^{-1}\begin{Bmatrix} v_0 \\ v_s \\ v_c \end{Bmatrix} = \begin{Bmatrix} C_T \\ -C_L \\ -C_M \end{Bmatrix}_{aero} \tag{1.2}$$

In the equations, the effect of wake contraction is given through the mass flow parameter V, which is written in terms of advance ratio, climb rate, and average induced flow [16]. From the potential theory solution developed by Mangler and Squire, Peters evaluated the coefficients of the derivative matrix $\boldsymbol{L}$.

$$\boldsymbol{L} = \begin{bmatrix} \frac{1}{2} & 0 & \frac{15\pi}{64}X \\ 0 & 2(1+X^2) & 0 \\ \frac{15\pi}{64}X & 0 & 2(1-X^2) \end{bmatrix} \tag{1.3}$$

Where the effect of wake skew angle χ appears explicitly in the parameter $X = tan(\chi/2)$ The diagonal mass matrix $\boldsymbol{M}$ was obtained from the virtual mass of an impermeable disc in translation or rotation, as initially suggested by Munk in [17].

$$\boldsymbol{M} = \begin{bmatrix} 8/3\pi & 0 & 0 \\ 0 & -16/45\pi & \\ 0 & 0 & -16/45\pi \end{bmatrix} \tag{1.4}$$

Once this set of equations is solved, at any point of the rotor disc the induced flow is defined by eq. 1.1.

Even if supported by some experimental results, [16], this theory is still based on the actuator disc and it presents an inherent limitation to account for the more complicated phenomena which are, for example, to a more accurate wake modeling. Moreover, hub loads are therein used as aerodynamic load on the rotor to associate with the induced velocity, that is to say the model does not distinguish between different lift distributions that may yield the same hub loads. Another limitation for the Pitt-Peters model is that it is a low-order model approximation of the rotor disc induced flow field based on the equation of a plane in polar coordinates. A generalization of Pitt-Peters inflow model is presented by Peter and He in [18]. Starting from the momentum equation, the derivation of Peters-He model is more mathematically rigorous and it is consistent with

first principles. The model uses the odd functions of the Legendre polynomials and Fourier harmonics to model the pressure perturbations along the radial and azimuthal directions of a rotor disc

$$P = \frac{1}{2} \sum_{m=0}^{\infty} \sum_{n=m+1,m+3,..}^{\infty} \bar{P}_n^m(\nu) \nu \bar{Q}_n^m(i\eta) \left[\tau_n^{mc} cos(m\bar{\psi}) + \tau_n^{ms} sin(m\bar{\psi}) \right] \tag{1.5}$$

The approximation of inflow distribution is generalized similarly to the pressure distribution so that an arbitrary number of harmonics and radial shape functions can be used for each inflow state

$$v_i = \sum_{m=0}^{\infty} \sum_{n=m+1,m+3,..}^{\infty} \frac{\bar{P}_n^m(\nu)}{\nu} \left[\alpha_n^m cos(m\bar{\psi}) + \beta_n^m sin(m\bar{\psi}) \right] \tag{1.6}$$

where $\bar{P}_n^m$ and $\bar{Q}_n^m$ are associated normalized Legendre functions of the first kind expressed in ellipsoidal coordinates (ν, η, ψ), τ_n^{mc}, τ_n^{ms} represent cosine and sine pressure coefficients and α_n^m, β_n^m are the inflow states. Then Peters-He use orthogonality relations to form closed form matrices based on free stream skew angle and flight speed which relate pressure perturbations at the disc to inflow velocities at the disc

$$\boldsymbol{M} \left\{ \dot{\alpha_n^m} \right\} + V \boldsymbol{L}_c^{-1} \left\{ \alpha_n^m \right\} = \frac{1}{2} \left\{ \tau_n^{mc} \right\} \tag{1.7}$$

$$\boldsymbol{M} \left\{ \dot{\beta_n^m} \right\} + V \boldsymbol{L}_s^{-1} \left\{ \beta_n^m \right\} = \frac{1}{2} \left\{ \tau_n^{ms} \right\} \tag{1.8}$$

The matrix $\mathbf{M}$ is the apparent mass matrix and $\mathbf{L}_c$, $\mathbf{L}_s$ are respectively the cosine and sine influence coefficient matrices. These are all given in closed form in [19]. Note that the $\mathbf{M}$ matrix of eqs. 1.7 and 1.8 of course differs from that one of eq. 1.4 but historically they are indicated with the same letter.

Even if superior to the previously presented model, the Peters-He model cannot provide an accurate description of inflow in the close vicinity of the blade surface, nor can it account for wake roll-up. Moreover, some relevant differences were found when the model was applied to predict the dynamic response of the helicopter both in hover and in low speed forward flight in comparison with the corresponding flight test data, [20] [21]. A large number of publications explained the problem with the deficiency of the inflow model to take into account phenomena such as gyroscopic force of the

wake, aerodynamic interaction between rotor and fuselage [21], wake distortion [22]. In order to overcome some of these problems, such as wake distortion, in the last twenty years modified versions of Peters-He were proposed. Reference [23] proposes that the gain matrix $\boldsymbol{L}$ should be modified as an augmented L-matrix so as to account for the effects due to wake curvatures. In particular in [24] Zhao uses a vortex tube method to determine the influence of distortions in the geometry of the wake at the rotor disc. The effects of three different disturbances -changes in wake bending, wake skew and wake spacing- expressed by the combination of hub and blade motion, are examined. However, the complicated wake distortion effects are incorporated by wake curvature parameters, which are empirically determined and are strongly depended on the method used to derive the wake distortion dynamic model. Despite this artificial modification improved some comparison with experimental data, the inclusion of the wake effects into dynamic inflow modeling is still an issue and further improvement, validation and correlation with experimental, CFD and free wake simulation are required, partly because the correction parameters must be essentially empirically determined.

Nowadays the focus on developing dynamic inflow models for advanced rotor configuration. Indeed, the presented models have been developed for and extensively used in modeling single main rotor helicopters. The future of the helicopter manufacturers will include configurations beyond the traditional single main rotor/trail rotor helicopters (e.g., tiltrotors, coaxial and compounds helicopter) and advances in simulation modeling are required. Recently state-space models of coaxial rotor wakes have been developed by extending the Peters-He finite state dynamic inflow model to account for the mutual aerodynamic interference of coaxial rotors by application of enhanced momentum theory [25], [26]. In particular in the model proposed by Prasad the influence coefficient matrix $\mathbf{L}$ is augmented in order to include the mutual influence between upper and lower rotors.

Although some advancement has been made in modeling aerodynamic interference, all these models are still based on simplified aerodynamic solutions unable to capture many important phenomena deriving from the complex aerodynamic field. Even if they cannot provide a comprehensive description of the inflow flow field they are extensively utilized in helicopter modeling.

1.2 Role of the dynamic inflow in helicopter modeling

The dynamic inflow plays a crucial role in helicopter modeling. Indeed, an helicopter simulation model is characterized by two main aspects

- Blade structural modeling
- Rotor aerodynamic modeling

In ref. [27], Padfield categories the helicopter models for simulation into three levels of increasing complexity specifying the application they are suitable for (see Tab. 1.1)

Table 1.1: Levels of rotor mathematical modeling

	Dynamics	Aerodyamics	Applications
Level 1	rigid blades (1) quasi-steady motion (2) 3 DoF flap (3) 6 DoF flap + lag (4) 6 DoF flap + lag +quasi-steady torsion	-linear 2-D **-dynamic inflow**/local momentum theory -analytically integrated loads	parametric trends for flying qualities and performance studies well within operational flight envelope low bandwidth control
Level 2	(1) rigid blades with options as in Level 1 (2) limited number of blade elastic modes	-nonlinear (limited 3-D) **-dynamic inflow**/local momentum theory -local effects of blade vortex interaction -unsteady 2-D compressibility numerically integrated loads	parametric trends for flying qualities and performance studies up to operational flight envelope medium bandwidth appropriate to high gain active flight control
Level 3	detailed structural representation as elastic modes or finite elements	-nonlinear 3-D full wake analysis (free or prescribed) -unsteady 2-D compressibility numerically integrated loads	rotor design rotor limit loads prediction vibration analysis rotor stability analysis up to safe flight envelope

In many applications the rotor aerodynamic loads are evaluated as a radial integration of the loads given by sectional aerodynamic models. These are typically derived from airfoil unsteady aerodynamic models coupled with a dynamic inflow theory, [28]. For instance, in different helicopter prediction tools that are widely used by aeronautics industries, the flight-mechanics and aeroelastic analyses are performed by using two-dimensional, quasi-steady aerodynamic models with wake-inflow corrections. For a thin, straight airfoil moving in an incompressible flow, following the Greenberg theory [29] it is possible to determine the aerodynamic force acting on it as a combination of the orthogonal component to the chord, the noncirculatory lift, L_{nc}, and the component directed along the normal to the relative wind, the circulatory lift, L_c. The noncirculatory lift is expressed as

$$L_{nc}(t) = \pi \varrho b^2 \dot{v}^n_{1/2} \tag{1.9}$$

where ϱ is air density, b denotes airfoil semichord length and $\dot{v}^n_{1/2}$ denotes the time derivative of the normal component of the relative wind evaluated at the airfoil mid point (positive upwards).
The circulatory lift is expressed as

$$L_c(t) = 2\pi \varrho b V \mathcal{F}^{-1}[C(k)\tilde{v}^n_{3/4}] \tag{1.10}$$

where V denotes the relative wind velocity, $\mathcal{F}$ denotes the Fourier transform, and $v^n_{3/4}$ represents the normal component of the relative wind evaluated at the airfoil $3/4$-chord point. Moreover, $C(k)$ is the Theodorsen lift deficiency, defined in terms of the reduced frequency, $k = \omega b/V$ where ω is the Fourier domain variable, [29]. The fundamental difficulties for the application of the unsteady aerodynamics airfoil theories is the presence of the transcendental function of the reduced frequency that requires the introduction of a convolution integral for the evaluation of the circulatory lift (see [30]). However, under the assumption of very low frequency analysis, the lift deficiency function is constant and equal to one. This restriction implies that the effects of unsteady shed vortices on the 2-D theoretical solutions are neglected and this assumption introduces some simplification in the numerical analysis. The inaccuracies introduced by this approximation could be compensated by coupling airfoil theories with dynamic inflow models or di-

rectly with a high fidelity aerodynamic solver. Indeed they provide the induced velocity field that has to be accounted into the downwash term, $v^n_{3/4}$ appearing in eq. 1.10.

1.3 Objectives and outline of the dissertation

The advantage in terms of simplicity of dynamic wake inflow models is undeniable. Based on first principles, they represent a white-box describing the unsteady dynamics of the induced velocity; they may be associated with practical modifications or empirical corrections in order to incorporate additional effects (such as wake distortion) and thanks to their state-space formulation, they can easily be coupled with a lift theory - rotor, fuselage and pilot dynamics - in order to perform aeroelasticity, flight mechanics, and handling quality assessment, as well as for flight control law synthesis.

However this simplicity leads to a poor description of the physical model, and to the

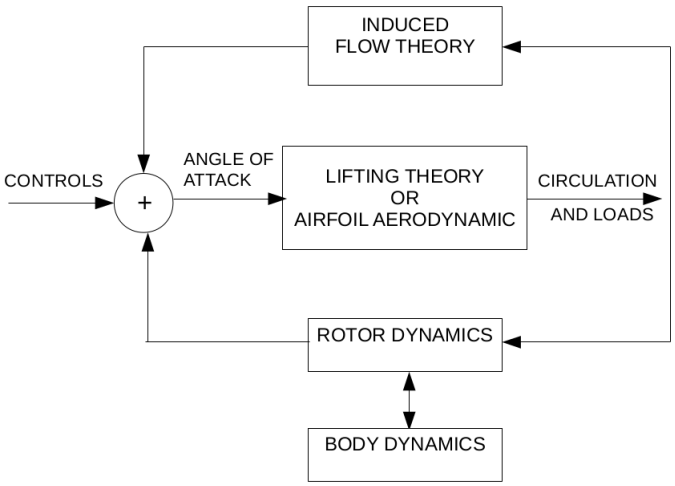

Figure 1.1: General work-flow sketch for the typical use of the dynamic inflow model.

introduction of artificial parameters to be determined that are strongly dependent on the method they are derived from. Moreover this models have the drawback that are not reliable in the presence of complex aerodynamic phenomena like strong aerodynamic interference and severe blade-vortex interactions and are not suitable for the new generation of rotorcraft. It is well known that in order to have a more accurate and generic representation of the induced velocity field high-fidelity physics-based inflow

models (e.g. free-vortex wake models, CFD, VPM, etc.) must be used. The fundamental problem of the high-fidelity models is the high computational cost they required. Moreover they cannot be applied in real-time simulation, stability analysis and control law applications where a finite state format is required.
The overall objective of this dissertation is the extraction of finite-state dynamic models of rotor wake inflow from simulations provided by high-fidelity aerodynamic solvers (which, however, might be of arbitrary accuracy and complexity), and, more in general, on the development of a complete tool chain allowing to derive computationally efficient, reduced-order wake inflow models from complex aerodynamic solvers, to be used for aeromechanics and aeroelastic simulations.
This work is structured as follows:

- In chapter 2 the finite-state dynamic inflow models developed in this work will be introduced.
- In chapter 3 the developed methodologies to extract linear time invariant and linear time periodic models from any high fidelity solver will be described.
- In chapter 4 the numerical results of the dynamic wake inflow identification and the impact of the inflow models on flight mechanics simulation will be illustrated.
- Finally in chapter 5 a series of concluding remarks will be presented.

Chapter 2

Dynamic Wake Inflow in State Space Format

In this chapter two possible models obtained by applying system identification techniques to high fidelity aerodynamic solvers are presented. Being the models linearized it is important to underline that they are valid about a given flight condition. However, even if this could be considered a limitation, an entire helicopter flight envelope could be obtained by applying a model stitching technique, as in ref. [31]. A general description of the models, initially based on a single main rotor configuration and later extended to the coaxial rotors configuration, is here presented. The extraction techniques will be presented in next chapter.

2.1 Inflow representation

In order to represent the complex wake inflow field with a level of accuracy suitable flight mechanics and aeroelastic applications, it is expressed in a non-rotating frame in terms of spanwise-varying multiblade variables. Indeed, introducing over the rotor disc the hub-fixed polar coordinate system, (r, ψ), for a four-bladed rotor, the computed wake inflow perturbation, is approximated through the following extension of the eq. 1.6:

$$v_i(r,\psi_i,t) = v_0(r,t) + v_c(r,t)\cos\psi_i + v_s(r,t)\sin(\psi_i) + \\ + v_{N/2}(r,t)\,(-1)^i \tag{2.1}$$

where ψ_i denotes the azimuth position of the i-th blade, whereas v_0, v_c, v_s and $v_{N/2}$ are, respectively, the instantaneous multiblade collective, cyclic and differential inflow coefficients at a given radial position, r. For v_B denoting the non dimensional wake inflow perturbation evaluated by the high-fidelity aerodynamic tool on the i-th rotor blade, applying the separation of variables technique, and choosing suitable sets of linearly independent radial basis functions, $\phi_{\alpha,j}(r)$, the multiblade wake inflow coefficients are expressed in the following form

$$\begin{aligned}
v_0(r,t) &= \frac{1}{N_b}\sum_{i=1}^{N_b} v_B(r,\psi_i,t) = \sum_{j=1}^{N_{0,r}} \lambda_{0,j}(t)\ \phi_{0,j}(r) \\
v_c(r,t) &= \frac{2}{N_b}\sum_{i=1}^{N_b} v_B(r,\psi_i,t)\cos\psi_i = \sum_{j=1}^{N_{c,r}} \lambda_{c,j}(t)\ \phi_{c,j}(r) \\
v_s(r,t) &= \frac{2}{N_b}\sum_{i=1}^{N_b} v_B(r,\psi_i,t)\sin\psi_i = \sum_{j=1}^{N_{s,r}} \lambda_{s,j}(t)\ \phi_{s,j}(r) \\
v_{N/2}(r,t) &= \frac{1}{N_b}\sum_{i=1}^{N_b} v_B(r,\psi_i,t)\,(-1)^i = \sum_{j=1}^{N_{N/2,r}} \lambda_{N/2,j}(t)\ \phi_{N/2,j}(r)
\end{aligned} \tag{2.2}$$

where N_b denotes the number of rotor blades, $N_{\alpha,r}$ is the number of functions used to define the α coefficient radial distribution with $\alpha = 0, c, s, N/2$, with $\lambda_{\alpha,j}$ representing the corresponding component onto the basis function $\phi_{\alpha,j}$. The differential component appears only for rotors with an even number of blades, whereas higher-harmonic multiblade cyclic components are included for $N_b > 4$.

It is worth noting that, neglecting the differential and (if present) the higher-harmonic cyclic components, for $N_{0,r} = N_{c,r} = N_{s,r} = 1$, $\phi_{0,1} = 1$, and $\phi_{c,1} = \phi_{s,1} = r$, the proposed inflow distribution coincides with the Pitt-Peters equation 1.1. In the present work this model is referred to as the Pitt-Peters-like inflow approximation, whereas expression 2.1 is called generalized model. In order to evaluate the the $\lambda_{\alpha,j}(t)$ coefficients

the following system is solved

$$\begin{bmatrix} \lambda_{\alpha,1} \\ \lambda_{\alpha,2} \\ \vdots \\ \lambda_{\alpha,N_{\alpha,r}} \end{bmatrix} = \Phi^{+} v_{\alpha} \tag{2.3}$$

where Φ^{+} is the Moore-Penrose inverse matrix of the shape functions and v_{α} is the α multiblade-coefficient of the inflow representation.

One of the most relevant difference between the state of art and the proposed inflow approximation is the introduction of the differential inflow coefficient $v_{N/2}$ in the approximating formula of the inflow flow field. The introduction of this term in the approximating formula is mandatory in order to reproduce the total spectrum of the computed inflow. In this context, it is important to observe that, except for axi-symmetric hovering operating condition, the time-periodic nature of rotor aerodynamics yields multi-harmonic responses to single-harmonic inputs. For instance, for small-perturbation harmonic input of frequency ω, non-zero harmonic components of the corresponding inflow v_B appear at the frequencies $\omega + m\Omega$, therefore non-zero harmonic components of the corresponding inflow coefficients appear at the frequencies $\omega + mN_b\Omega + H$ for $m \in [-N_m, N_m]$; with N_m related to the maximum order of periodicity of the aerodynamic operator and H is a coefficient depending on the input/output type (see table **??**).

	Input Type	
Output Type	Collective-Cyclic	Differential
Collective-Cyclic	0	$\Omega N_b/2$
Differential	$\Omega N_b/2$	0

Table 2.1: Values of H for different input/output type.

Considering a four-bladed rotor in forward flight at advance ratio $\mu = 0.2$, this is confirmed by the results shown in figs. 2.1 and 2.2 that present respectively the spectra of the computed inflow and the inflow coefficients evaluated at a radial position $r/R = 0.7$ for an azimuth angle $\psi = \pi/2$, response to a low-frequency harmonic longitudinal cyclic pitch with $\omega = 10$ rad/s. The computed inflow v_B is evaluated by an aerodynamic tool based on Boundary Element Method presented in chapter 4 and in appendix B.

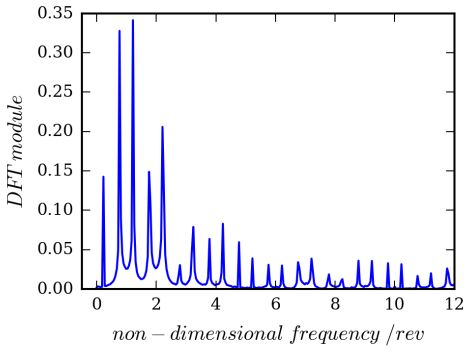

Figure 2.1: Spectrum of the computed inflow v_B at radial station $0.7R$ and $\psi = \pi/2$ response to harmonic θ_c perturbation. Forward flight condition.

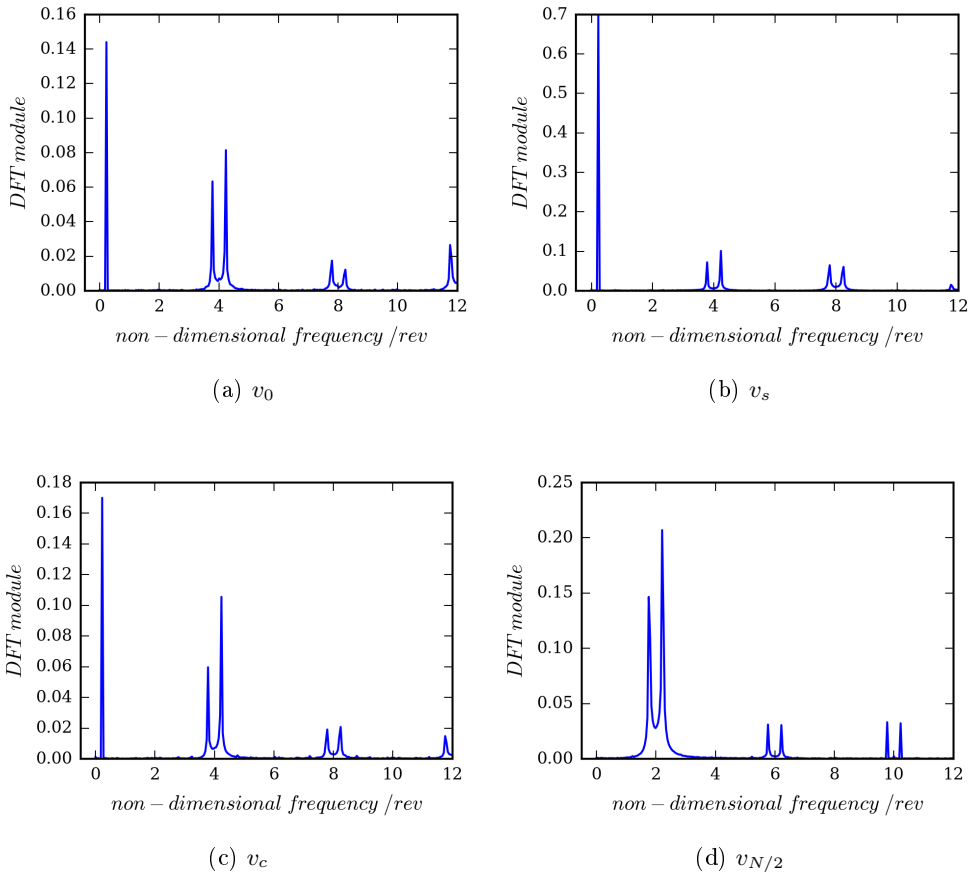

(a) v_0 (b) v_s

(c) v_c (d) $v_{N/2}$

Figure 2.2: Spectrum of inflow coefficients at radial station $0.7R$ and $\psi = \pi/2$ response to harmonic θ_c perturbation. Forward flight condition.

Figures 2.2(a,b,c) show that the spectra of collective and cyclic inflow coefficients are characterized by a single tonal peak at the very-low input frequency, and by tonal peaks, around the 4/rev harmonic and one around the 8/rev one. Figure 2.2(d) shows that the spectra of the differential inflow coefficient is characterized by tonal peaks around the 2/rev, 6/rev harmonic and one around the 10/rev one. The importance of the introduction of the differential inflow coefficient is showed in fig. 2.3 where the spectra correlation between the computed inflow v_B and the its approximation v_i is showed. The continuous blue line represent the spectrum of the approximated inflow neglecting the differential coefficient while in the red line the latter coefficient is included.

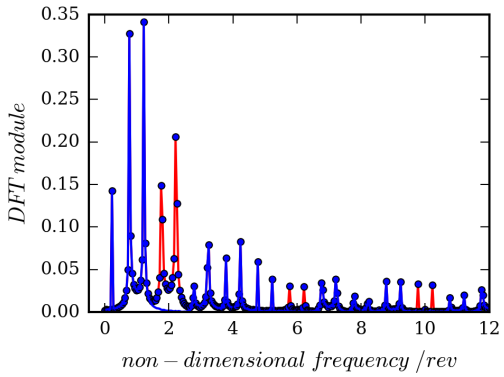

Figure 2.3: Correlation of spectra between the computed inflow ● v_B and its approximation v_i w/o —/— differential coefficient, at radial station $0.7R$ and $\psi = \pi/2$ response to harmonic θ_c perturbation

2.2 Dynamic inflow models

The dynamic inflow models developed are here introduced by their non-parametric sampled transfer functions. The state-space parametrization is also here presented, while the identification process of the models is discussed in Chapter 3.

2.2.1 Linear time invariant dynamic inflow model

Even if for some classes of helicopters (for instance coaxial rotor) and in particular flight conditions such as forward flight, the inflow operator is strongly time periodic, for

flight-mechanics applications and in general low frequency applications, is reasonable to neglect the time periodic effects. Indeed the low frequency dynamics related to flight mechanics are distant from the multi-harmonic behavior of the inflow. Neglecting the time periodic nature of the aerodynamic operator, yields to a linear time invariant LTI model that generates a transfer function providing an input/output one-to-one map, [32]. This means that if the input of the system is a sinusoid (or a complex exponential) the predicted output will have the same frequency of the input at steady state while gain and phase are predicted by the transfer function.
Two different LTI version of dynamic inflow are here presented.

Kinematic based model

The linear time invariant version of the kinematic model $\lambda - q$ relates the wake inflow coefficients to typical degrees of freedom of the flight mechanics problems namely blade pitch controls, $\mathbf{q}_\theta = \{\theta_0 \ \theta_s \ \theta_c\}^T$, hub linear velocity components, $\mathbf{q}_V = \{u \ v \ w\}^T$, hub angular velocity components, $\mathbf{q}_\Omega = \{p \ q \ r\}^T$ and rigid blade flapping variables, $\mathbf{q}_\beta = \{\beta_0 \ \beta_s \ \beta_c\}^T$. Being all the variables of collective and cyclic type, the differential inflow coefficients is null, thus the model takes into consideration the inflow coefficients $\boldsymbol{\lambda} = \{\boldsymbol{\lambda}_0 \ \boldsymbol{\lambda}_s \ \boldsymbol{\lambda}_c\}^T$. Differently from the classical dynamic inflow theories that relate the perturbed induced velocity to the perturbed loads, this model relates the inflow directly with the causes that can produce different lift distribution and may preserve the same hub loads. Moreover, being the wake evolution strongly influenced by the complex motion of the trailing edge of the blades, seems reasonable to relate the influence of the wake vortices with all the variables that define the position of the vortices separation from the trailing edge. The $\lambda - q$ model generates a non parametric transfer function between inflow coefficients and blade/hub kinematics inputs such that in the Fourier domain

$$\tilde{\boldsymbol{\lambda}} = \boldsymbol{H}_\theta \tilde{\boldsymbol{q}}_\theta + \boldsymbol{H}_V \tilde{\boldsymbol{q}}_V + \boldsymbol{H}_\Omega \tilde{\boldsymbol{q}}_\Omega + \boldsymbol{H}_\beta \tilde{\boldsymbol{q}}_\beta = \boldsymbol{H}(\omega)\tilde{\boldsymbol{q}} \tag{2.4}$$

where $\tilde{\boldsymbol{q}} = \{\tilde{\boldsymbol{q}}_\theta \ \tilde{\boldsymbol{q}}_V \ \tilde{\boldsymbol{q}}_\Omega \ \tilde{\boldsymbol{q}}_\beta\}$ and $\boldsymbol{H}(\omega) = [\boldsymbol{H}_\theta \ \boldsymbol{H}_V \ \boldsymbol{H}_\Omega \ \boldsymbol{H}_\beta]$ is the $[M \times N]$ transfer function matrix with $M = (N_{0,r} + N_{c,r} + N_{s,r})$ and $N = 12$ respectively the number of outputs and inputs.

Load based model

In order to follow the well known dynamic inflow theories and to investigate the influence of the different blade/hub kinematics variables considered, a model relating wake inflow coefficients to hub loads is also presented. This model is considered only with the Pitt-Peters like inflow approximation of eq. 1.1.

The high fidelity aerodynamic solvers in output offer both hub loads and wake inflow over the blades. The load based model $\lambda - f$ relates the inflow coefficients to rotor thrust, roll and pitching moment coefficients $\mathbf{f} = \{C_T, C_L, C_M\}^T$ exactly like the Pitt and Peters' model. In order to obtain the Pitt-Peters like model, the additional identification of the transfer function matrix between the perturbations of the kinematic input variables and the corresponding rotor thrust and roll and pitch moments is required.

Note that, these rotor loads are linearly related to blade bound circulation, and hence to the corresponding wake vorticity and inflow; the remaining three rotor loads (namely, lateral forces and torque) are closely related to induced drag and hence quadratically related to inflow.

To this purpose, the transfer function matrices, $\boldsymbol{G}_\theta, \boldsymbol{G}_V, \boldsymbol{G}_\Omega$ and $\boldsymbol{G}_\beta$, relating, respectively, the kinematic perturbations, $\tilde{\boldsymbol{q}}_\theta$, $\tilde{\boldsymbol{q}}_V$, $\tilde{\boldsymbol{q}}_\Omega$ and $\tilde{\boldsymbol{q}}_\beta$ to the rotor loads are evaluated through the same a procedure to that applied for eq. 2.4, simply replacing the aerodynamic output $\tilde{\boldsymbol{\lambda}}$ with $\tilde{\boldsymbol{f}}$ (as available from the same time responses used for $\boldsymbol{H}_\theta$ $\boldsymbol{H}_V$ $\boldsymbol{H}_\Omega$ and $\boldsymbol{H}_\beta$ identification).

Then, considering for instance the matrix $\boldsymbol{G}_V$, its inverse matrix is determined and the wake inflow coefficients are directly related to the rotor loads as follows:

$$\tilde{\boldsymbol{\lambda}} = \hat{\boldsymbol{H}}_V(\omega)\tilde{\boldsymbol{f}} \tag{2.5}$$

where $\hat{\boldsymbol{H}}_V(\omega) = \boldsymbol{H}_V(\omega)\boldsymbol{G}_V^{-1}(\omega)$ is the $[3\times3]$ transfer function matrix (equivalent transfer function matrices, $\hat{\boldsymbol{H}}_\Omega$, $\hat{\boldsymbol{H}}_\theta$ and $\hat{\boldsymbol{H}}_\beta$, may be derived from $\boldsymbol{G}_\Omega$,$\boldsymbol{G}_\theta$ and $\boldsymbol{G}_\beta$).

2.2.2 Linear time periodic dynamic inflow model

For aeroelastic applications and in general for high-frequency analyses the LTI approximation loses its effectiveness. A time periodic system is characterized by a time varing-periodic transfer function with period T. The important notion behind linear time

periodic LTP system is its fundamental frequency defined as $\omega_p = 2\pi/T$. In contrast to the LTI case, if a complex exponential (or sinusoidal) is input to an LTP system, the output consists in a superposition of sinusoids not only at the input frequency ω, but also at several (or an infinite) other frequency , $\omega + n\omega_p$, each with possibly different gain and phase, where n is an integer. This one-to-many behavior of the harmonics is described by the harmonic transfer function matrix defined by Zadeh in [33].
In this work a linear time periodic extension of the kinematic based inflow model is proposed.

Kinematic based model

Being the model appropriate for high-frequency applications (e.g for aeroelastic problems), the linear time periodic version of the $\lambda - q$ model relates wake inflow coefficients, $\boldsymbol{\lambda} = \{\boldsymbol{\lambda}_0\ \boldsymbol{\lambda}_s\ \boldsymbol{\lambda}_c\ \boldsymbol{\lambda}_{N/2}\}^T$, to harmonic perturbations of hub linear and angular velocity variables respectively $\mathbf{q}_V$ and $\mathbf{q}_\Omega$, blade pitch control variables $\mathbf{q}_\theta$ and the blade elastic degrees of freedom - blade flap β and lag γ bending as well as elastic torsion φ - expressed in the fixed-frame of reference. For instance for a generic rotor having N_b flexible blades, let us denote with $\boldsymbol{\zeta}^m(t)$ the vector collecting the elastic degrees of freedom of the $m-th$ blade in the rotating frame (generally described as a linear combination of N_ζ shape functions). Then, the corresponding multiblade coordinates of the $i-th$ mode are defined as (see, [34, 35]):

$$\begin{aligned}
\zeta_{i,0}(t) &= \frac{1}{N_b}\sum_{m=1}^{N_b}\zeta_i^m(t) \\
\zeta_{i,nc}(t) &= \frac{2}{N_b}\sum_{m=1}^{N_b}\zeta_i^m(t)\cos n\psi_m \\
\zeta_{i,ns}(t) &= \frac{2}{N_b}\sum_{m=1}^{N_b}\zeta_i^m(t)\sin n\psi_m \\
\zeta_{i,N/2}(t) &= \frac{1}{N_b}\sum_{m=1}^{N_b}\zeta_i^m(t)\,(-1)^m
\end{aligned} \tag{2.6}$$

where the number of cyclic modes, $\zeta_{i,nc}$, $\zeta_{i,ns}$, depends on the harmonic index, n, ranging between $n = 1$ and $(N_b - 1)/2$ for N_b odd, and between $n = 1$ and $(N_b - 2)/2$ for N_b even. The coordinate $\zeta_{i,N/2}$ (differential mode) is present only if N_b is even.

From the multi-harmonic behavior of the wake inflow coefficients previously presented, the pumping frequencies of the inflow coefficients result $\omega_p = N_b\Omega - H$ and depend on the input/output type by the H coefficient. Indeed, in order to identify the Zadeh's transfer function, each jth component of the $\boldsymbol{\lambda}_\alpha$ inflow coefficient is decomposed in a summation of an arbitrary finite number of harmonics n_h as

$$\lambda_{\alpha,j}(t) = \lambda^0_\alpha(t) + \sum_{k=1}^{n_h} \lambda^{kc}_{\alpha,j}(t)cos(k\omega_{p,\alpha}t) + \lambda^{ks}_{\alpha,j}(t)sin(k\omega_{p,\alpha}t) \tag{2.7}$$

where $\omega_{p,\alpha}$ indicate the pumping frequency associated to the $\boldsymbol{\lambda}_\alpha$ inflow coefficient. Thus the harmonic transfer function matrix $\boldsymbol{MH}$ relates the input variable $\tilde{\boldsymbol{q}} = \{\tilde{\boldsymbol{\zeta}}\ \tilde{\boldsymbol{q}}_\theta\ \tilde{\boldsymbol{q}}_V\ \tilde{\boldsymbol{q}}_\Omega\}$ with the arbitrary number n_h of harmonic components of the inflow coefficients and it is formed by $m = 2n_h + 1$ blocks with dimension $[M \times N]$, where $M = (N_{0,r} + N_{c,r} + N_{s,r} + N_{N/2,r})$ and $N = (9 + N_\zeta)$ respectively the number of outputs and inputs

$$\boldsymbol{MH}(\omega) = \begin{bmatrix} MH(\omega)_0 \\ MH(\omega)_{1c} \\ MH(\omega)_{1s} \\ \vdots \\ MH(\omega)_{n_hc} \\ MH(\omega)_{n_hs} \end{bmatrix} \tag{2.8}$$

By grouping the harmonic components of the inflow coefficients in vectors $\boldsymbol{\lambda}^0, \boldsymbol{\lambda}^{kc}$ and $\boldsymbol{\lambda}^{kc}$, the blocks of the $\boldsymbol{MH}$ matrix are linear time invariant transfer function matrices, each one relating the input $\tilde{\boldsymbol{q}}$ with a specific component of $\tilde{\boldsymbol{\lambda}}$:

$$\tilde{\boldsymbol{\lambda}}^0 = \boldsymbol{MH}_0(\omega)\tilde{\boldsymbol{q}} \qquad \tilde{\boldsymbol{\lambda}}^{kc} = \boldsymbol{MH}_{kc}(\omega)\tilde{\boldsymbol{q}} \qquad \tilde{\boldsymbol{\lambda}}^{ks} = \boldsymbol{MH}_{ks}(\omega)\tilde{\boldsymbol{q}} \qquad k = 1...n_h \tag{2.9}$$

It is worth noting that this system has more outputs than the LTI model, in particular it has $m \cdot M$ outputs instead of M; the number of inputs is the same. Moreover in the multi-harmonic transfer function matrix defined by the block it is also present the LTI behavior of the system, usually called the best linear time invariant BLTI, and it is indeed equal to

$$\boldsymbol{MH}_0(\omega) = \boldsymbol{H}(\omega) \tag{2.10}$$

useful when a time invariant approximation of a time periodic system has to be performed.

From sampled transfer function to state-space representation

In order to be employed in any rotorcraft analysis, the presented models must have a state-space representation. In this work to achieve that the rational matrix approximation (RMA) method is used. This method, developed and widely used by some researcher of the Department of Engineering of Roma Tre University within the European project *ARISTOTEL*(2010-2013), allows to evaluate the state-space representation from any sampled transfer function.

Considering a generic non parametric transfer function $\boldsymbol{H}$ between an input, $\tilde{\boldsymbol{u}}$, and an output, $\tilde{\boldsymbol{y}}$. The state-space representation is obtained by the determination of rational forms (with a finite number of poles) providing the best fit to the sampled transfer function. Specifically, the rational-matrix approximation of the matrix:

$$\boldsymbol{H}(s) \approx s\,\boldsymbol{A}_1 + \boldsymbol{A}_0 + \boldsymbol{C}\left[s\,\boldsymbol{I} - \boldsymbol{A}\right]^{-1}\,\boldsymbol{B} \tag{2.11}$$

is determined through application of a least-square procedure assuring the stability of the identified poles [36] [37], with $\boldsymbol{A}_1, \boldsymbol{A}_0, \boldsymbol{A}, \boldsymbol{B}$ and $\boldsymbol{C}$ representing real matrices, and s denoting the Laplace-domain variable (see Appendix 1 for an outline of the applied RMA methodology). Finally transforming 2.11 into time domain yields the following state-space representation:

$$\begin{cases} \boldsymbol{y}(t) = \boldsymbol{A}_1\dot{\boldsymbol{x}}(t) + \boldsymbol{A}_0\,\boldsymbol{x}(t) + \boldsymbol{C}\,\boldsymbol{r}(t) \\ \dot{\boldsymbol{r}}(t) = \boldsymbol{A}\boldsymbol{r}(t) + \boldsymbol{B}\boldsymbol{x}(t) \end{cases} \tag{2.12}$$

where

$$\tilde{\boldsymbol{r}} = \left[s\,\boldsymbol{I} - \boldsymbol{A}\right]^{-1}\,\boldsymbol{B} \tag{2.13}$$

represent the vector of the additional states representing the dynamics of the system under identification.

Applying the methodology to the linear time invariant kinematic based inflow transfer function of eq. 2.4 yields:

$$\tilde{\boldsymbol{\lambda}} \approx \left(s\,\boldsymbol{A}_1 + \boldsymbol{A}_0 + \boldsymbol{C}\left[s\,\boldsymbol{I} - \boldsymbol{A}\right]^{-1}\,\boldsymbol{B}\right)\tilde{\boldsymbol{q}} \tag{2.14}$$

Matrices $\boldsymbol{A}_1$, $\boldsymbol{A}_0$, $\boldsymbol{B}$ and $\boldsymbol{C}$ are real, fully populated matrices, whereas $\boldsymbol{A}$ is a square block-diagonal matrix containing the poles of the approximated transfer functions. Transforming eq. 2.14 into time domain yields the following dynamic wake inflow model in finite-dimensional state-space form:

$$\begin{cases} \boldsymbol{\lambda}(t) = \boldsymbol{A}_1 \dot{\boldsymbol{q}}(t) + \boldsymbol{A}_0\, \boldsymbol{q}(t) + \boldsymbol{C}\, \boldsymbol{r}(t) \\ \dot{\boldsymbol{r}}(t) = \boldsymbol{A}\boldsymbol{r}(t) + \boldsymbol{B}\boldsymbol{q}(t) \end{cases} \tag{2.15}$$

where in this case $\boldsymbol{r}$ is the vector of the additional states representing wake inflow dynamics. The same methodology can be performed with the linear time periodic kinematic based inflow transfer function of eq. 2.8 but the resulting dimensions of the RMA matrices are different. For instance in case of LTI model of eq. 2.4 the resulting state-space matrices have the following dimension: $[\boldsymbol{A}_1] = [\boldsymbol{A}_0] = [M \times N]$, $[\boldsymbol{A}] = [N_a \times N_a]$, $[\boldsymbol{B}] = [N_a \times N]$ and $[\boldsymbol{C}] = [M \times N_a]$, with N_a indicate number of the poles utilized and M and N are respectively the number of outputs and inputs of the linear time invariant model. In case of the LTP model of eq. 2.8, the matrices dimension are: $[\boldsymbol{A}_1] = [\boldsymbol{A}_0] = [(2n_h + 1)M \times N]$, $[\boldsymbol{A}] = [N_a \times N_a]$, $[\boldsymbol{B}] = [N_a \times N$ and $[\boldsymbol{C}] = [M \times N_a]$ where M and N are respectively the number of outputs and inputs of the linear time periodic model.

This inflow model is capable of taking into account all aerodynamic phenomena simulated by the high fidelity aerodynamic solver applied for the transfer function sampling. Coupling eq. 2.1 with the outcomes of the differential model in eq. 2.15 provides the time evolution of the wake inflow linear distribution on the rotor disc, as associated with arbitrary hub motion and pitch control perturbations.

For what concerns the parametrization of the linear time invariant load based models $\lambda - f$, a similar approach is applied, but examination of the asymptotic behavior of the transfer functions between wake inflow and loads provided by any unsteady aerodynamic operator reveals that it tends to zero as perturbation frequency tends to infinity, and hence the polynomial part of the RMA should be neglected. This can be inferred, for instance, from the aerodynamic formulation utilized in this work in Appendix B, observing that wake inflow is directly related to the velocity perturbation (via the boundary conditions), whereas pressure (and hence loads) is related to the first time derivative of

the potential and hence of the velocity perturbations. Therefore, the application of the RMA algorithm to the eq. 2.5 yields:

$$\tilde{\boldsymbol{\lambda}} \approx \left(\boldsymbol{A}_0 + \boldsymbol{C}\left[s\,\boldsymbol{I} - \boldsymbol{A}\right]^{-1}\,\boldsymbol{B} \right)_V \tilde{\boldsymbol{f}} \tag{2.16}$$

that into time domain is:

$$\begin{cases} \boldsymbol{\lambda}(t) = \boldsymbol{A}_0\,\boldsymbol{f}(t) + \boldsymbol{C}\,\boldsymbol{r}(t) \\ \dot{\boldsymbol{r}}(t) = \boldsymbol{A}\boldsymbol{r}(t) + \boldsymbol{B}\boldsymbol{q}(t) \end{cases} \tag{2.17}$$

with $[\boldsymbol{A}_0] = [3 \times 3]$, $[\boldsymbol{A}] = [N_a \times N_a]$, $[\boldsymbol{B}] = [N_a \times 3]$ and $[\boldsymbol{C}] = [3 \times N_a]$. However, matrix $\boldsymbol{A}_0$ may be left in the approximation formula in that, particularly in the low-frequency, finite domains of flight dynamics interest, it provides a wider function space of search of the optimal fitting of the sampled transfer matrix. For $\boldsymbol{A} = \boldsymbol{0}$ and $\boldsymbol{C} = \boldsymbol{I}$, the model in eq. 2.17 is formally identical to the Pitt-Peters dynamic wake inflow model presented in 1.2: in that case, the number of dynamic states is forced to be $N_a = 3$ and, observing that $\boldsymbol{\lambda} = \boldsymbol{x}$, the inflow dynamics coincides with that of the additional states. This differs from the proposed approach which, extending that model, determines N_a as resulting from the RMA of the transfer matrix identified from the unsteady aerodynamics simulations (see Eq. 2.16) and, for $\boldsymbol{A} = \boldsymbol{0}$, provides the inflow parameters as a linear combination of the additional states, $\boldsymbol{\lambda} = \boldsymbol{C}\boldsymbol{x}$. Equivalent, but different, Pitt-Peters-type dynamic inflow models may be obtained by the RMA of matrices $\hat{\boldsymbol{H}}_\Omega$, $\hat{\boldsymbol{H}}_\theta$ and $\hat{\boldsymbol{H}}_\beta$. Coupling Eq. 2.1 with the outcomes of Eq. 2.17 provides the time evolution of the wake inflow linear distribution on the rotor disc, as associated with rotor loads perturbations. Note that, if the model extraction is based on an aerodynamic solver capable of simulating the influence of kinematic perturbations on the wake shape, wake distortion effects are intrinsically accounted for in the corresponding $\lambda - f$ dynamic inflow model.

If not specified otherwise, the number of the poles utilized is the one that assure the best fit between the sampled transfer function and its RMA.

2.3 Models extension to advanced rotor configuration: coaxial contra-rotating rotors

In this section the extension of the proposed inflow models to coaxial rotors is presented. The inflow approximation is exactly the same of eq. 2.1 written for lower and the upper rotor disc:

$$\begin{aligned} v_i^{u,l}(r,\psi_i^{u,l},t) = v_0^{u,l}(r,t) + v_c^{u,l}(r,t)\cos\psi_i^{u,l} + v_s^{u,l}(r,t)\sin\psi_i^{u,l} + \\ + v_{N/2}^{u,l}(r,t)\,(-1)^i \end{aligned} \tag{2.18}$$

The expression of the inflow coefficients is still obtained with eq. 2.6 and clearly the same considerations on the differential coefficient can be done.

The first substantial difference between the coaxial inflow models and the one previously presented valid for a single rotor configuration is on the blade pitch control. Usually there is a distinction between the upper and lower pitch control law such that, for each rotor, the command pitch laws are defined and an azimuth distinction is done

$$\theta^u = \theta_0^u + \theta_c^u\cos\psi^u + \theta_s^u\sin\psi^u \tag{2.19}$$

$$\theta^l = \theta_0^l + \theta_c^l\cos\psi^l + \theta_s^l\sin\psi^l \tag{2.20}$$

Moreover, when it comes to deal with coaxial configuration, the command laws are usually given in terms of blade pitch and differential blade pitch defined respectively as $\theta^+ = (\theta^u + \theta^l)/2$ and $\theta^- = (\theta^u - \theta^l)/2$. Furthermore, considering the high flapping stiffness they preset, in order to preserve the clearance between rotors, perturbations on flapping variables are here neglected.

Thus, the linear time invariant kinematic based model $\lambda - q$ relates the inflow components $\boldsymbol{\lambda} = \{\boldsymbol{\lambda}_0^u\ \boldsymbol{\lambda}_s^u\ \boldsymbol{\lambda}_c^u\ \boldsymbol{\lambda}_0^l\ \boldsymbol{\lambda}_s^l\ \boldsymbol{\lambda}_c^l\}^T$ to blade pitch controls, $\mathbf{q}_\theta = \{\theta_0^+\ \theta_s^+\ \theta_c^+\ \theta_0^-\ \theta_s^-\ \theta_c^-\}^T$, hub linear and angular velocity components, $\mathbf{q}_{V\Omega} = \{u\ v\ w\ p\ q\ r\}^T$ such that:

$$\tilde{\boldsymbol{\lambda}} = \boldsymbol{H}_\theta\tilde{\boldsymbol{q}}_\theta + \boldsymbol{H}_{V\Omega}\tilde{\boldsymbol{q}}_{V\Omega} = \boldsymbol{H}(\omega)\tilde{\boldsymbol{q}} \tag{2.21}$$

where $\tilde{\boldsymbol{q}} = [\tilde{\boldsymbol{q}}_\theta\ \tilde{\boldsymbol{q}}_{V\Omega}]$ and $\boldsymbol{H}(\omega) = [\boldsymbol{H}_\theta\ \boldsymbol{H}_{V\Omega}]$ is a $[M \times N]$ transfer function matrix where $M = (N_{0,r}^u + N_{c,r}^u + N_{s,r}^u + N_{0,r}^l + N_{c,r}^l + N_{s,r}^l)$ and $N = 12$ are respectively the

number of outputs and inputs.

The linear time invariant load based model requires the identification of transfer functions $\boldsymbol{G}_\theta$ and $\boldsymbol{G}_{V\Omega}$ relating respectively the kinematic perturbations $\tilde{\boldsymbol{q}}_\theta$ and $\tilde{\boldsymbol{q}}_{V\Omega}$ to the rotor hub loads $\tilde{\boldsymbol{f}} = \{C_T^u\ C_L^u\ C_M^u\ C_T^l\ C_L^l\ C_M^l\}^T$.
As for the single rotor case, $\lambda - f$ model is considered only with the Pitt-Peters inflow distribution. Then, considering for instance the matrix $\boldsymbol{G}_{V\Omega}$, its inverse matrix is determined and the wake inflow coefficients are directly related to the rotor loads as follows:

$$\tilde{\boldsymbol{\lambda}} = \hat{\boldsymbol{H}}_{V\Omega}(\omega)\tilde{\boldsymbol{f}} \tag{2.22}$$

where $\hat{\boldsymbol{H}}_{V\Omega}(\omega) = \boldsymbol{H}_{V\Omega}(\omega)\hat{\boldsymbol{G}}_{V\Omega}(\omega)^{-1}$ is the $[6 \times 6]$ transfer function matrix (equivalent transfer function matrices $\hat{\boldsymbol{H}}_\theta$ and may be derived from $\hat{\boldsymbol{G}}_\theta$.

The linear time periodic version of the kinematic based model relates $\lambda - q$ relates the inflow components $\boldsymbol{\lambda} = \{\boldsymbol{\lambda}_0^u\ \boldsymbol{\lambda}_s^u\ \boldsymbol{\lambda}_c^u\ \boldsymbol{\lambda}_{N/2}^u\ \boldsymbol{\lambda}_0^l\ \boldsymbol{\lambda}_s^l\ \boldsymbol{\lambda}_c^l\ \boldsymbol{\lambda}_{N/2}^l\}^T$ to blade pitch controls, $\mathbf{q}_\theta$, hub linear and angular velocity components, $\mathbf{q}_{V\Omega}$ and blade elastic degrees of freedom $\boldsymbol{\zeta}$ such that:

$$\tilde{\boldsymbol{\lambda}} = \boldsymbol{MH}(\omega)\tilde{\boldsymbol{q}} \tag{2.23}$$

where $\tilde{\boldsymbol{q}} = [\tilde{\boldsymbol{\zeta}}\ \tilde{\boldsymbol{q}}_\theta\ \tilde{\boldsymbol{q}}_{V\Omega}]$ and $\boldsymbol{MH}(\omega)$ is a $[(2n_h+1)M \times N]$ transfer function matrix where $M = (N_{0,r}^u + N_{c,r}^u + N_{s,r}^u + N_{N/2,r}^u + N_{0,r}^l + N_{c,r}^l + N_{s,r}^l + N_{N/2,r}^l)$ and $N = (9 + N_\zeta)$ are respectively the number of outputs and inputs of the linear time periodic kinematic based model for coaxial rotor.

Finally by the RMA algorithm the state-space representation of the models are obtained from the eqs. 2.21,2.23 and 2.22 and are exactly like eqs. 2.15 and 2.17 with the only difference in the matrix dimensions. Indeed considering the linear time invariant kinematic based model $\lambda - q$, the dimension of the RMA matrices are: $[\boldsymbol{A}_1] = [\boldsymbol{A}_0] = [M \times N]$, $[\boldsymbol{A}] = [N_a \times N_a]$, $[\boldsymbol{B}] = [N_a \times N]$ and $[\boldsymbol{C}] = [M \times N_a]$. where M

and N are respectively the number of outputs and inputs of the linear time invariant transfer function.

For the linear time invariant load based model $\lambda - f$ the RMA matrix dimensions result: $[\boldsymbol{A}_0] = [6 \times 6]$, $[\boldsymbol{A}] = [N_a \times N_a]$, $[\boldsymbol{B}] = [N_a \times 6]$ and $[\boldsymbol{C}] = [6 \times N_a]$.

In case of the linear time periodic kinematic based model the matrix dimensions are: $[\boldsymbol{A}_1] = [\boldsymbol{A}_0] = [(2n_h + 1)M \times N]$, $[\boldsymbol{A}] = [N_a \times N_a]$, $[\boldsymbol{B}] = [N_a \times N$ and $[\boldsymbol{C}] = [M \times N_a]$ where M and N are respectively the number of outputs and inputs of the linear time periodic transfer function.

When a high fidelity solver is used to perform aerodynamic simulations, all the interference effects between upper and lower rotors are naturally included in the present models. Indeed, comparing the coaxial inflow models with the single main rotor one, there is no need to add some artificial terms that can take into account the mutual interaction between the upper and the lower rotor, because all the interaction phenomena deriving from the aerodynamic solution provided by the high fidelity solver are directly included into the models.

Chapter 3

Dynamic Wake Inflow Models Extraction

The non-parametric system identification for the characterization of high fidelity computational aerodynamics solvers is the main focus of this work. In the present chapter two system identification methodologies developed and employed are presented. The first one is based on single harmonic response of the system while the second is based on response of a sweep input signal usually called chirp. By applying the two it techniques is possible to accurately estimate the linear time invariant behavior of a generic non-linear dynamical system such as the aerodynamic operator of an helicopter. If on one side the first method allow to extract the time invariant model also when time periodic system are dealt with, on the other hand an innovative extension of the chirp excitation method to LTP systems is here presented.

Both the approaches are applicable under the fundamental condition that the system for which the extraction is performed is stable. In particular, regarding the isolated rotor system presented in this work, the condition is its aerodynamic stability at the steady flight condition for which the transfer function matrices are identified. Since the methodologies are applicable to any system identification problem and represent a part set of tools developed in this work, the processes are described for a generic system characterized by a $G(\omega)$ transfer function relating an input u and an output y.

3.1 Single frequency excitation method for linear time invariant transfer function extraction

The proposed method to extract the LTI transfer function consists in the following steps:

- Application of single-harmonic, small perturbation of each input variables $u(t)$;
- Evaluation in the frequency domain of the harmonic components of the resulting output $y(t)$ having the same frequency of the input. In particular the corresponding complex values of the frequency-response functions are determined;
- Reiteration of the process for a discrete number of frequencies within a defined range, so as to get adequate sampling of the frequency response matrix, $G(\omega)$, for the specific case examined;

However, time periodic systems yield multi-harmonic outputs even with a single harmonic signal as input. The same is commonly true for nonlinear systems. Thanks to the extraction of the output components at the same frequency of the input perturbation, a constant-coefficient approximation of the operators relating y to u is obtained. Moreover, the linearization of the system is obtained utilizing a sufficiently small input. The capability and simplicity of isolating and eliminating the time periodicity and non linearities effects is the main advantage of this identification approach. In order to apply this identification methodology, the following issues have to be taken care of: [35]

- In order to isolate the output harmonic response, the signal record must start when the transient due to the application of the perturbation is vanished.
- To avoid leakage effects the period examined is an integer multiple of the input harmonic period.
- A sufficiently long period is recorded to reduce the effects of leakage.
- If a substantial random noise is present in the output signal an ulterior increase of the length of the recording period is performed. Then a noise reduction can

be performed by mediating various periodograms during the frequency domain analysis in the second step of the identification process;

In order to estimate the quality of the identification, the power coherence function $\gamma_P(\omega_i)$ can be introduced as:

$$\gamma_P(\omega_i) = \frac{|Ip_{yu}(\omega_i)|^2}{Ip_{yy}(\omega_i)Ip_{uu}(\omega_i)} \in [0,1] \tag{3.1}$$

where $I_{P_{yx}}$ denotes the integral of the corresponding input-output cross-spectral density, $I_{P_{xx}}$ and $I_{P_{yy}}$ are, respectively, power of input and output signals (namely, the integrals of the corresponding power spectral densities). The function γ_P is a particular measure of linearity and time invariance of the system, as well as of the presence of noise. For a noiseless harmonic response of a LTI system $\gamma_P = 1$, while it is less than one for systems where noise and nonlinearities are present.

The single frequency excitation method, if correctly implemented, offers a very robust approach for the non-parametric transfer function identification even for a time-periodic system (BLTI): it automatically deals with time-periodicities and most nonlinearities, and it can deal with a noisy output as well. However these features may come at a price; the need for the extinction of the transient and the length of the recorded periods may rapidly increase the computational cost of the identification when applied to system with a large time constant (thus a long transient) and/or with particularly noisy output. Furthermore it is worth noting that the computational cost increase as $O(N_f)$ where N_f represents the number of analyzed frequencies. For this reason in the next section a method with a smaller computational cost, yet less robust, will be presented.

3.2 Chirp excitation method for linear time invariant transfer function extraction

In the previous section the advantages of an identification technique based on single frequency excitation were discussed. However this approach has an important drawback: it usually requires long simulations to be able to sample a wide spectrum of frequencies. In fact to get a single sample of a column of the transfer function matrix (the effect of an input on all the outputs) for a certain frequency $\breve{\omega}$, a simulation time larger than the

slowest time constant is needed for the transient effects to become negligible. As the value of $\check{\omega}$ increases the useful part of simulation time (proportional to $1/\check{\omega}$) becomes comparable or even smaller than the the time spent on waiting for the transient to vanish. To overcome this efficiency issue an approach often used in system identification is perturbing the system with a signal whose frequency changes with time. The approach presented in this section uses a so called 'chirp' signal as input. This methodology is widely used for system identification, however is not suitable for the extraction of the BLTI in a time-periodic system. An extension for the robust application to LTP systems will be presented in the next section.

The main characteristic of a chirp signal is the full band spectrum. This characteristic is shared with impulse input with the advantage of having a much smaller maximum amplitude of the signal for the same frequency spectrum module; a small amplitude of the signal is fundamental when a linear behavior of the system is sought as in the present case. A simple chirp signal can be defined as an harmonic signal whose frequency varies in time. For example:

$$u(t) = sin(f(t)t + \phi) \tag{3.2}$$

where the function $f(t)$ defines how the frequency is swept along the chirp. In particular the frequency $\omega(t)$ can be defined as

$$\omega(t) = \frac{d[f(t)t]}{dt} = t\frac{d[f(t)]}{dt} + f(t) \tag{3.3}$$

In real applications the chirp spectrum is limited in a band between a minimum and a maximum frequency and it depends on the choice of the frequency function $f(t)$.

The quality of the identification depends on the choice of the frequency functions. It is really important to excite all the frequencies under examination for a sufficient amount of time. Figure 3.1 shows a linear and a quadratic chirp alongside their spectrogram. Usually, in order to capture the lowest frequencies behavior of the system, a quadratic frequency function instead of a linear one is recommended. This is because the lowest frequencies require more excitation time to be well captured. Moreover a good practice when creating an input chirp signal is having a decreasing amplitude at the end of the signal and to zero-pad it further for at least a duration equal to the slowest dynamics of the excited system. In this way both the input and the output will

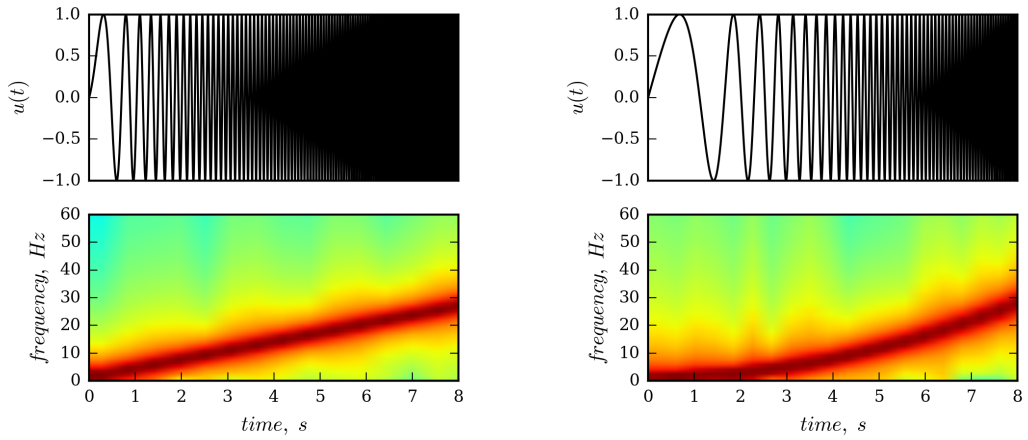

(a) Linear chirp

(b) Quadratic chirp

Figure 3.1: Example of linear and quadratic chirp signal and their spectrogram, with a frequency band from 0 to 32 Hz

be less affected by the windowing effects introduced by the discrete Fourier Transform. In figure 3.2 an example of chirp signal utilized in this work and its frequency spectrum are depicted. The dashed vertical line in the right part of figure 3.2(b) indicates the maximum frequency at which the system is adequately excited, while the decreasing nature of the signal band is caused by the quadratic nature of $f(t)$.

However, the chirp method cannot provide an accurate estimation of the static derivatives like the single frequency method. For this purpose, it is recommended to evaluate it by applying to the system a small, constant valued perturbation and measuring the output variation. In other words, by applying a simple numerical differentiation.
The extraction of the non-parametric transfer function with the chirp excitation method consists in the following steps

- Application of small chirp signal input $u(t)$, in the frequency range of interest
- Evaluation of the transfer function $G(\omega)$ by the ratio between the discrete Fourier Transform of the output and the input

$$G(\omega) = \frac{\mathcal{F}(y(t))}{\mathcal{F}(u(t))} \tag{3.4}$$

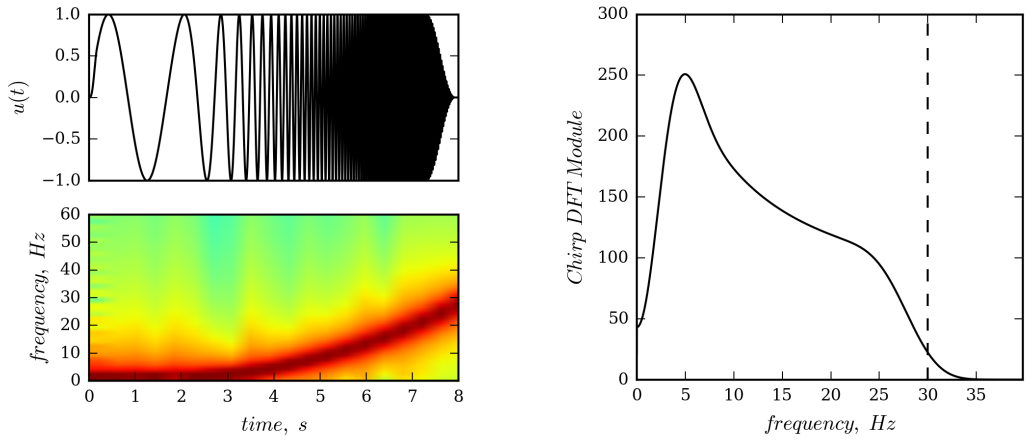

(a) Time history and spectrogram

(b) Discrete Fast Fourier module

Figure 3.2: Example of quadratic chirp signal with a frequency band from 0 to 32 Hz

The application of the $\mathcal{F}$ gives a good estimation of the transfer function when the output signal is not affected by noise and when the windowing artifacts are negligible for both signals. While it is possible to reduce the artifacts introduced by the windowing of the signal, it is often impossible to eliminate all the noise sources from the output. To reduce the influence of the random noise on the quality of the estimation a second approach for the analysis of the chirp output can be employed: the power spectral densities of the signals are considered instead of their $\mathcal{F}s$, [38]. In particular the transfer function between an input u and an output y is defined as

$$G(\omega) = \frac{\Phi_{yu}(\omega)}{\Phi_{uu}(\omega)} \tag{3.5}$$

where Φ_{yu} and Φ_{uu} are the input-output cross spectral density (CSD) and the power spectral density (PSD) of the input respectively. Recalling the definition of the cross and power spectral densities it can be shown that the zero mean random noise is filtered by the application of the cross spectral density operator. Instead of the $\mathcal{F}$, a sophisticated generalization, called the Chirp Z-Transform $\mathcal{CZT}$, is used [39]. Such a transform has a great flexibility in that the number of the output points, spacing and range is completely arbitrary (although the frequency resolution is still limited by the total sampling time, similar to the $\mathcal{F}$). Due to its flexibility, it is used to obtain a more finely spaced interpolation of the portion of the spectrum under examination.

It is worth noting that, similarly to the single frequency-response method previously presented, a noisy signal imposes a longer duration of the simulation to be able to maintain a sufficient frequency resolution due to the application of the periodogram method. Even if longer simulation times may be able to effectively mitigate the negative effect of the noise on the identification accuracy, this method, as presented, does not offer an effective way to filter out the multi-harmonic effects caused by nonlinearities time periodic behavior of the operator. In particular this second issue is of fundamental importance for the objectives of this work and a solution will be presented in the next section.

To obtain an indication of the quality of the identification in terms of impact of output noise and effects of certain nonlinearities the coherence between the input and the output can be used [40]. The coherence between two signals $u(t)$ and $y(t)$ is defined as:

$$C_{yu}(\omega_i) = \frac{|P_{yu}(\omega_i)|^2}{P_{yy}(\omega_i)P_{uu}(\omega_i)} \in [0,1] \tag{3.6}$$

and it varies between zero and one. An unitary, or almost unitary, coherence is an indication of a linear correlation between the two signals and hence it may indicate that the transfer function was correctly identified. A low coherence may indicate a high noise-to-signal ratio, the presence of certain kinds of nonlinearities, an insufficient excitation of a particular range of frequencies, or simply a zero of the system.

3.3 Extended single frequency excitation method to linear time periodic transfer function extraction

In section 3.1, a procedure for the extraction of the LTI transfer function using single-harmonic perturbation of the input has been presented. Using this procedure it is also possible to evaluate the Zadeh's harmonic transfer function. The method is based on the a priori knowledge of the intrinsic periodicity of the system ω_p and consists in the following steps:

- Application of single-harmonic perturbation of the input $u(t)$ of frequency ω ;
- Evaluation of the harmonic components of the resulting output $y(t)$ having the same frequency of the input, ω, and the one due to the periodicity of the system

$\omega + n\omega_p$. In particular the corresponding complex values of the frequency-response functions are determined;

- Reiteration of the process for a discrete number of frequencies within a defined range, so as to get adequate sampling of the frequency response matrix, for the specific case examined.

The capability of immediately isolating the effects of the time periodicity of operators is the main advantage of this identification approach. Some care is however needed if particular frequencies are analyzed. Indeed considering that the output of a LTP system, excited by a sinusoid with frequency ω, consists in a superposition of sinusoids at frequencies $[\omega, \omega_p \pm \omega, 2\omega_p \pm \omega, ...]$. An excitation frequency $\omega = \omega_p/2$ gives as output:

$$\left[\omega_p/2|_{\omega}, 3\omega_p/2|_{\omega_p+\omega}, \omega_p/2|_{\omega_p-\omega}, 5\omega_p/2|_{2\omega_p+\omega}, 3\omega_p/2|_{2\omega_p-\omega}, ...\right] \tag{3.7}$$

that is

$$\left[\omega_p/2|_{\omega_p-\omega}^{\omega}, 3\omega_p/2|_{2\omega_p-\omega}^{\omega_p+\omega}, 5\omega_p/2|^{2\omega_p+\omega}, ...\right] \tag{3.8}$$

where $|_*^{\square}$ simply shows the result of the combination between the excitation and n-pumping frequencies.

As one can see, there is no way to distinguish the origin of the harmonic component of the output. In order to avoid this problem it is advisable to exclude from the analysis frequencies in the set $\omega \in [\omega_p/2, \omega_p, 3\omega_p/2, 2\omega_p, ...]$.

3.4 Extended chirp-based excitation method to linear time periodic transfer function extraction

In section 3.2, a procedure for the identification of LTI system using an input signal having a band spectrum has been presented. Using this procedure it is possible to extract the transfer functions for the frequencies comprised inside this band by using a single perturbation for each input. However this methodology suffers from an accuracy loss when applied to time-periodic systems. The reason for this limitation is due to the fact that there is no way to distinguish if an harmonic component of the output, having a frequency inside band spectrum of the input signal, is the result of the response of a

LTI system excited at the same frequency or is the result of a time periodicity of the system. For this reason, more information than those given by a single perturbation of the system are needed to carry out a correct an harmonic transfer function identification. An important characteristic of LTP systems is that the output signal depends not only on the input signal, but also on the phase of the input signal with respect to the internal system phase. In [41, 42] an identification methodology exploiting this characteristic is presented: the idea is to apply the same input to the time periodic system multiple times, with different delays T with respect to the beginning of a system period. By properly analyzing the various outputs it becomes possible to differentiate between the effects of the various harmonic transfer functions. Two approaches are proposed in [42] for the actual identification of the harmonic transfer function: a first approach employing the discrete Fourier transformation, suffering from all the noise related issues described in section 3.2, and a second approach using an ill defined power/cross spectral density along with an heuristic assumption on smoothness of the transfer functions.
An alternative approach is here presented. Recalling the definition of the harmonic transfer function $\boldsymbol{MH}$ given in 2.8, it is possible to write the output of a LTP system excited by an input $u(t)$ as

$$y(t,T) = y^0(t) + \sum_{m=1}^{n_h} [y^{mc}(t)cos(m\omega_p(t+T)) + y^{ms}(t)sin(m\omega_p(t+T))] \tag{3.9}$$

This equation is equivalent to equation 2.7, written for a generic output $y(t)$ and the only difference being the explication of the dependency of the output on the delay T . The Laplace transform of each of the output components y^{mc}, y^{ms}, is in turn given by equation 2.9. If the system under examination is real and the signals $y^0(t)$, $y^{mc}(t)$, $y^{ms}(t)$ can be isolated, it would be possible to apply the methodology developed in 3.2 for identifying the multiharmonics blocks $MH_0(\omega)$, $MH_{mc}(\omega)$, $MH_{ms}(\omega)$. The decomposition of the output signal, described in equation 3.9, can be carried out in the time domain or in the frequency domain. The former approach is employed here. Therefore, in order to identify a finite number of harmonics, n_h, of the **MH**, the following steps are performed

- The system is perturbed multiple times, $N_t \geq 2n_h+1$, with the same chirp signal.

The perturbation is applied to the system after different delays from the steady response, $T_i = i\dfrac{T}{2n_h+1}$, and the outputs $y(t,T_i)$ are recorded.

- For every time step the following linear system is solved:

$$R(t)\begin{bmatrix} y^0(t) \\ y^{1c}(t) \\ y^{1s}(t) \\ \vdots \\ y^{n_h c}(t) \\ y^{n_h s}(t) \end{bmatrix} = \begin{bmatrix} y(t,T_1) \\ y(t,T_2) \\ y(t,T_3) \\ \vdots \\ y(t,T_N) \end{bmatrix} \tag{3.10}$$

and the output components are identified. The matrix $R(t)$ is defined as:

$$R(t) = \begin{bmatrix} 1 & cos(\omega_p\phi_1) & sin(\omega_p\phi_1) & cos(\omega_p\phi_1) & sin(\omega_p\phi_1) \\ 1 & cos(\omega_p\phi_2) & sin(\omega_p\phi_2) & cos(\omega_p\phi_2) & sin(\omega_p\phi_2) \\ 1 & cos(\omega_p\phi_3) & sin(\omega_p\phi_3) & cos(\omega_p\phi_3) & sin(\omega_p\phi_3) \\ \vdots & \vdots & \vdots & \vdots & \vdots \\ 1 & cos(\omega_p\phi_{N_T}) & sin(\omega_p\phi_{N_T}) & cos(\omega_p\phi_{N_T}) & sin(\omega_p\phi_{N_T}) \end{bmatrix} \tag{3.11}$$

where $\phi_i = t + T_i, \quad i = 1, ..., N_T$

- For each output components the 3.4 gives the transfer function relating the identified coefficient to the applied input

$$\begin{bmatrix} y^0 \\ y^{1c} \\ y^{1s} \\ \vdots \\ y^{n_h c} \\ y^{n_h s} \end{bmatrix} = \boldsymbol{MH}(\omega)u \tag{3.12}$$

Chapter 4

Numerical results

In this chapter numerical results concerning the identification of the wake inflow models and their application are presented. The models are obtained by applying system identification techniques to high fidelity aerodynamic solvers based on Boundary Element Method for the solution of a boundary integral equation approach, suited for the analysis of potential flows around helicopter rotors in arbitrary flight conditions, included those where strong blade-vortex interactions occur (see appendix B). The utilized aerodynamic tool offers a local time history over the rotor blades of the induced velocity evaluated by the Biot-Savart law. With the aim of developing a dynamic inflow model to be coupled with two dimensional aerodynamic models the inflow is evaluated for each section at 3/4 of the local chord of the blades.

In order to validate the capabilities of the wake inflow approximation and the extraction methodology, the single main rotor of the Bo-105 helicopter and a coaxial rotor configuration representative of the Sikorsky S-69 helicopter are analyzed. Table 4.1 summarizes the rotors and helicopter principal properties. The coaxial rotor test case is analyzed both for the validation of the presented methodology in presence of a complex aerodynamic solution due to the strong mutual aerodynamic interference between the rotors and also to demonstrate the versatility of the proposed method for any kind of helicopter rotor.

The quality of eq. 2.1 is investigated for a static perturbation starting from the Pitt-Peters like approximation up to a most complex and complete representation. Then

wake inflow transfer functions and their rational approximation are examined. First, the linear time invariant version of the $\lambda - q$ and $\lambda - f$ model is presented considering the Pitt-Peters like inflow approximation. In addition, for the Pitt-Peters like model, the influence of the type of kinematic perturbations used for its identification is discussed. Then the time periodic version of the $\lambda - q$ model is presented taking into consideration a detailed description of the wake inflow suitable for aeroelastic analysis.
Time marching validation of the proposed models are presented in order to test their capabilities of predicting wake inflow caused by arbitrary kinematic perturbations.
Finally the time invariant models are applied to helicopter flight mechanics analyses. If not specified otherwise, the rotor wake in the aerodynamic BEM solver is assumed to have a prescribed shape that, in forward flight, coincides with the surface swept by the trailing edges, whereas in hovering it becomes an helicoid with spiral length given by the mean trimmed inflow. Although the crucial role played by the free wake algorithm to provide a realistic wake shape is discussed, note that prescribed wake prediction can be conveniently applied to show the capabilities of the wake inflow approximation and the state space extraction. In addition, all the results presented concern non-dimensional quantities (unless otherwise specified): linear velocities are divided by the factor ΩR, angular velocity are divided by Ω, while angles are expressed in degrees. If not specified otherwise the trimmed flight conditions of hovering and forward flight at advance ratio $\mu = 0.2$ are analyzed for both the rotor configuration. The trim conditions are related to the helicopter weights and a momentum trim condition is considered in forward flight case.

	Bo105	S-69	
Helicopter weight	24525	50000	N
MR System	hingeless	hingeless	
MR Number of Rotors	1	2	
MR Number of Blades per Rotor	4	3	
MR Rotor Rotational Direction	CCW	CCW upper CW lower	
MR Destined Rotor Speeds	44.4	32.8	rad/s
MR Blade Crossing	-	$\Psi = 30 + 60n$	$\circ$
MR Hub Separation	-	0.76	m
MR Radius	4.91	5.48	m
MR Root Cut Off	1	1.1	m
MR Chord	0.27	0.54	m
MR Taper Ratio	1	0.5	
MR Twist	-8	-7	$\circ$/m
TR Radius	1	-	m
TR Chord	0.2		m
TR Destined Rotor Speeds	230	-	rad/s
TR Number of Blades	2	-	
I_{xx}	1430	-	$kg\,m^2$
I_{yy}	4975	-	$kg\,m^2$
I_{zz}	4100	-	$kg\,m^2$
I_{xz}	650	-	$kg\,m^2$

Table 4.1: Rotors properties

4.1 Approximated representation of wake inflow

First, considering the rotor in hovering condition, the accuracy of the inflow representation of Eq. 2.1 is investigated. Initially, for the Bo105 rotor, the linear Pitt-Peters like representation is analyzed. Figure 4.1(a) shows the computed wake inflow distribution normalized with respect to its maximum, v_B, caused by stationary axi-symmetric perturbations along with the inflow approximation v_i. It is the worth noting that the inflow approximation of eq. 2.1 can be always evaluated from the computed induced velocity independently of the introduction of a finite-state description for its coefficients. .

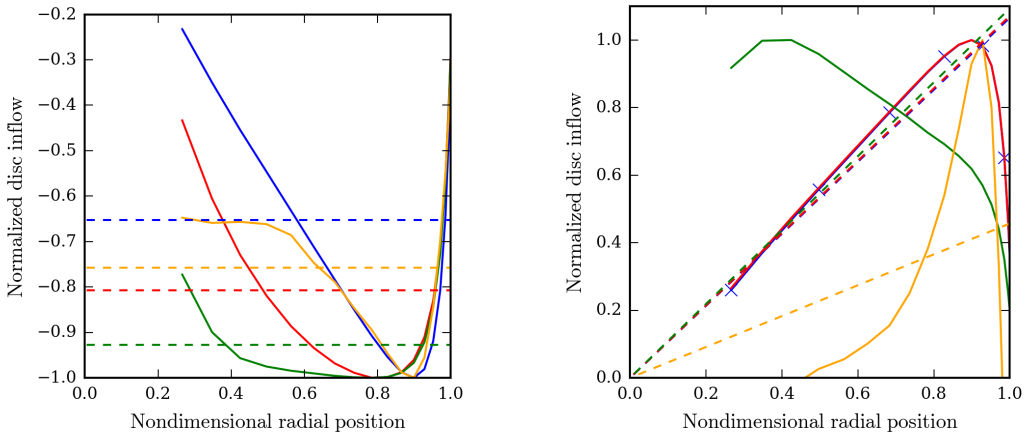

(a) Axi-symmetric perturbations of θ_0,r, w,β_0

(b) Non axi-symmetric perturbations of θ_s,p, u,β_s

Figure 4.1: Distribution of wake inflow perturbations on blades at $\psi = \pi/2$. —— v_B, - - - v_i Hovering Condition.

It is interesting to observe that different perturbations provide normalized inflow distributions that are remarkably different. In particular, a perturbation of the collective pitch, θ_0, induces an inflow distribution with a significant (axi-symmetric) radial gradient, whereas the inflow caused by the axial velocity perturbation, w, is almost constant spanwise (except for the three-dimensional effects at the blade root and tip regions) and thus may be satisfactorily approximated by the Pitt-Peters like representation. Figure 4.1(b) presents the wake inflow distribution produced by non axi-symmetric stationary perturbations on the blade located at $\Psi = \pi/2$. In this case, the normalized inflow distributions caused by p and θ_s are almost identical and, neglecting the three dimensional effects at the blade tip, can be satisfactorily approximated by a linear distribution, whereas that induced by u and β_s presents radial variations that cannot be satisfactorily reproduced by eq. 1.1. Similarly consideration can be done on fig.4.2 where the computed wake inflow distribution on the coaxial rotor blades caused by stationary perturbations of blade pitch controls variables are shown.

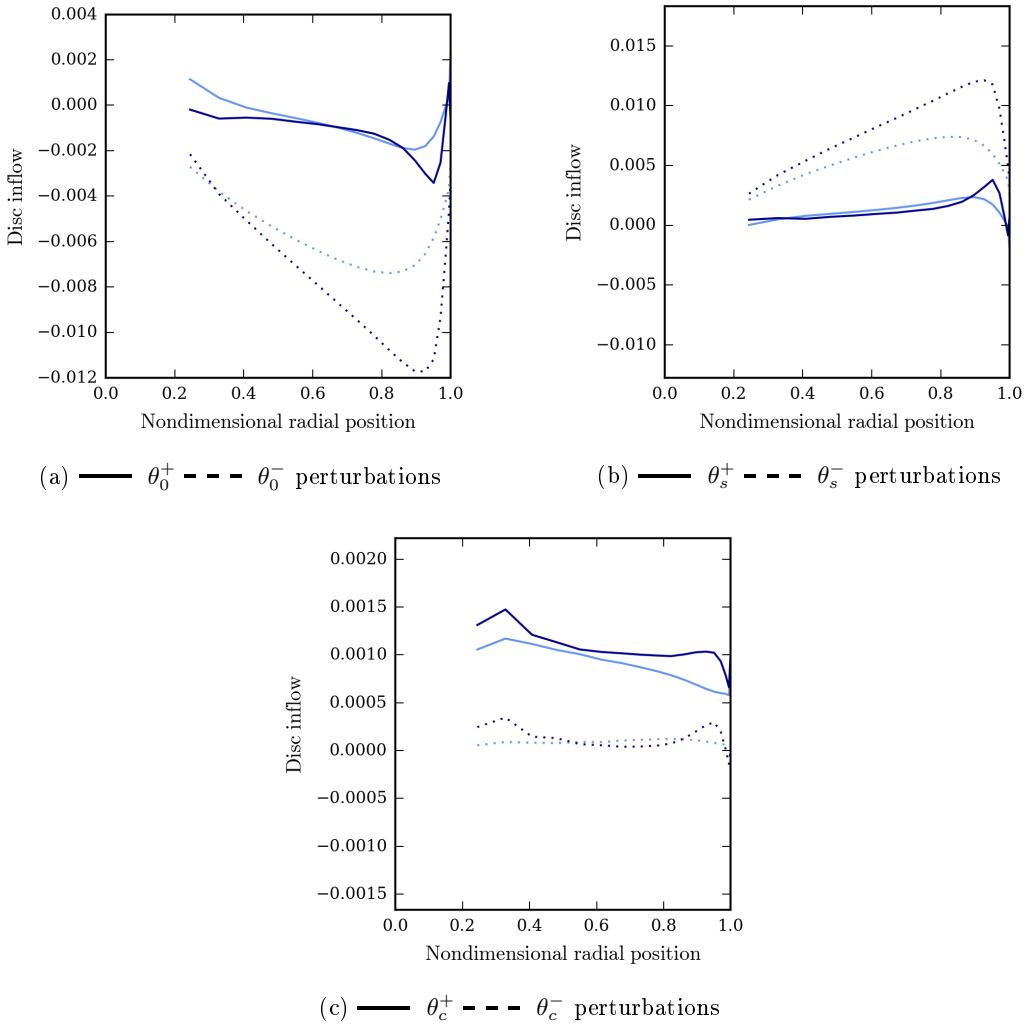

Figure 4.2: Distribution of wake inflow perturbations, v_B, on blades at $\psi = \pi/2$. upper rotor lower rotor. Hovering condition.

Figure 4.2(a) shows the computed wake inflow radial distributions, $v_B^{u,l}$, caused by stationary perturbations of $\theta_0^{\pm}$ evaluated on the blade when passing at azimuth locations $\psi = \pi/2$. Figures. 4.2(b) and 4.2(c) present the computed wake inflow due to perturbations of average and differential longitudinal and lateral pitches namely, $\theta_c^{\pm}$ and $\theta_s^{\pm}$. Comparing figs. 4.2(b) and 4.2(c), it is worth noting that, unlike the single rotor case where the wake inflow response to θ_c tends to be negligible on blades passing at $\psi = \pi/2$ and $\psi = 3\pi/2$ perturbations of differential θ_c produce inflow

comparable with that generated by perturbations of differential θ_s, thus revealing that remarkable coupling between the cyclic components of inflow and blade pitch controls occurs in coaxial rotors. It is evident that the Pitt-Peters like linear inflow representation can provide only a rough approximation of the perturbed inflow distribution both for single and coaxial configuration. These observations are confirmed by fig. 4.3, that shows wake inflow distributions on a coaxial rotor blades during one revolution, induced by stationary blade pitch perturbations. In figs. 4.3(a) and 4.3(b), wake inflow on upper and lower rotors caused by an steady axi-symmetric perturbation present both azimuthal $6/rev$ periodicity and radial gradients that cannot clearly be captured by 1.1.

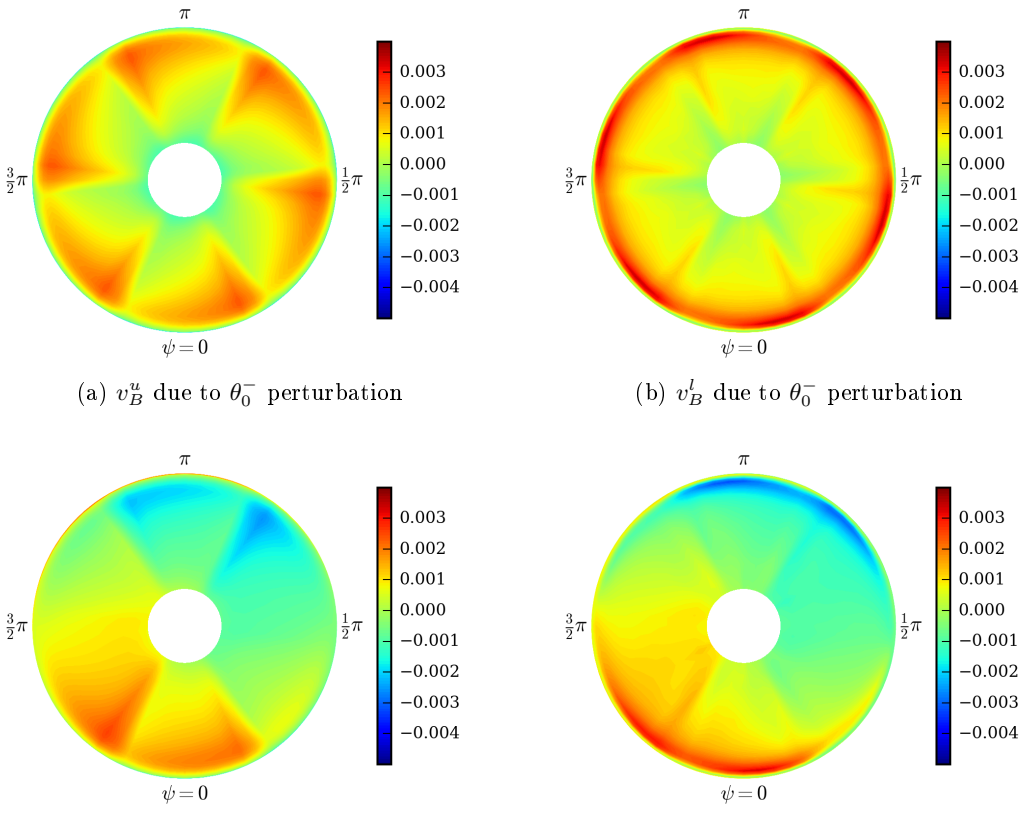

(a) v_B^u due to θ_0^- perturbation

(b) v_B^l due to θ_0^- perturbation

(c) v_B^u due to θ_c^- perturbation

(d) v_B^l due to θ_c^- perturbation

Figure 4.3: Distribution of wake inflow perturbations, $v_B^{u,l}$ over coaxial rotor discs. Hovering Condition.

In particular, such $6/rev$ periodicity is a peculiar outcome of the interactions be-

tween the two rotors, not occurring in single rotor configurations. It is due to blade passage (on upper and lower rotors) and wake passage (mainly of upper rotor wake on lower rotor). Similar conclusions are drawn from figs. 4.3(c) and 4.3(d) depicting upper and lower disc distributions of inflow on rotor blades due to (non-axisymmetric) steady perturbations of differential cyclic pitch, θ_c^-. In this case, the azimuth direction $45° - 225°$ may be roughly identified as the line of separation between upward and downward inflow regions (it might be observed that, for single rotors, this line roughly coincides with the direction $90° - 270°$)
In forward flight it is expected that the inflow distribution became more complex. Indeed fig. 4.4 shows the complexity of inflow distribution due to θ_c^- perturbations.

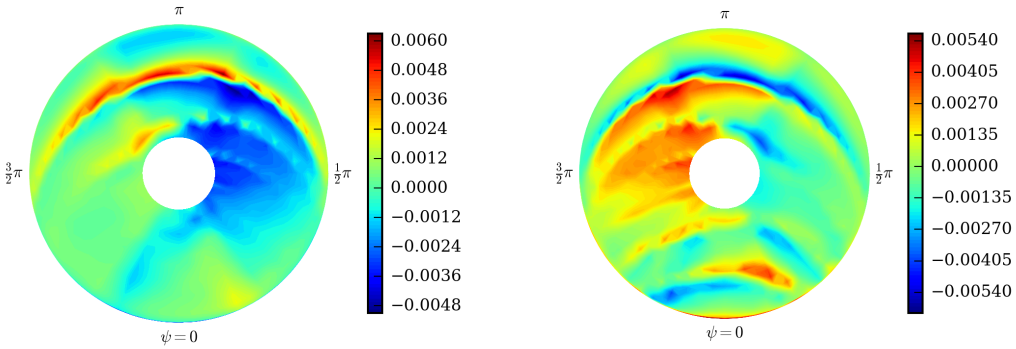

(a) v_B^u due to θ_c^- perturbations

(b) vl_B due to θ_c^- perturbations

Figure 4.4: Distribution of wake inflow perturbations, v_B, over coaxial rotor discs. Forward flight condition.

The azimuth $6/rev$ periodicity is hidden by the superimposed $3/rev$ effects of the two three-blade wake structures deployed backward. The traces of the wake tip vortices appearing within the discs area because of the forward motion wake skew effect can be only roughly approximated by a linear representation.

Despite the observations regarding the accuracy of wake inflow representations, it is important to recall that the suitability of wake inflow approximations is strictly related to the applications they are thought for. For instance, it is well known that, although not providing a detailed representation of the wake inflow, the Pitt-Peters like approx-

imation is commonly applied for flight dynamics applications involving low-frequency simulations. However, in order to take into account higher order radial distributions and higher-harmonic azimuthal distributions, useful for higher-frequency aeroelastic applications, eq. 2.1 is considered. Dividing the blade span into a number of finite segments, the basis functions used in eq. 2.6 are such to provide a linear distribution of inflow coefficients within each segment assuring continuity at their edges. Considering $N_r^0 = N_r^c = N_r^s = N_r^{N/2} = 4$, $\phi_j^0 = \phi_j^s = \phi_j^c = \phi_j^{N/2}$, fig. 4.5(a) shows the computed normalized wake inflow distribution and its approximation on a single rotor blade, due to the same perturbation θ_0 considered in fig. 4.1. In particular, both the Pitt-Peters like and the present model approximation are shown. An overview of the relevant en-

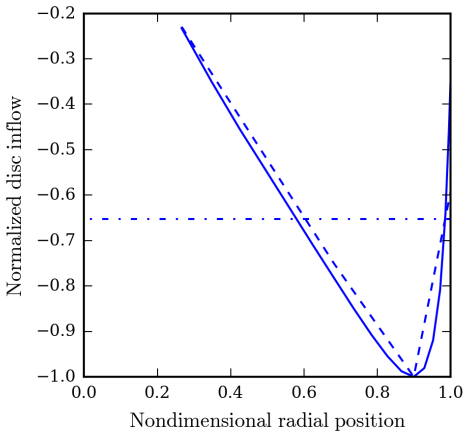

(a) v_B and v_i distributions due to θ_0 perturbation

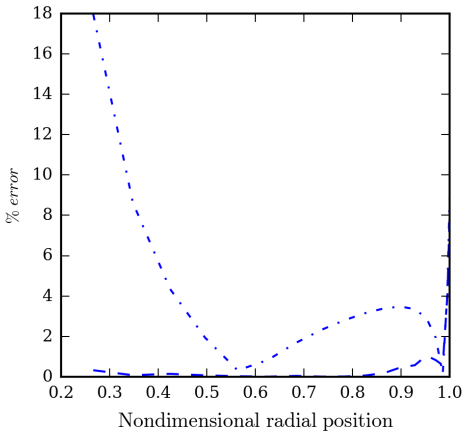

(b) Spanwise error v_i distributions.

Figure 4.5: Distribution of wake inflow perturbations —— v_B on blades at $\psi = \pi/2$ and its approximation v_i - - - present model considering four identical shape functions of the inflow coefficients -·-·- Pitt-Peters like (left). Spanwise error distribution (right). Hovering Condition.

hancement introduced by the radial approximation proposed is given in fig. 4.5(b). It presents the spanwise distributions of the percentage of the error rms with respect to computed inflow sectional inflow peak. The improvement of the inflow prediction provided by eq. 2.1 is considerable throughout the blade span. A similarly improvement is obtained for all the other perturbations.

Figure 4.6 shows the computed normalized wake inflow distribution and its approxima-

tion respectively on the upper and lower blades of the coaxial configuration, at $\Psi = \pi/2$, due to a stationary perturbation of θ_0^- in forward flight condition.

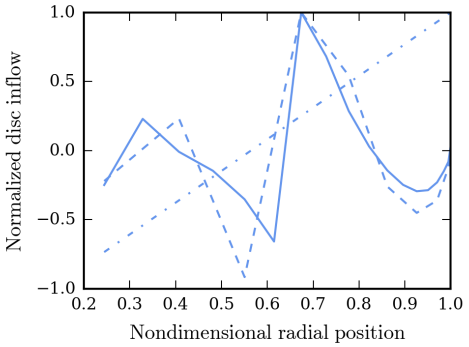

(a) v_B^u and v_i^u distributions due to θ_0^- perturbation

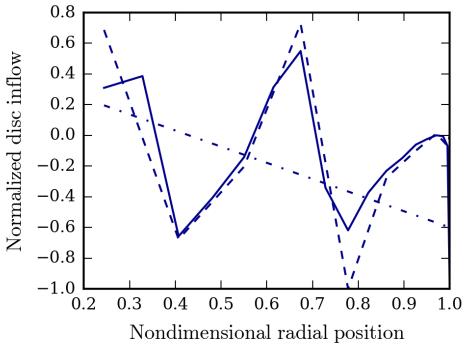

(b) v_B^l and v_i^l distributions due to θ_0^- perturbation

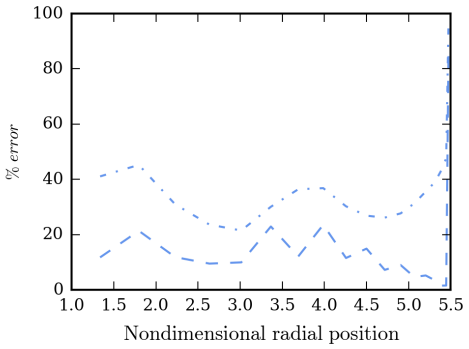

(c) Spanwise error v_i^u distributions.

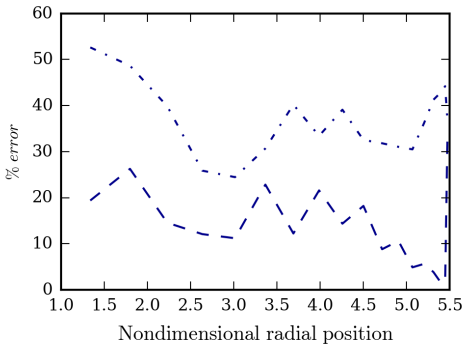

(d) Spanwise error v_i^l distribution.

Figure 4.6: Distribution of wake inflow perturbations v_B ——— upper rotor ——— lower rotor on blades at $\psi = \pi/2$ and its approximation $v_i^{u,l}$(- - - present model considering four identical shape functions of the inflow coefficients - · - · - Pitt-Peters like) **(top)**. Spanwise error distribution **(bottom)**.

Even if the inflow distribution in forward flight is particularly irregular, the improvement introduced by the radial approximations is still considerable as illustrated by figs. 4.3(c) and 4.3(d). Figure 4.7)(a) shows the wake inflow distribution on upper and lower rotor blades during one revolution induced by the same perturbation of fig. 4.6 alongside its radial approximation. Although using a greater number of shape functions will increase the capability of reproducing the inflow over the rotor discs, fig. 4.7(b) shows

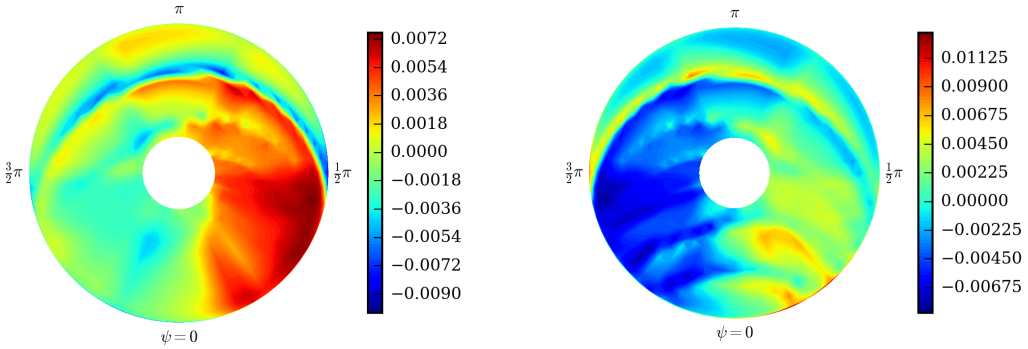

(a) v_B^u due to θ_0^-

(b) v_B^l due to θ_0^-

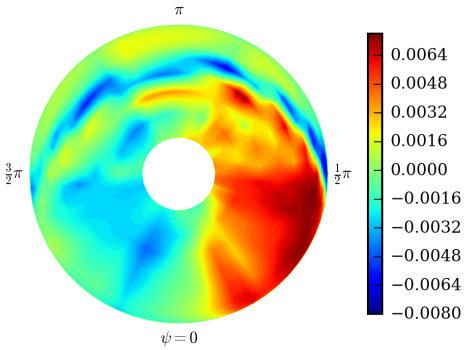

(c) v_i^u due to θ_0^-

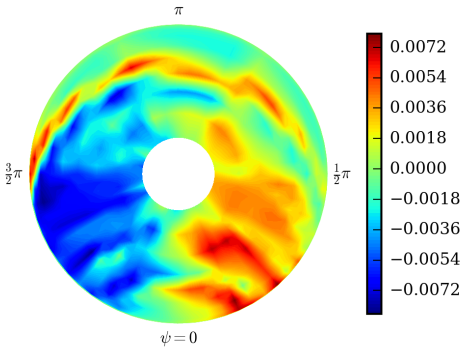

(d) v_i^l due to θ_0^-

Figure 4.7: Distribution of wake inflow perturbations, v_B **(top)**, and its approximation considering four identical shape functions of the inflow coefficients $v_i^{u,l}$ **(bottom)** over coaxial rotor discs. Forward flight condition.

that four shape function for each inflow coefficients can reproduce with a good level of accuracy all the higher order radial distributions.

4.2 Linear Time Invariant models

The transfer functions of the linear time invariant models and their RMA are here examined. In particular the models relating the kinematics input to inflow coefficients and the rotor hub loads to the inflow coefficients are presented both for hovering and forward flight condition for single and coaxial rotor configurations.

V-q model identification and rational matrix approximation

In order to investigate the difference in terms of transfer functions between the various type of perturbations, the Pitt-Peters like linear inflow approximation is considered. Being the time invariant model and eq. 1.1 particularly recommended for flight mechanics simulations, if not otherwise specified the frequency range examined is between $[0 - 0.5/rev]$.

Hovering rotor

For symmetry reasons, in hovering condition only the transfer functions relating λ_0 to axi-symmetric perturbations, and the transfer functions relating λ_s and λ_c to non axi-symmetric perturbations are significant. Specifically, fig. 4.8 shows the sampled values and RMA of the transfer functions relating λ_0 to θ_0, w, β_0, r, as well as λ_s to θ_c, v, β_c, q, (diagonal terms in $\boldsymbol{H}_\theta, \boldsymbol{H}_v, \boldsymbol{H}_\beta, \boldsymbol{H}_\Omega$) and to θ_s, u, β_s, p, (off-diagonal terms in $\boldsymbol{H}_\theta, \boldsymbol{H}_v, \boldsymbol{H}_\beta, \boldsymbol{H}_\Omega$) for the single rotor configuration. Note that, λ_c diagonal and off-diagonal transfer functions (the former involving $\theta_c, v, \beta_c, q,$, the latter involving θ_s, u, β_s, p) coincide with the λ_s ones.

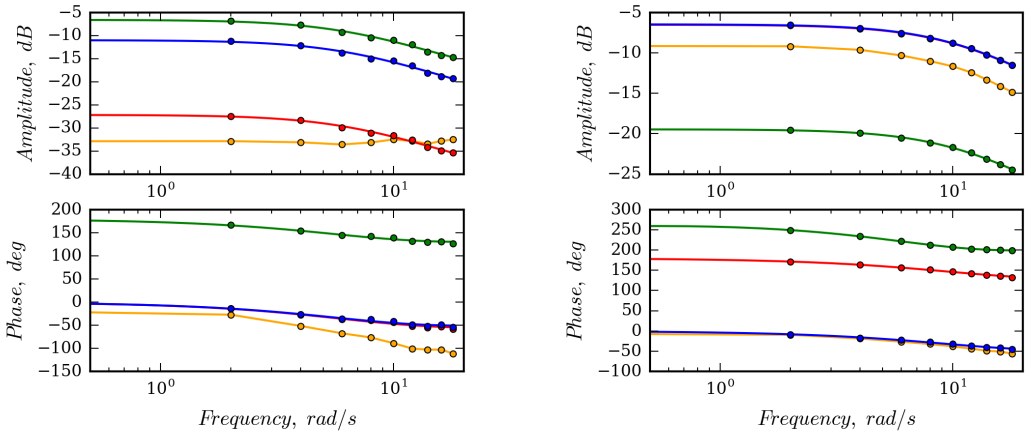

(a) λ_0 vs θ_0, w,β_0,r

(b) λ_s vs θ_s, u,β_c,p

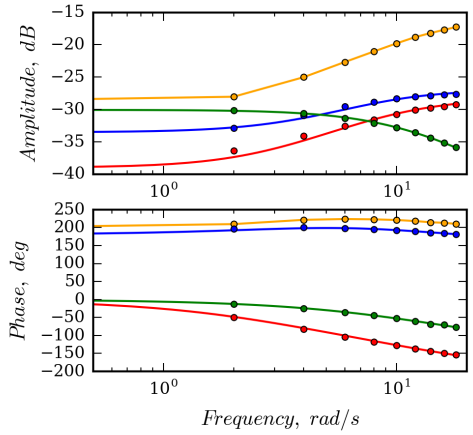

(c) λ_s vs θ_c, v,β_s,q

Figure 4.8: Transfer functions between velocity kinematic variables and inflow coefficients. Hovering condition. —— RMA, ● sample.

It is interesting to note that different perturbations yield to different transfer functions. Furthermore, figs 4.9 presents the comparison of the transfer functions in $\boldsymbol{H}_\theta$ evaluated by using an helicoidal prescribed wake, with those evaluated by the prescribed Landgrebe wake model based on experimental measurements [43] $\boldsymbol{H}_\theta^L$, and those determined through free-wake simulations (i.e., with wake shape deformed according to the local velocity field), $\boldsymbol{H}_\theta^F$. The differences between $\boldsymbol{H}_\theta$, $\boldsymbol{H}_\theta^L$ and $\boldsymbol{H}_\theta^F$ predictions confirm that the wake shape plays an important role in the aerodynamic simulation: free-wake

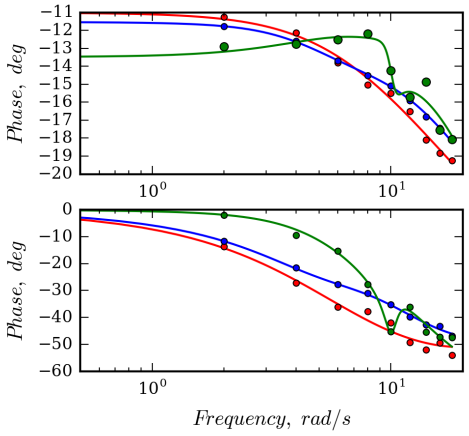

(a) λ_0 vs θ_0

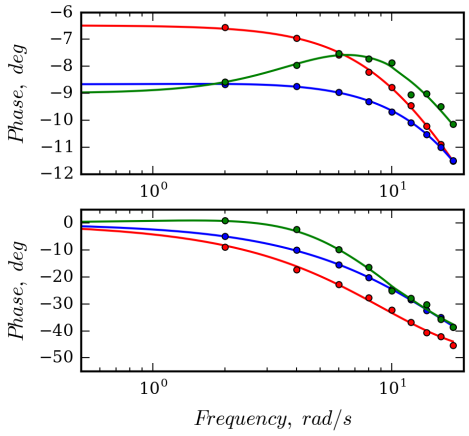

(b) λ_s vs θ_s.

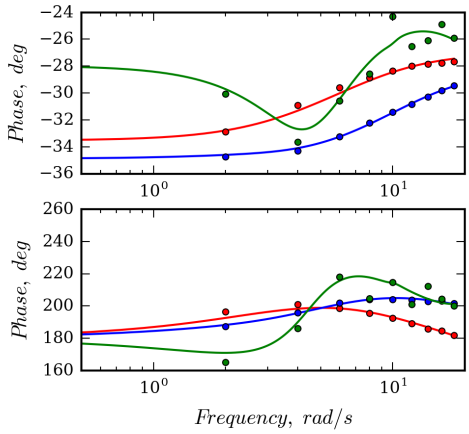

(c) λ_s vs θ_c.

Figure 4.9: Transfer functions between blade pitch controls and inflow coefficients. $\mathbf{H}_\theta$, $\mathbf{H}_\theta^L$, $\mathbf{H}_\theta^F$. Hover.

results tend to be closer to those from Landgrebe wake model than to helicoidal wake ones, although this is not true over the whole frequency range examined.

All the presented RMAs are achieved by introducing a number of poles (thus providing additional aerodynamic states) in a range of 3-5 real poles. Figure 4.10 shows the power coherence parameter matrix of the relevant $\boldsymbol{H}_\theta$, $\boldsymbol{H}_\theta^L$ and $\boldsymbol{H}_\theta^F$ transfer functions. Normally the identification is considered well done when $\gamma_P(\omega_i) \geq 0.6$. The high value of the coherence, for almost all the frequencies under examination, of the diagonal and off-

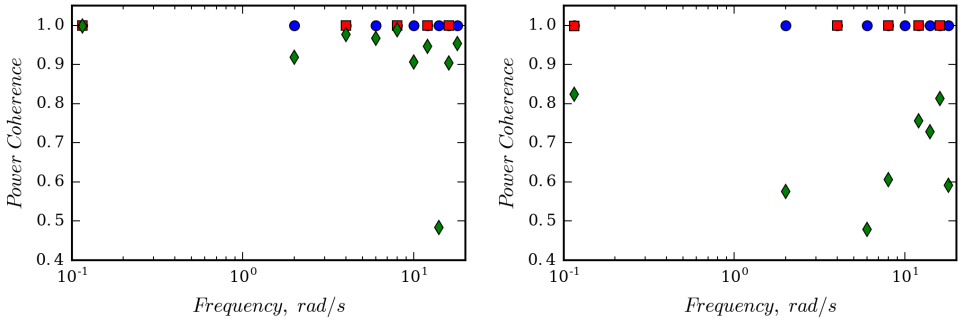

(a) $\lambda_0$vs θ_0 (b) $\lambda_s$vsθ_s

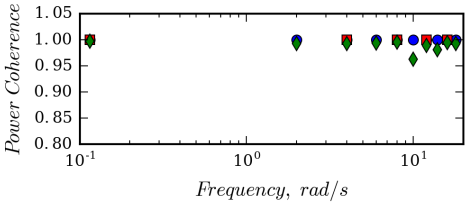

(c) $\lambda_s$vs θ_c

Figure 4.10: Power coherence of identification of transfer functions between blade pitch controls and inflow coefficients. ● $\mathbf{H}_\theta$, ■ $\mathbf{H}_\theta^L$, ♦ $\mathbf{H}_\theta^F$. Hover.

diagonal transfer functions previously presented, indicates that the transfer functions are very well estimated. Figure 4.11 shows a subset of the elements of the transfer functions matrices, $\boldsymbol{H}_\theta$ of the coaxial configuration, with the remaining ones that are either negligible or identical to those shown, for symmetry reasons. The components of wake inflow on the two rotors present remarkable differences: on the lower rotor, the transfer functions are generally of higher amplitude than upper rotor's ones (particularly those concerning blade pitch components, $\theta_0^+, \theta_c^+, \theta_s^+$), and present faster increase of angular phase with increasing frequency. Similar considerations may be drawn for the transfer functions $\boldsymbol{H}_{V\Omega}$ shown in fig. 4.12. A partial exception is represented by the transfer function λ_s vs u in fig. 4.12(c), whose upper rotor amplitude, in the lower-frequency range, is significantly higher than lower rotor one. It is interesting to note the similarity between the transfer functions λ_s vs θ_s^+ and λ_s vs p (see figs. 4.11(f) and 4.12(p)), as well as that between λ_s vs θ_c^+ and λ_s vs q (see figs. 4.11(d) and 4.12(f)): these are consistent with the similarity between the blade kinematic effects (and consequent

distribution of released wake vorticity) produced by θ_s^+ and p perturbations and by θ_c^+ and q perturbations.

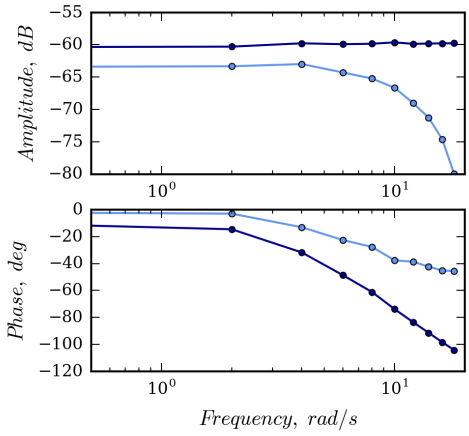

(a) $\lambda_0^{u,l}$ vs θ_0^-

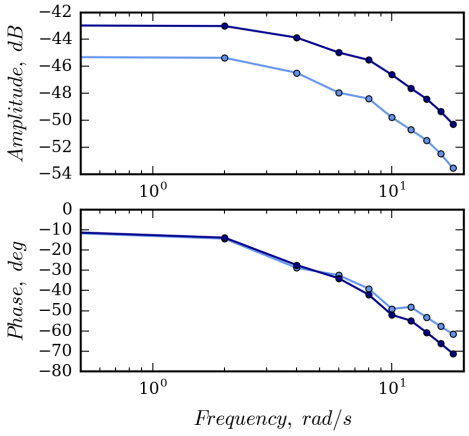

(b) $\lambda_0^{u,l}$ vs θ_0^+

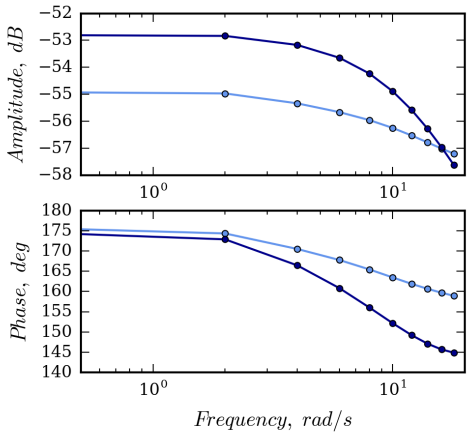

(c) $\lambda_s^{u,l}$ vs θ_c^-

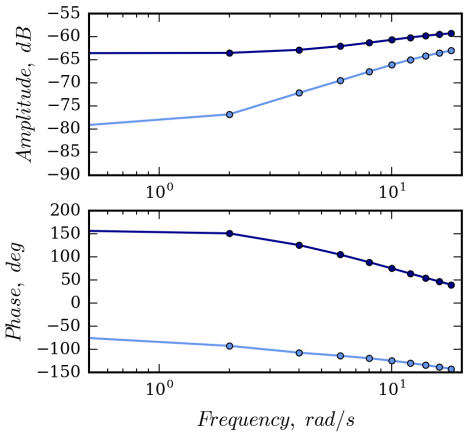

(d) $\lambda_s^{u,l}$ vs θ_c^+

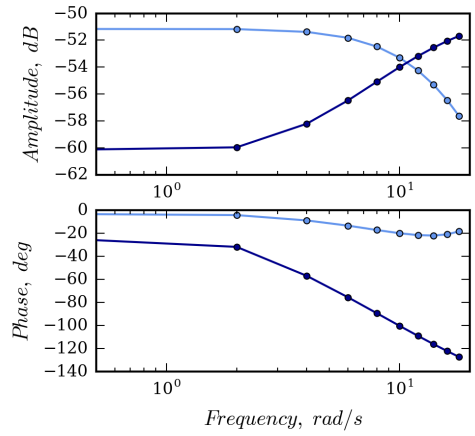

(e) $\lambda_s^{u,l}$ vs θ_s^-

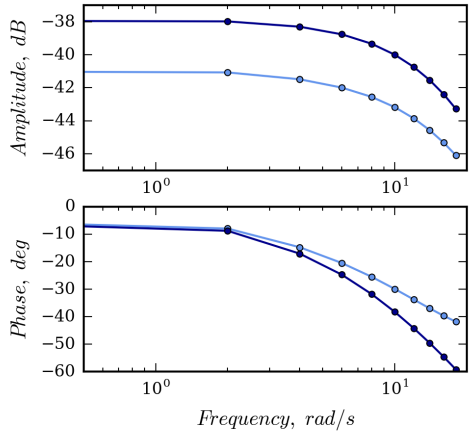

(f) $\lambda_s^{u,l}$ vs θ_s^+

Figure 4.11: Transfer functions between blade pitch control variables and wake inflow components. Hovering condition — RMA upper rotor — RMA lower rotor, ● samples.

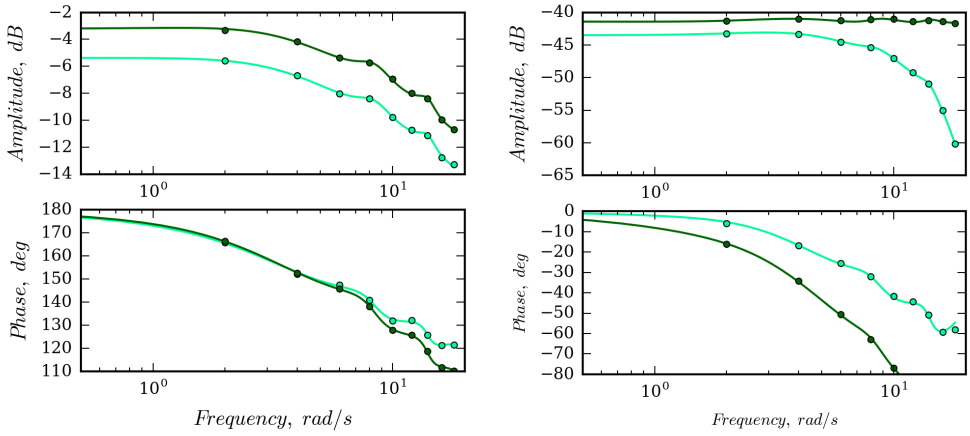

(a) $\lambda_0^{u,l}$ vs w

(b) $\lambda_0^{u,l}$ vs r

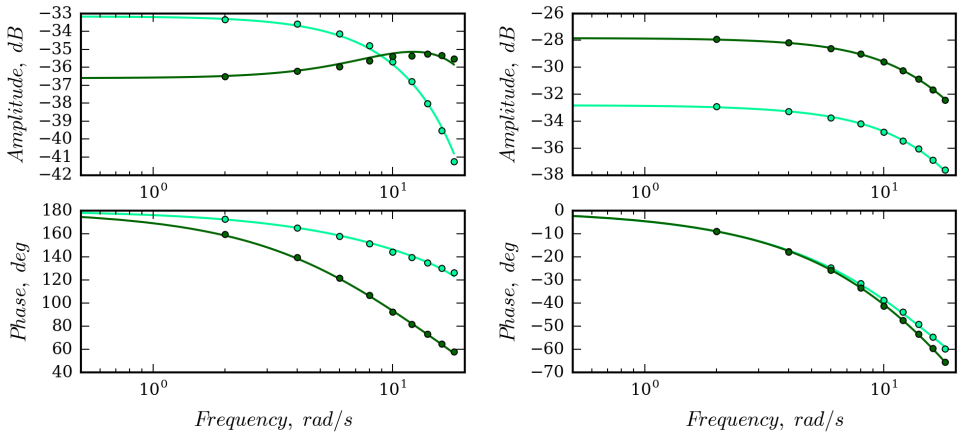

(c) $\lambda_s^{u,l}$ vs u

(d) $\lambda_s^{u,l}$ vs v

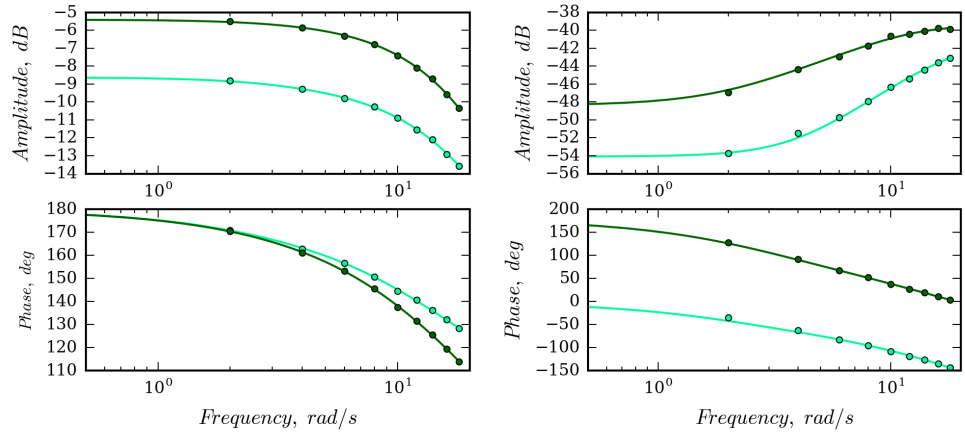

(e) $\lambda_s^{u,l}$ vs p

(f) $\lambda_s^{u,l}$ vs q

Figure 4.12: Transfer functions between hub kinematic variables and wake inflow components. Hovering condition — RMA upper rotor, — RMA lower rotor, ● samples.

A subset of the elements of the transfer functions matrix $\mathbf{H}_\theta^F$ is shown in fig. 4.13. Similarly to the prescribed wake case, the components of wake inflow on the two rotors present remarkable differences, but the amplitudes of the lower rotor transfer functions are no more generally higher than those of the upper rotor ones. In particular, the free wake analysis predicts in upper rotor λ_0^u vs θ_0^- and λ_s^u vs θ_c^+ amplitudes much increased with respect to those from the prescribed wake analysis, whereas the opposite effect is observed on the lower rotor ones. The rest of the depicted transfer functions are much less affected by the inclusion of the free wake effects. For all the showed transfer functions the RMAs reveal an excellent agreement with the sampled values. The presented RMAs are achieved by introducing a number of poles (thus providing additional aerodynamic states) in a range of 7-11 poles.

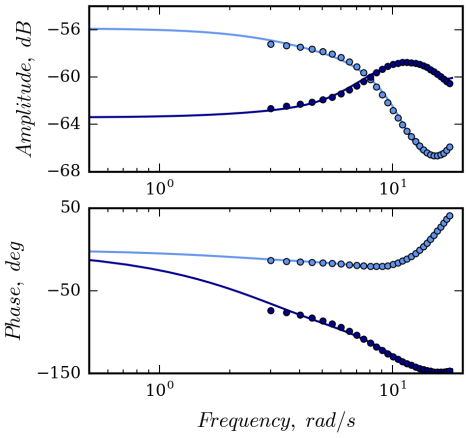

(a) $\lambda_0^{u,l}$ vs θ_0^-

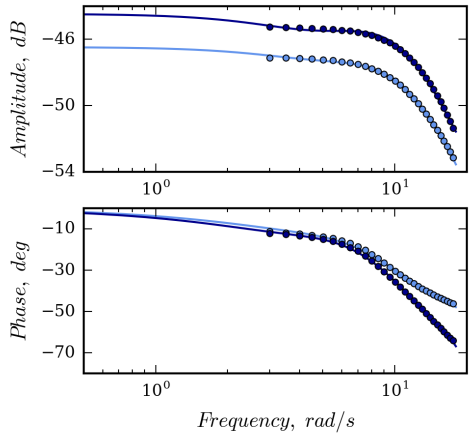

(b) $\lambda_0^{u,l}$ vs θ_0^+

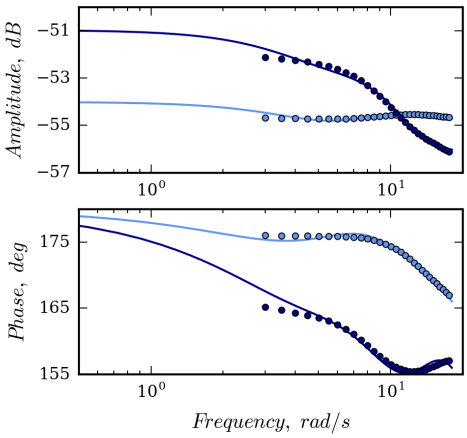

(c) $\lambda_s^{u,l}$ vs θ_c^-

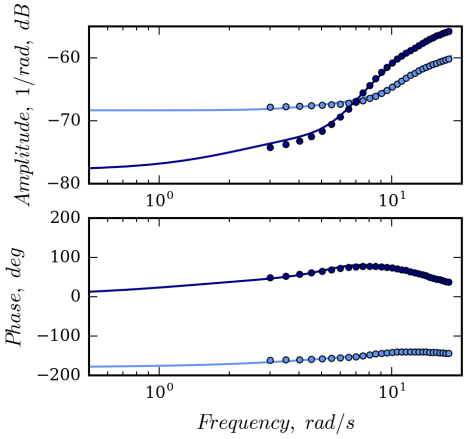

(d) $\lambda_s^{u,l}$ vs θ_c^+

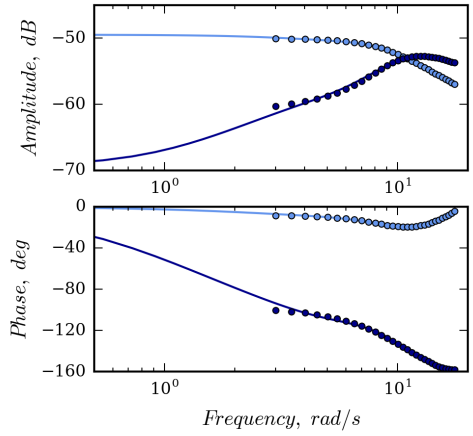

(e) $\lambda_s^{u,l}$ vs θ_s^-

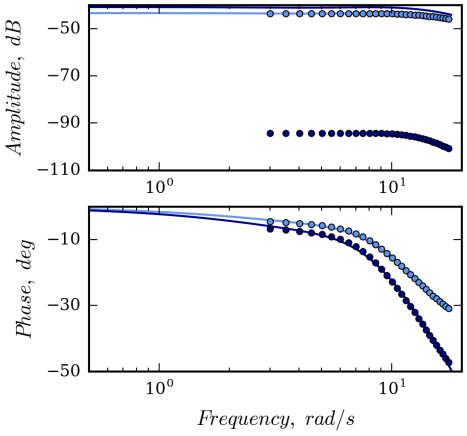

(f) $\lambda_s^{u,l}$ vs θ_s^+

Figure 4.13: Transfer functions between blade pitch control variables and wake inflow components, for hovering condition, free-wake analysis — RMA upper rotor — RMA lower rotor, ● samples.

Advancing rotor

When forward flight conditions are considered, the transfer function matrices are fully populated, due to aerodynamic couplings. Figures 4.14,4.15 and 4.16 depicts the elements of $\boldsymbol{H_\theta}$ for the single rotor configuration, where these coupling effects can be observed (see, for instance, fig. 4.14b(b) that represents the strong influence of θ_c on λ_0). Note that, in this case, the transfer functions are sampled almost up to $1/rev$ frequency, because of the presence of higher frequency poles, as shown in fig. 4.16(b). The presented RMAs are achieved by introducing a 3 additional aerodynamic states.

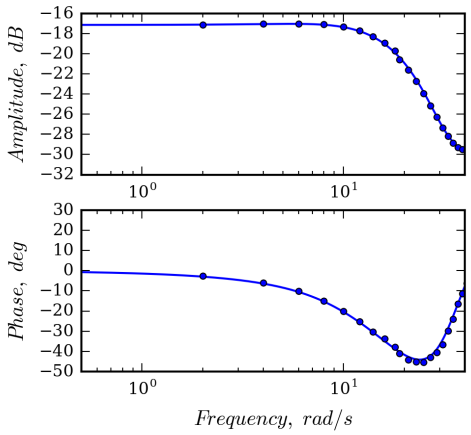

(a) λ_0 vs θ_0

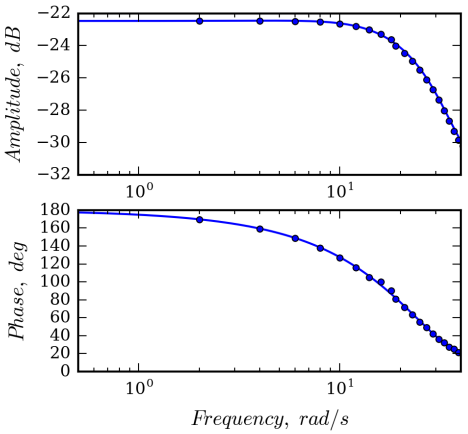

(b) $\lambda 0$ vs θ_c

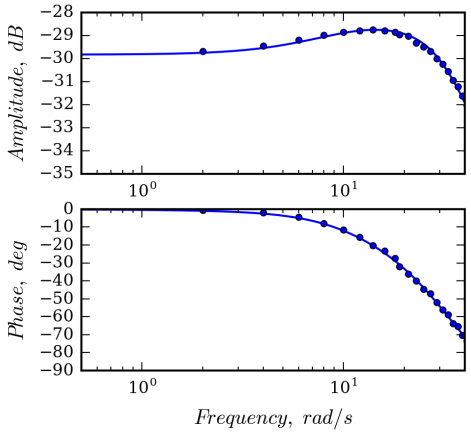

(c) λ_0 vs θ_s

Figure 4.14: Transfer functions between blade pitch controls and λ_0 . Forward flight

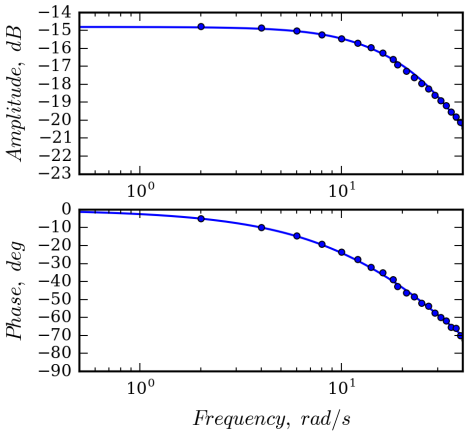

(a) λ_s vs θ_0

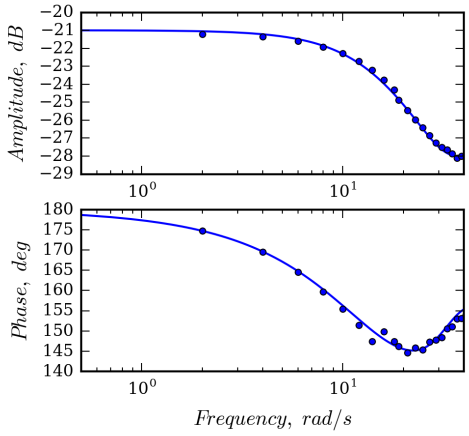

(b) λs vs θ_c

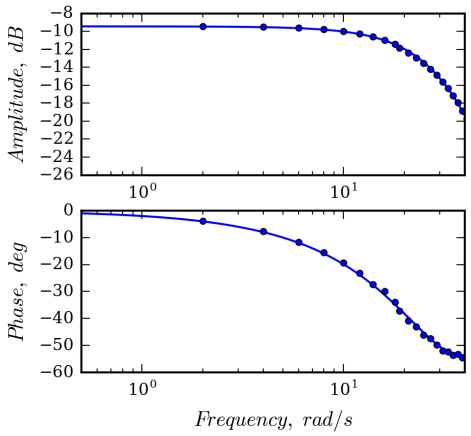

(c) λ_s vs θ_s

Figure 4.15: Transfer functions between blade pitch controls and λ_s . Forward flight

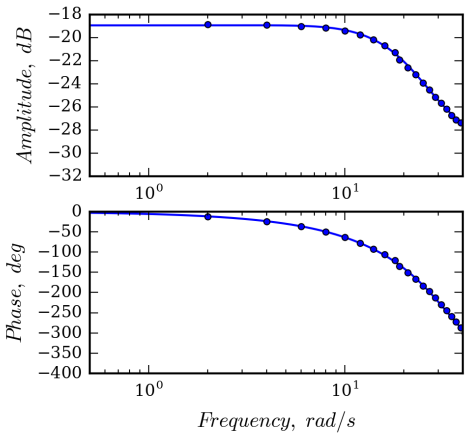

(a) λ_c vs θ_0

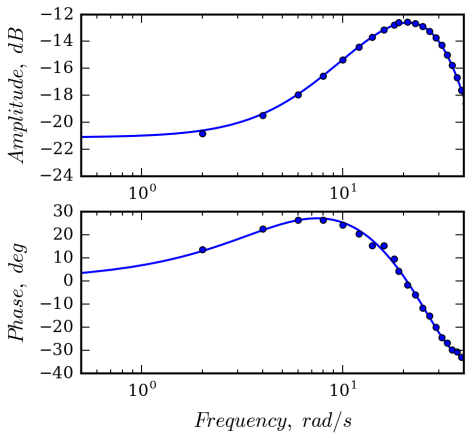

(b) λc vs θ_c

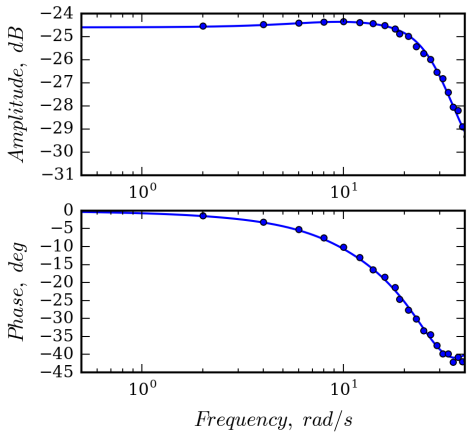

(c) λ_c vs θ_s

Figure 4.16: Transfer functions between blade pitch controls and λ_c . Forward flight

The power coherence of the signals examined in the identification process is depicted in fig. 4.17. In this case, although the wake geometry is assumed to be of prescribed shape and small-perturbation inputs are considered, the power coherence is always less than one because of the periodic nature of advancing-rotor aerodynamic operators (given by the combination of translation and rotation motion). These results provide a measure of the degree of inaccuracy of the proposed LTI model to represent wake inflow for forward flight configurations. However, it is interesting to observe that the power coherence is very close to one for the $\mathbf{H}_\theta$ diagonal transfer functions, while its lowest

values are met for the transfer functions involving either the input or the output cyclic-sine component (namely, θ_s or λ_s). It means that the latter variables are remarkably associated to the time-variant behavior of the advancing-rotor aerodynamic operator.

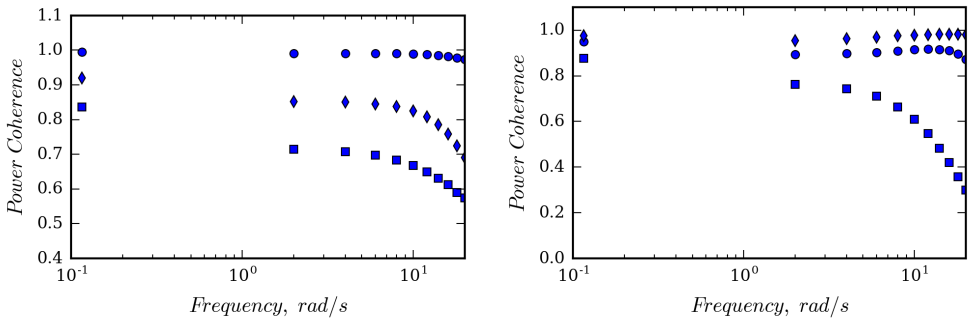

(a) θ_0

(b) θ_c

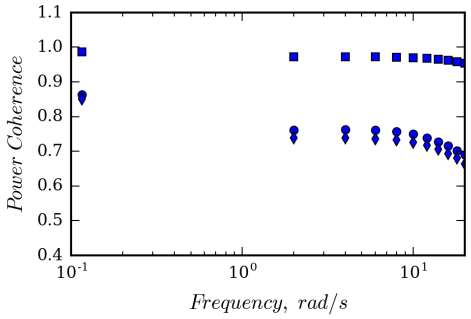

(c) θ_s

Figure 4.17: Power coherence of identification of transfer functions between blade pitch controls and inflow coefficients. ● λ_0, ♦ λ_s, ■ λ_c. Forward flight

Figure 4.18 shows the same subset of elements of the transfer functions matrix for the coaxial configuration, $\mathbf{H}_\theta$, selected for fig. 4.12. Comparing these two figures (both related to prescribed wake shape aerodynamic simulations), it can be readily observed that in forward flight conditions, differently from the hovering case, the magnitudes of the inflow transfer functions on upper and lower rotors are very close or identical (except for λ_s vs θ_s^- in fig. 4.18(e) and, at the higher frequencies, λ_s vs θ_c^+ in fig. 4.18(d)), and that they are either in phase (see figs. 4.18(b), 4.18(c) and 4.18(f)). In addition, the magnitude of the forward flight transfer functions is remarkably lower than that of

the hovering ones. Reduced cross coupling effects between cyclic variables may also be noted (see, for instance, λ_s vs θ_c^+ in figs. 4.12(f) and 4.18(d)). The physical reason of these differences between hovering and forward flight inflow responses is the position of the released wakes with respect to the two rotors. Indeed, the skewed prescribed wakes of the advancing rotors rapidly move away from the blades, with the upper one impinging just the 20% of the outer rear part of the lower rotor disc, and therefore, a lower inflow magnitude is expected, along with drastically reduced coupling between the two rotors. Similarly to the results for the hovering case, the RMA of transfer functions of matrix $\mathbf{H}_\theta$ appears in excellent agreement with sampled values. The presented RMA is achieved by introducing 11 poles.

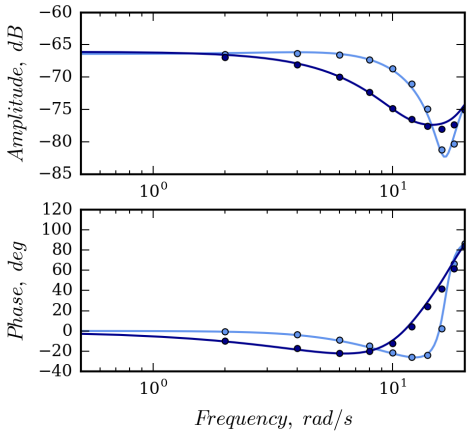

(a) $\lambda_0^{u,l}$ vs θ_0^-

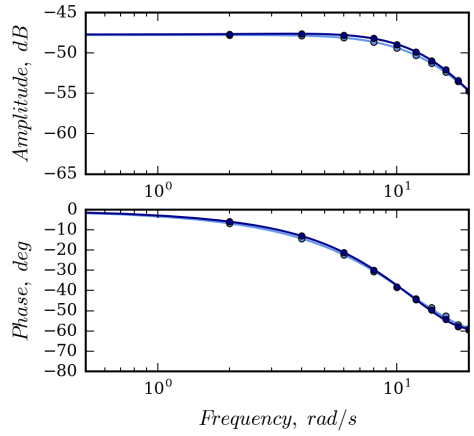

(b) $\lambda_0^{u,l}$ vs θ_0^+

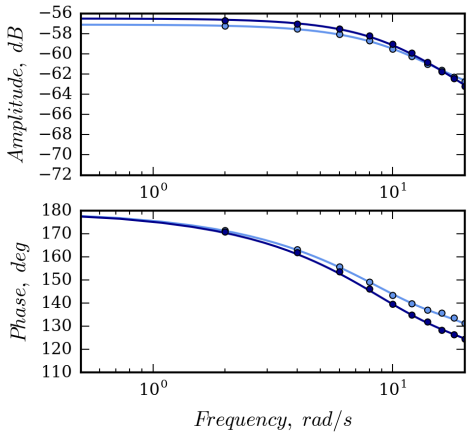

(c) $\lambda_s^{u,l}$ vs θ_c^-

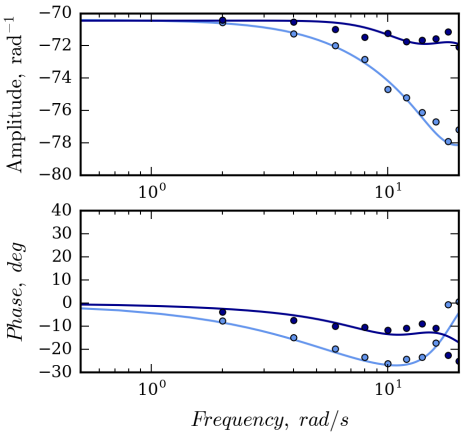

(d) $\lambda_s^{u,l}$ vs θ_c^+

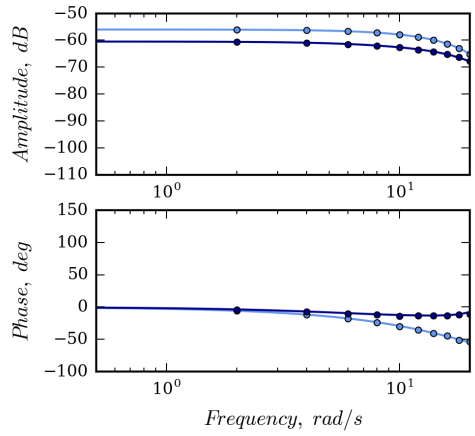

(e) $\lambda_s^{u,l}$ vs θ_s^-

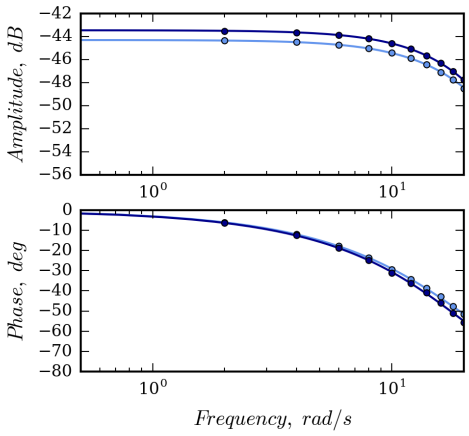

(f) $\lambda_s^{u,l}$ vs θ_s^+

Figure 4.18: Transfer functions between blade pitch control variables and wake inflow components, forward flight condition, — RMA upper rotor — RMA lower rotor, ● samples.

V-f model

Next, the load based wake inflow model identified is presented. As already attested in the previous chapter, this model is evaluated considering the Pitt-Peters like inflow distribution.

Hovering rotor

In order to evaluate the transfer function relating the wake inflow coefficient and the rotor hub loads, the transfer function relating kinematics perturbation and loads must be evaluated. By way of example fig. 4.19 shows the sampled transfer function $\mathbf{G}_\theta$ and its coherence parameter, for the single rotor configuration and free wake solution. Differently from the identification of the wake inflow transfer function, all the coherence parameter are extremely high. This is also observed for the coaxial configuration and in forward flight condition. Figure 4.20 shows the transfer functions between the mean inflow component and the thrust coefficient appearing in $\hat{\mathbf{H}}_\theta, \hat{\mathbf{H}}_V$, $\hat{\mathbf{H}}_\theta$ and $\hat{\mathbf{H}}_\beta$, along with that given by the Pitt-Peters model.

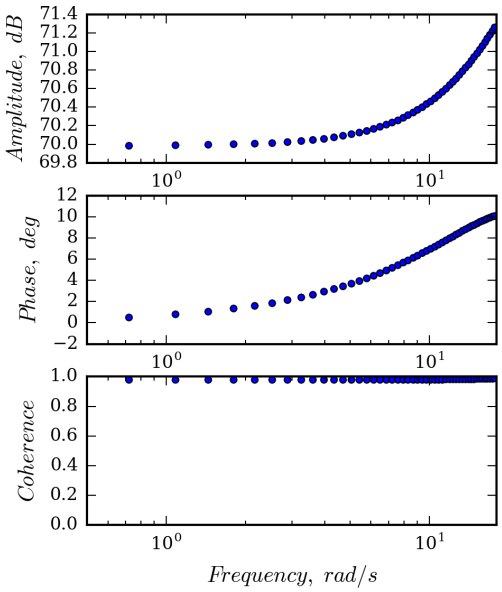

(a) C_T vs θ_0

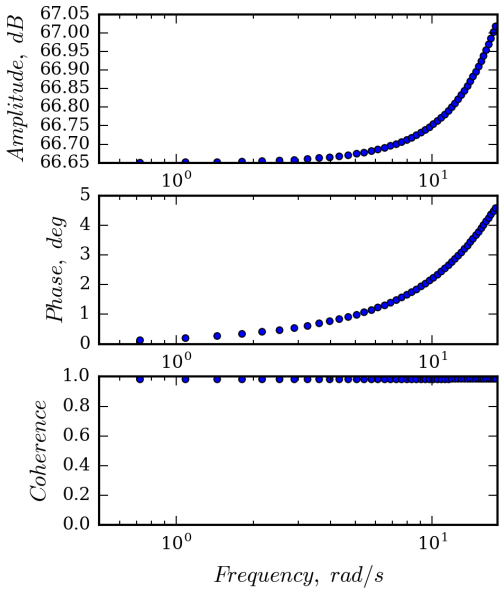

(b) C_L vs θ_c

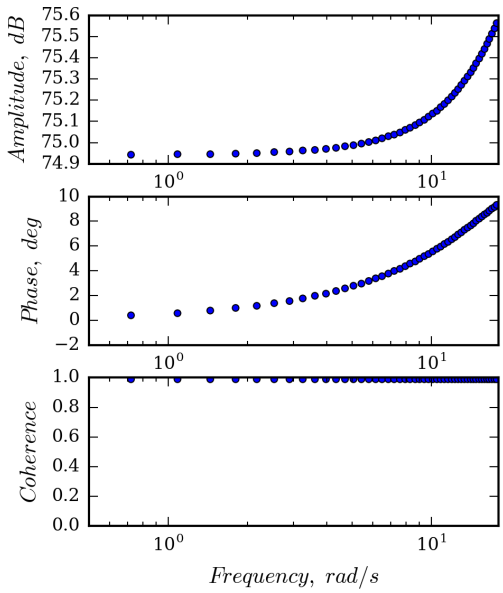

(c) C_L vs θ_s

Figure 4.19: Transfer functions between blade pitch control variables and rotor hub loads, hovering condition. Single rotor configuration. Free wake analysis.

First of all, it is interesting to observe that the transfer functions determined by the

proposed approach are significantly dependent on the kinematic perturbation they are derived from. For instance, λ_0 vs C_T derived from linear velocity and angular velocity perturbations present amplitude discrepancies of about 6 dB, and phase discrepancies of $7° - 8°$.

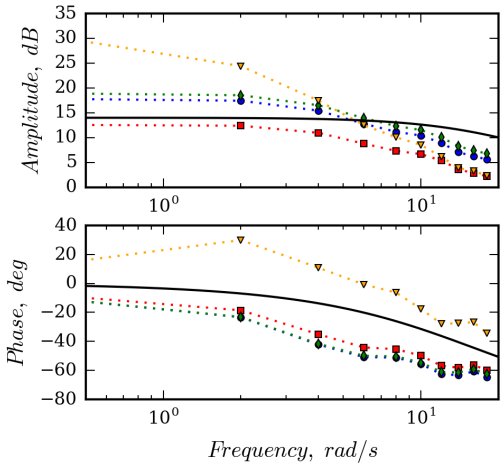

Figure 4.20: Transfer function λ_0 vs C_T : load based approach $\hat{\mathbf{H}}_\theta$, $\hat{\mathbf{H}}_V$,$\hat{\mathbf{H}}_\beta$,$\hat{\mathbf{H}}_\Omega$ compared with Pitt-Peters'one ——

Therefore, even in hovering condition, λ_0 cannot be considered simply dependent on the thrust coefficient: inflow depends on wake vorticity and hence on the spanwise bound vorticity distribution (strictly related to the lift distribution) which, in turn, is heavily affected by the downwash distribution and hence by the generating kinematic perturbation. For instance, the same value of thrust coefficient perturbation may be suitably obtained either by collective pitch perturbation that provides uniform geometric angle of attack radial distribution, or by axial velocity perturbation producing arctangent-shape radial distribution of the geometric angle of attack. This confirms the dependency of Pitt-Peters-type inflow modelling on blade circulation distribution already observed in [44, 12], at the same time providing an interpretation of its kinematic origin. Then, comparing the identified transfer functions with those from the original Pitt-Peters model it is apparent that different modeling procedures (namely, based on q_θ, q_V, q_Ω and q_β perturbations) provide correlations of different quality, while the decay of all of the present models amplitudes with increasing frequency is faster. In addition,

the present transfer functions show similar phases, with a discrepancy of 10° - 20° with respect to the Pitt-Peters model. Figure 4.21(a) shows the transfer functions between wake inflow side-to-side gradient, λ_s, and in-plane rolling moment, C_L .

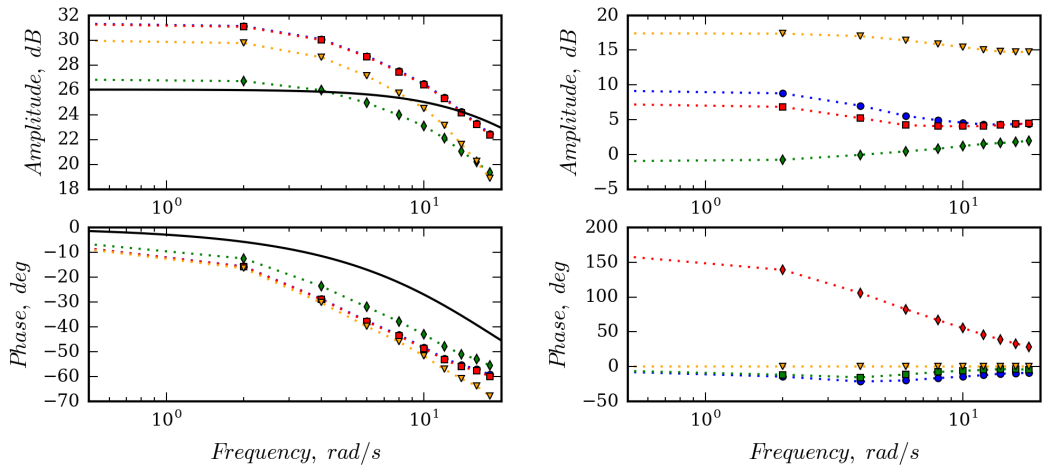

(a) λ_s vs C_L (b) λ_s vs C_M

Figure 4.21: Transfer functions evaluated by load based approach $\hat{\mathbf{H}}_\theta$, $\hat{\mathbf{H}}_V$, $\hat{\mathbf{H}}_\beta$, $\hat{\mathbf{H}}_\Omega$, and comparison with Pitt-Peters model

Due to the axial symmetry of hovering flight condition, this transfer function is coincident with the one relating fore-to-aft gradient to pitching moment. Although to a lower extent, also these transfer functions depend on the specific perturbation variable they are derived from. However, almost identical transfer functions are extracted from in-plane angular velocities, p, q, and cyclic controls, θ_s, θ_c perturbations, since their effect on blade downwash is substantially the same (namely, a constant perturbation of the geometric angle of attack along the blade span). If compared to the results in fig. 4.20, the transfer functions from $\hat{\mathbf{H}}_V$, $\hat{\mathbf{H}}_\Omega$ and $\hat{\mathbf{H}}_\theta$ have closer phases, while maintaining a phase lag of about 10° with respect to the Pitt-Peters model. The frequency behavior of the transfer functions in figs. 4.20 and 4.21(a) is confirmed by the placement of the corresponding stable poles presented in Table 4.2 (with the RMA ones related to the matrix $\hat{\mathbf{H}}_\theta$): indeed, those determined by the present approach are represented by real values lower than those of Pitt-Peters' model, thus inducing the lower-frequency response amplitude decay and the larger phase delay observed in figs. 4.20 and 4.21(a).

Note that, the poles associated with λ_s , λ_c transfer functions have algebraic multiplicity equal to two. Next, the off-diagonal transfer function between λ_s and pitching moment,

	RMA $\hat{\mathbf{H}}_\theta$	RMA $\hat{\mathbf{H}}_\theta^F$	Pitt-Peters model
λ_0 transfer function	4.1 rad/s	6.43 rad/s	10.46 rad/s
λ_s, λ_c transfer functions	4.84 rad/s	6.84 rad/s	19.61 rad/s
	8.43 rad/s	11.34 rad/s	

Table 4.2: Wake inflow models poles. Hover.

C_M , is shown in fig. 4.21(b) (for symmetry reasons, an almost identical transfer function is obtained between λ_c and rolling moment, C_L). Consistently with Pitt-Peters' model (which considers null such a transfer function), its amplitude is significantly smaller than that of λ_s vs C_L and λ_c vs C_M . In the overall, the λ_s vs C_M transfer functions derived from q_Ω and q_θ perturbations are very similar, whereas different values of this transfer function are obtained by q_V perturbations. Also for the hovering rotor case, the effect of the wake shape on the Pitt-Peters like modeling is examined in fig. 4.22. It shows the sampled transfer functions λ_0 vs C_T, λ_s vs C_L and λ_s vs C_M (with the corresponding RMAs) as resulting from q_θ perturbations and aerodynamic responses evaluated considering helicoidal prescribed wake, Landgrebe-model prescribed wake , and free-wake simulation. Confirming the observations made on figs. 4.9(a), 4.9(b) and 4.9(c), different wake shapes generate quite different transfer functions, with free-wake solutions introducing higher frequency poles. For the specific case considered, they are positioned around 10 rad/s, in a range of frequency which is of interest for both flight dynamics and aeroelasticity simulations.

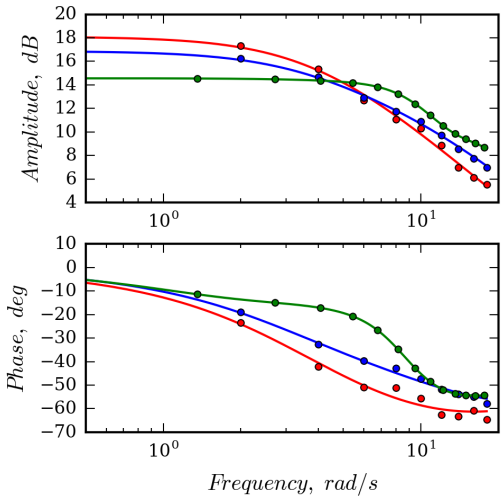

(a) C_T vs θ_0

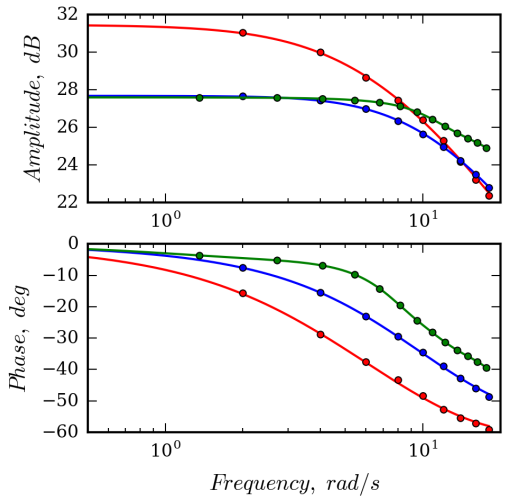

(b) C_L vs θ_c

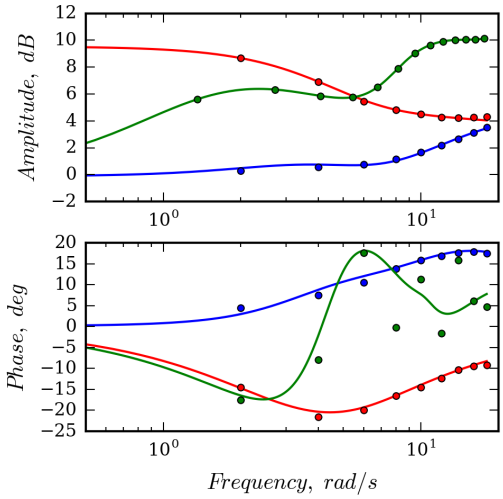

(c) C_L vs θ_c

Figure 4.22: Wake shape effect on identified Pitt-Peters-like transfer functions. $\hat{\mathbf{H}}_\theta$, $\hat{\mathbf{H}}_\theta^L$, $\hat{\mathbf{H}}_\theta^F$

Finally the relevant transfer function of the $\lambda - f$ model obtained from all the kinematic perturbation and by utilizing the free wake algorithm are shown in fig. 4.23.

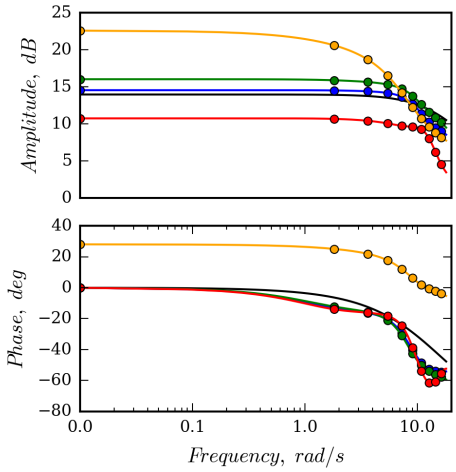

(a) λ_s vs C_L

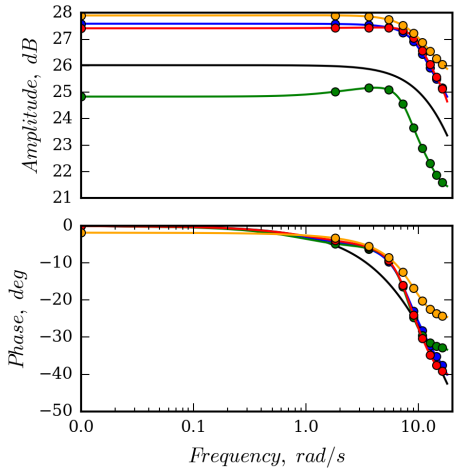

(b) λ_s vs C_L

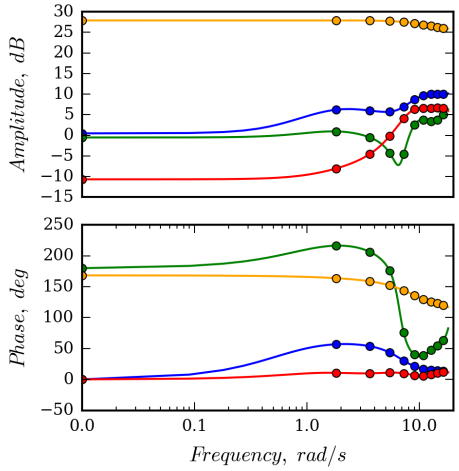

(c) λ_s vs C_M

Figure 4.23: Transfer functions evaluated by load based approach $\hat{\mathbf{H}}_\theta$, $\hat{\mathbf{H}}_V$, $\hat{\mathbf{H}}_\beta$, $\hat{\mathbf{H}}_\Omega$, and comparison with Pitt-Peters model

Clearly the transfer functions of the load based inflow model are still dependent on the perturbation they are derived from and similarly conclusion between the prescribed wake and free wake solution may be drawn for all the other kinematic perturbations. All the presented RMAs are achieved by introducing a number of poles in a range of 3-5.

Figure 4.24 shows sampled values and RMA of the most significant transfer functions in $\hat{\mathbf{H}}_{\Omega V}$ and $\hat{\mathbf{H}}_{\theta}$ of the coaxial configuration, without presenting, for the sake of conciseness, those non-negligible transfer functions that are easily derivable by observing that λ_s vs C_L and C_M are fully equivalent (in hovering) to λ_c vs C_M and C_L. In this case, 13 states are introduced in order to achieve the RMAs. In line with the results observed in figs. 4.12 and 4.11, inflow on lower rotor is generally higher than that on upper rotor. In addition, it can be observed that: (i) the mutual influence between the two rotors is remarkable; (ii) the influence of upper rotor loads on lower rotor inflow is higher than the influence of lower rotor loads on upper rotor inflow; (iii) RMAs are of excellent quality for all the transfer functions examined and as for the single rotor case, the Pitt-Peters type inflow model derived from q_{θ} perturbations and that obtained from $q_{\Omega V}$ show noticeable discrepancies. It is interesting to note that, for the examined coaxial rotor, the higher-amplitude transfer functions in $\hat{\mathbf{H}}_{\theta}$ and $\hat{\mathbf{H}}_{\Omega V}$ (namely, $\lambda_0^{u,l}$ vs $C_T^{u,l}$, $\lambda_s^{u,l}$ vs $C_L^{u,l}$ and hence $\lambda_c^{u,l}$ vs $C_M^{u,l}$, see figs. 4.24(a), 4.24(b), 4.24(c) and 4.24(d)) are in much higher agreement than the corresponding ones evaluated for the single rotor case. Different perturbations provide quite different transfer functions when considering cross-coupling effects (like, for instance, $\lambda_s^{u,l}$ vs $C_M^{u,l}$, see figs. 4.24(e) and 4.24(f)). This closer similarity between $\hat{\mathbf{H}}_{\theta}$ and $\hat{\mathbf{H}}_{\Omega V}$ is probably the beneficial effect of deriving the Pitt-Peters type model from a larger set of inputs (six instead of three, as for single rotors) which is representative of a larger domain of perturbed load distributions. Therefore, in order to obtain a Pitt-Peters type model that is almost univocally related to the rotor operative conditions and corresponding circulation distributions, these results suggest to attempt the reformulation of the problem in terms of a larger number of input loads.

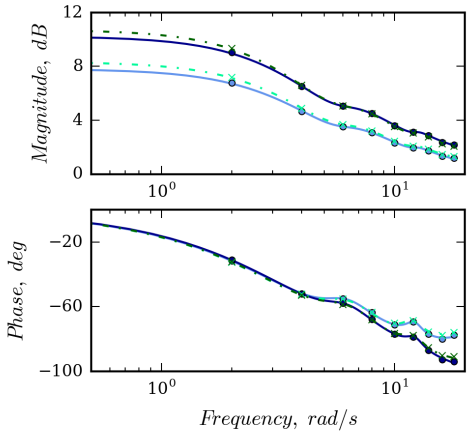

(a) $\lambda_0^{u,l}$ vs C_T^u

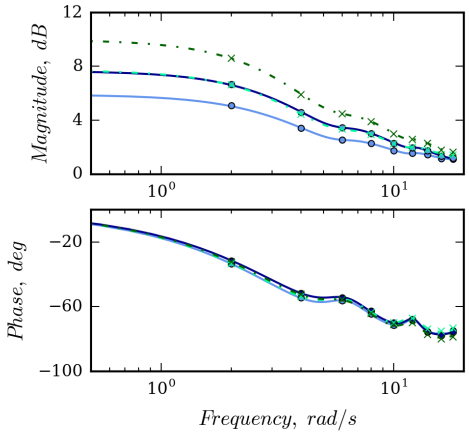

(b) $\lambda_0^{u,l}$ vs C_T^l

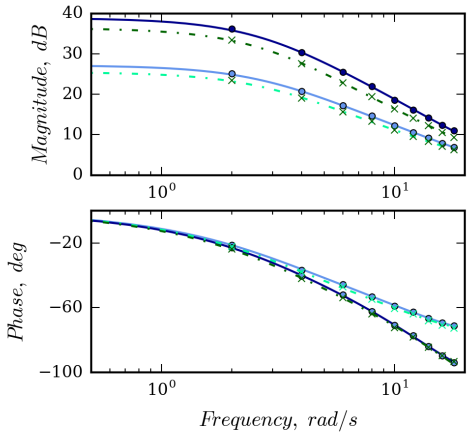

(c) $\lambda_s^{u,l}$ vs C_M^u

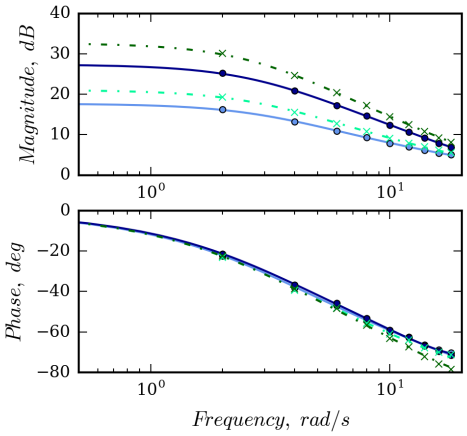

(d) $\lambda_s^{u,l}$ vs C_M^l

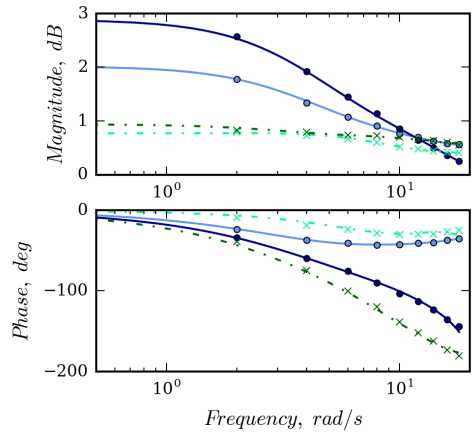

(e) $\lambda_s^{u,l}$ vs C_M^u

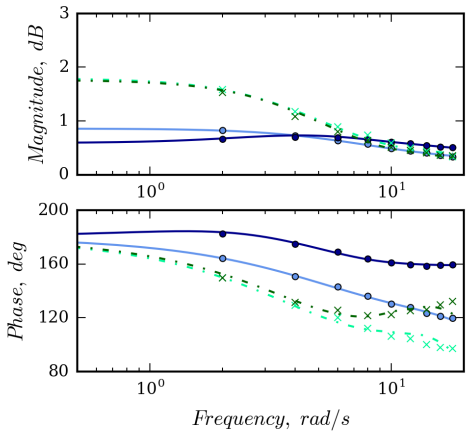

(f) $\lambda_s^{u,l}$ vs C_M^l

Figure 4.24: Transfer functions evaluated by load based approach, hovering condition., RMA upper rotor RMA lower rotor, ● samples.

Advancing rotor

Figures 4.25, 4.26 and 4.27 present the elements of the matrix $\hat{\mathbf{H}}_\theta$ compared with the non-zero Pitt-Peters' transfer functions, for the single rotor configuration in forward flight condition. In this case, 3 aerodynamic states are introduced in order to achieve the RMA.

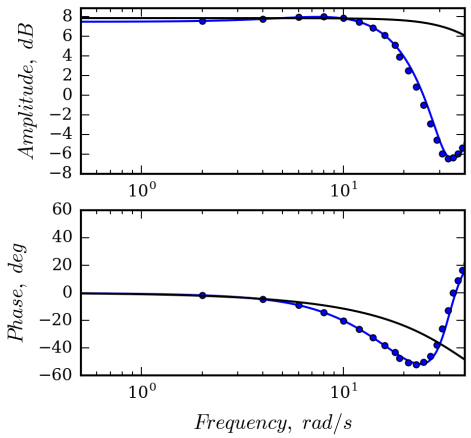

(a) λ_0 vs C_T

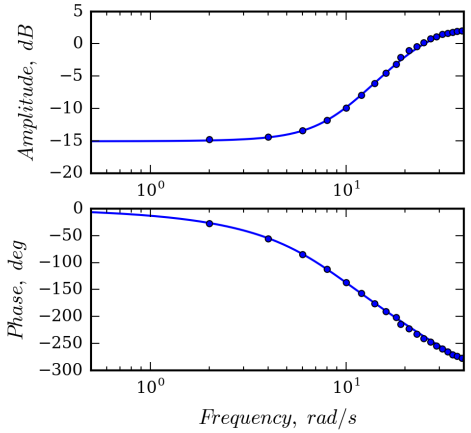

(b) λ_0 vs C_L

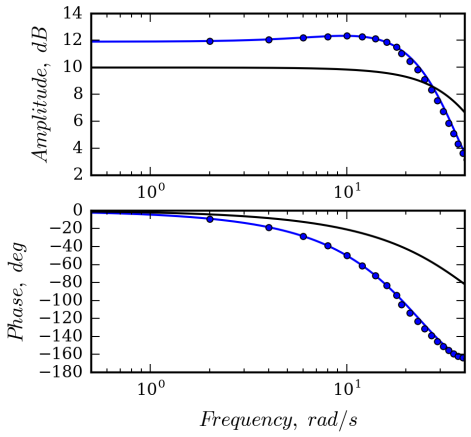

(c) λ_0 vs C_M

Figure 4.25: Transfer functions between rotor loads and λ_0 and comparison with Pitt-Peters model. Forward flight condition. —— RMA , ● samples.

The range of frequency considered (up to $1/rev$) allows to notice the presence of high frequency poles, which significantly affect dynamic inflow response above 15 rad/s.

The transfer functions from the proposed approach appear to be closer to Pitt-Peters' ones than in the hovering rotor case. This is true especially in the low frequency range, with some remarkable exceptions (see, for instance, fig. 4.25(a)). It is worth noting that, increasing the frequency of perturbation, unsteady effects different from those considered by the momentum theory become relevant and, as a consequence, high frequency poles arise in the transfer functions.

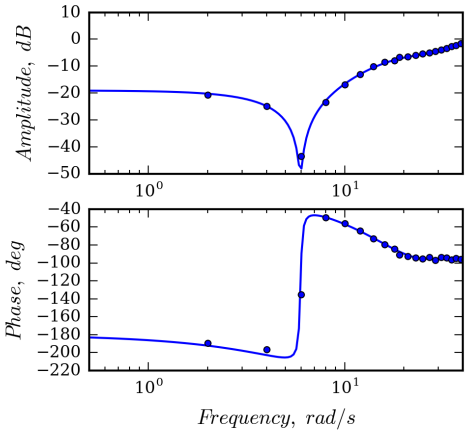

(a) λ_s vs C_T

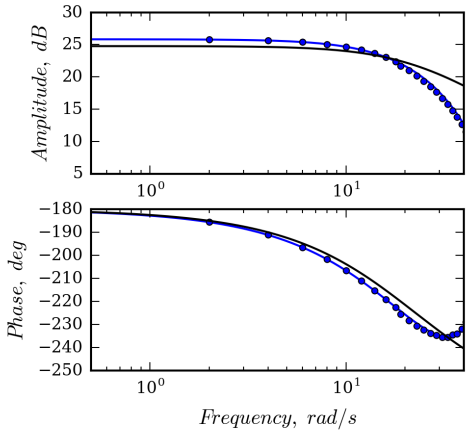

(b) λ_s vs C_L

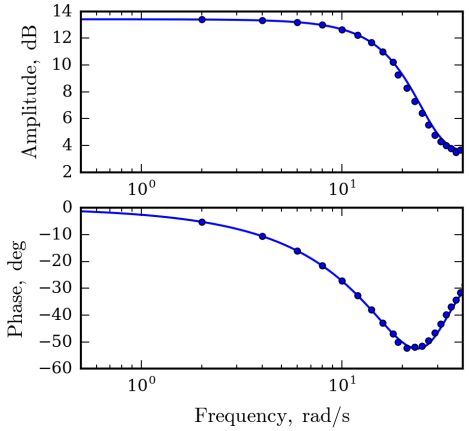

(c) λ_s vs C_M

Figure 4.26: Transfer functions between rotor loads and λ_s and comparison with Pitt-Peters model. Forward flight condition. —— RMA , ● samples.

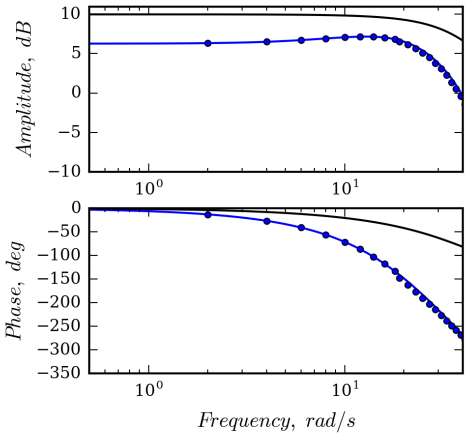

(a) λ_c vs C_T

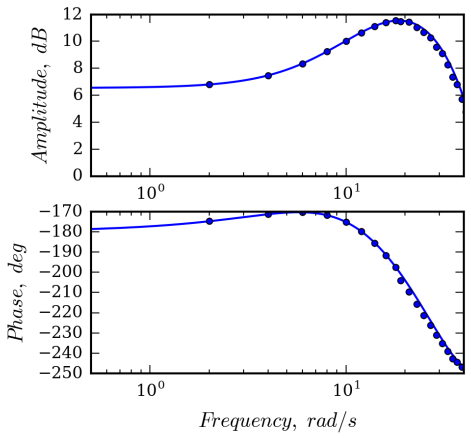

(b) λ_c vs C_L

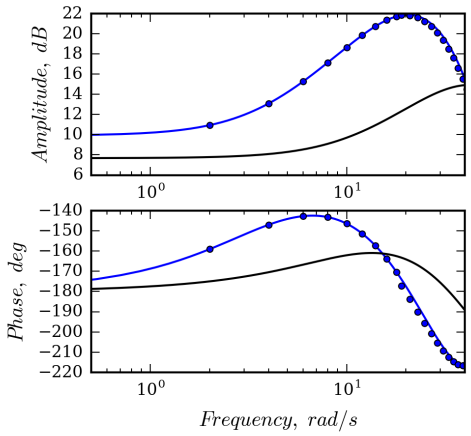

(c) λ_c vs C_M

Figure 4.27: Transfer functions between rotor loads and λ_c and comparison with Pitt-Peters model. Forward flight condition. —— RMA , ● samples.

Next, Fig. 4.28 shows the most relevant transfer functions of the Pitt-Peters type model derived from blade pitch perturbations of the coaxial configuration. It is interesting to observe that, differently from what occurring in hovering condition where lower rotor inflow perturbations are higher than upper rotor ones independently on the perturbed load rotor (see fig. 4.24), in this case lower coupling occurs between upper and lower rotors: indeed, upper/lower rotor load perturbations produce higher upper/lower rotor inflow components perturbations.

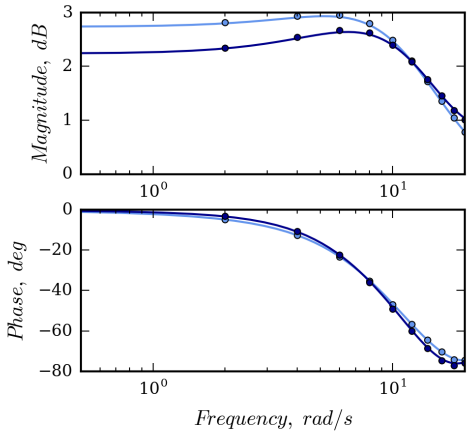

(a) $\lambda_0^{u,l}$ vs C_T^u

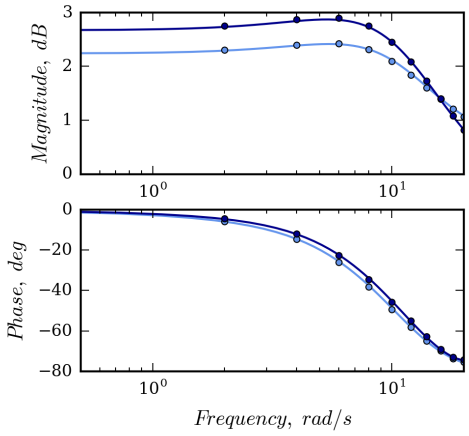

(b) $\lambda_0^{u,l}$ vs C_T^l

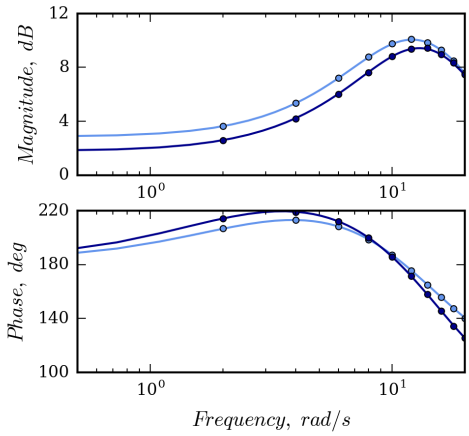

(c) $\lambda_c^{u,l}$ vs C_M^u

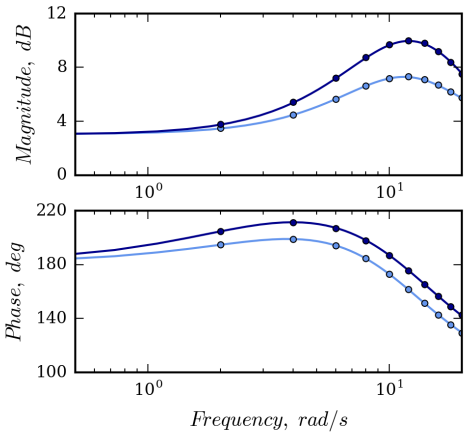

(d) $\lambda_c^{u,l}$ vs C_M^l

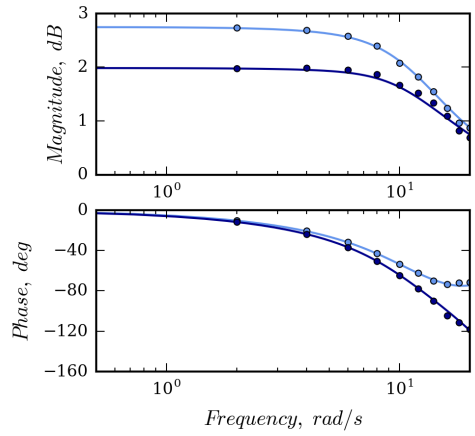

(e) $\lambda_s^{u,l}$ vs C_M^u

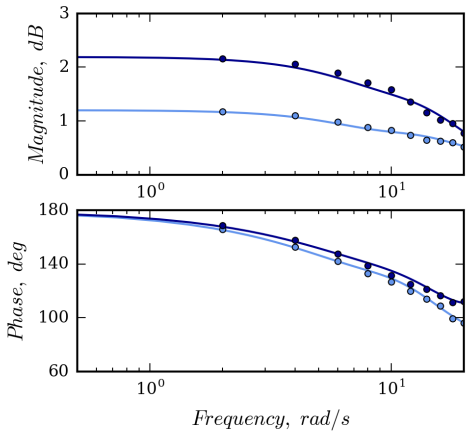

(f) $\lambda_s^{u,l}$ vs C_M^l

Figure 4.28: Transfer functions between rotor loads and inflow coefficients. Forward flight condition. RMA upper rotor RMA lower rotor, ● samples.

Furthermore, as compared to the hovering case results, it is confirmed that C_M strongly affects λ_c , whereas it has a weak effect on λ_s (the opposite occurs for C_L). Likewise the hovering rotor case, the RMA is of excellent accuracy, thus assuring the definition of accurate finite-state wake inflow modeling.
Unlike the kinematic based model, for the $\lambda - f$ model is not possible to establish a wellness indicator such the coherence. This is because the coherence parameter represent a relation between the output and the input directly applied to the system. However, it is believed the quality of the $\lambda - f$ transfer functions depends on the wellness of the sampled transfer function relating the inflow and forces to the kinematic inputs, respectively $\mathbf{H}_q$ and $\mathbf{G}_q$. Moreover, in the next section is presented a time validation of the inflow models that represent the litmus test.

4.2.1 Time marching validation for kinematic and load based models

Before employ the identified inflow models, and in general after any kind of system identification problem, it is a good practice to test the resulting state space. Even if the coherence parameter represent one of the confirmed criterion for the identification wellness, it is recommended to perform the goodness of the identification in order to check the output quality. Therefore in order to assess the capability of the presented finite-state models to predict the wake inflow generated by arbitrary perturbations of the kinematic variables, its outcomes are compared with those given by the non-linear, time-marching aerodynamic BEM solver.

Hovering

Considering, without loss of generality, the following chirp type arbitrary perturbation of roll angular velocity (expressed in deg/s)

$$p(t) = sin[\omega(t)t]e^{\alpha t} \tag{4.1}$$

where $\omega(t) = \gamma t$ with $\gamma = 3\ rad/s^2$ and $\alpha = -0.25\ rad/s$, for the single rotor configuration fig. 4.29(a) depicts the corresponding evolutions inflow components, λ_c and λ_s, as predicted by the BEM solver and by the $\lambda - q$ finite-state model.

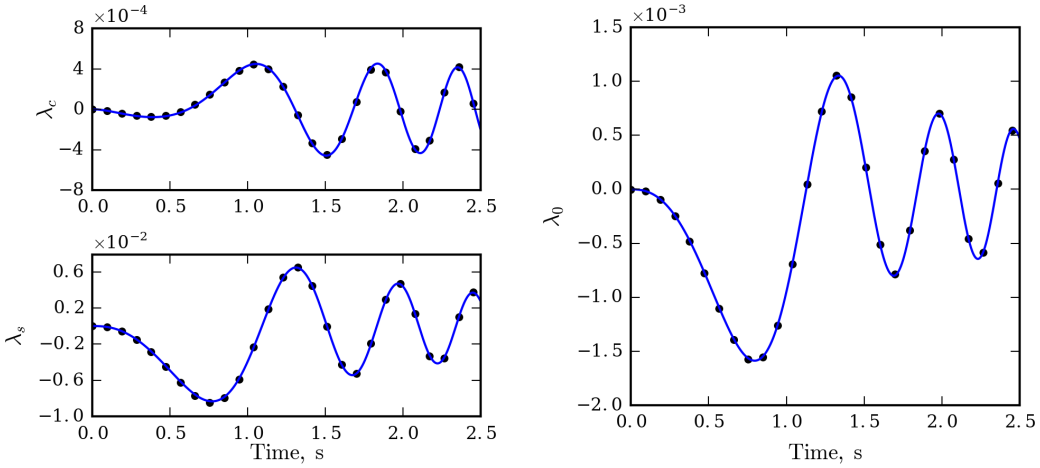

(a) p perturbation

(b) w perturbation

Figure 4.29: Time response to perturbations. Hovering condition. Correlation among BEM simulations and predictions given by the $\lambda - q$ state-space model. ● BEM; — state-space model.

The validation of λ_0 predictions in fig. 4.29(b) is accomplished by considering small w perturbations following the same time evolution given in eq. 4.1 (in this case, expressed in m/s). As expected, the finite-state $\lambda - q$ model is in excellent agreement with the BEM predictions.

In order to test the capabilities of the $\lambda - f$ models, the rotor loads deriving from the kinematic perturbations, are used as inputs to the load based model identified. In particular fig. 4.30 compares the BEM prediction and finite-state model predictions of inflow coefficients corresponding to the same kinematic perturbations of fig. 4.29. The results are shown for three different LTI finite-state models, namely those obtained by $\hat{\mathbf{H}}_\theta$, $\hat{\mathbf{H}}_\Omega$ and $\hat{\mathbf{H}}_V$. As expected, in case of roll angular velocity perturbation fig. 4.30(a), the finite-state model derived by $\hat{\mathbf{H}}_\Omega$ is in excellent agreement with the BEM predictions. The same is true when the finite-state model derived by $\hat{\mathbf{H}}_V$ is employed to predict the inflow coefficient in case of w perturbation 4.30(b). Instead, when the finitestate model is based on variables different from those perturbing the rotor, the analytic solution differs from the BEM one, consistently with the results shown in figs. 4.21(a) and 4.21(b). In particular, the results obtained by the finite state model based

on $\hat{\mathbf{H}}_V$ present a remarkable discrepancy in terms of the λ_c phase.

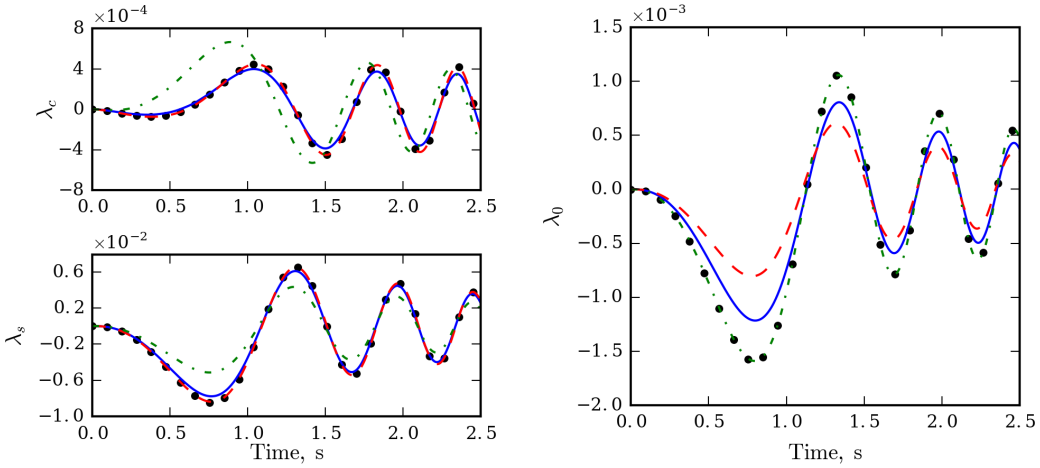

(a) p perturbation

(b) w perturbation

Figure 4.30: Time response to perturbations. Hovering condition. Correlation among BEM simulations and predictions given by the $\lambda - f$ state-space models. ● BEM; — $\hat{\mathbf{H}}_\theta$; - · - · - $\hat{\mathbf{H}}_V$; - - - $\hat{\mathbf{H}}_\Omega$

Next considering a θ_c^+ perturbation, applied to the coaxial configuration, following the same time evolution in Eq. 4.1 (in this case, expressed in *deg*). Figure 4.31 depicts the corresponding rotor inflow components $\lambda_c^{u,l}$ and $\lambda_s^{u,l}$, as predicted by the BEM solver and by the kinematic finite-state model.

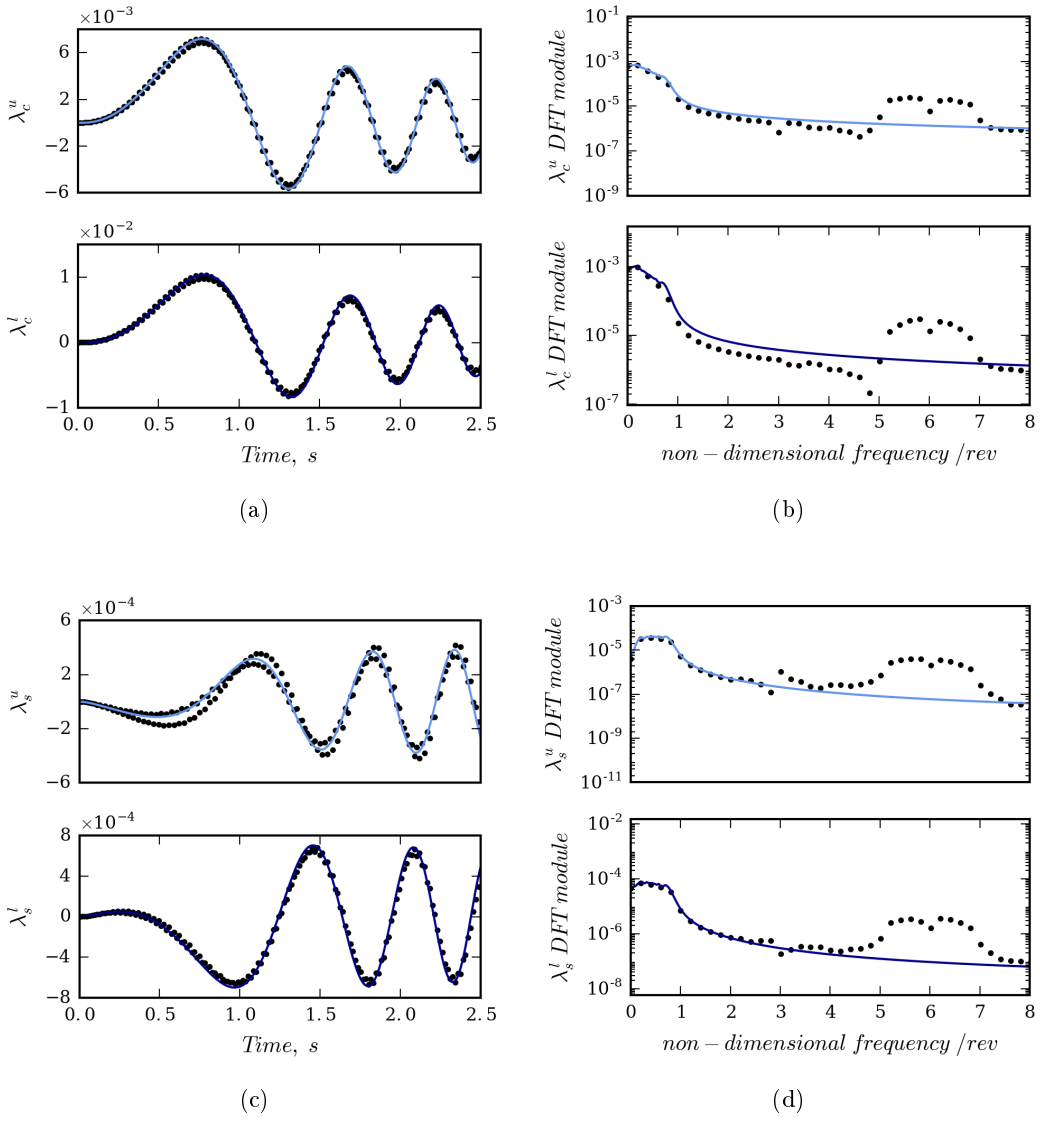

Figure 4.31: Time response and correlation of spectra response to θ_c^+ perturbation. Hovering condition. Correlation among BEM simulations and predictions given by the $\lambda - q$ state-space model. ● BEM; upper rotor lower rotor state space model

This finite-state model provides time responses that are in almost perfect agreement with nonlinear BEM solutions for any inflow components, except for multi-harmonic components around the $6/rev$, which are generated as part of the interactions between upper and lower rotors (see also fig. 4.3) and are fully missing in the analytical model (which is of LTI type).

Next, the inflow responses determined through the loaded based models of the coaxial configuration are examined. Figures 4.32 depict upper and lower rotor inflow components $\lambda_c^{u,l}$ and $\lambda_s^{u,l}$, as predicted by BEM and by finite-state models obtained from both $\hat{\mathbf{H}}_\theta$ and $\hat{\mathbf{H}}_{\Omega V}$.

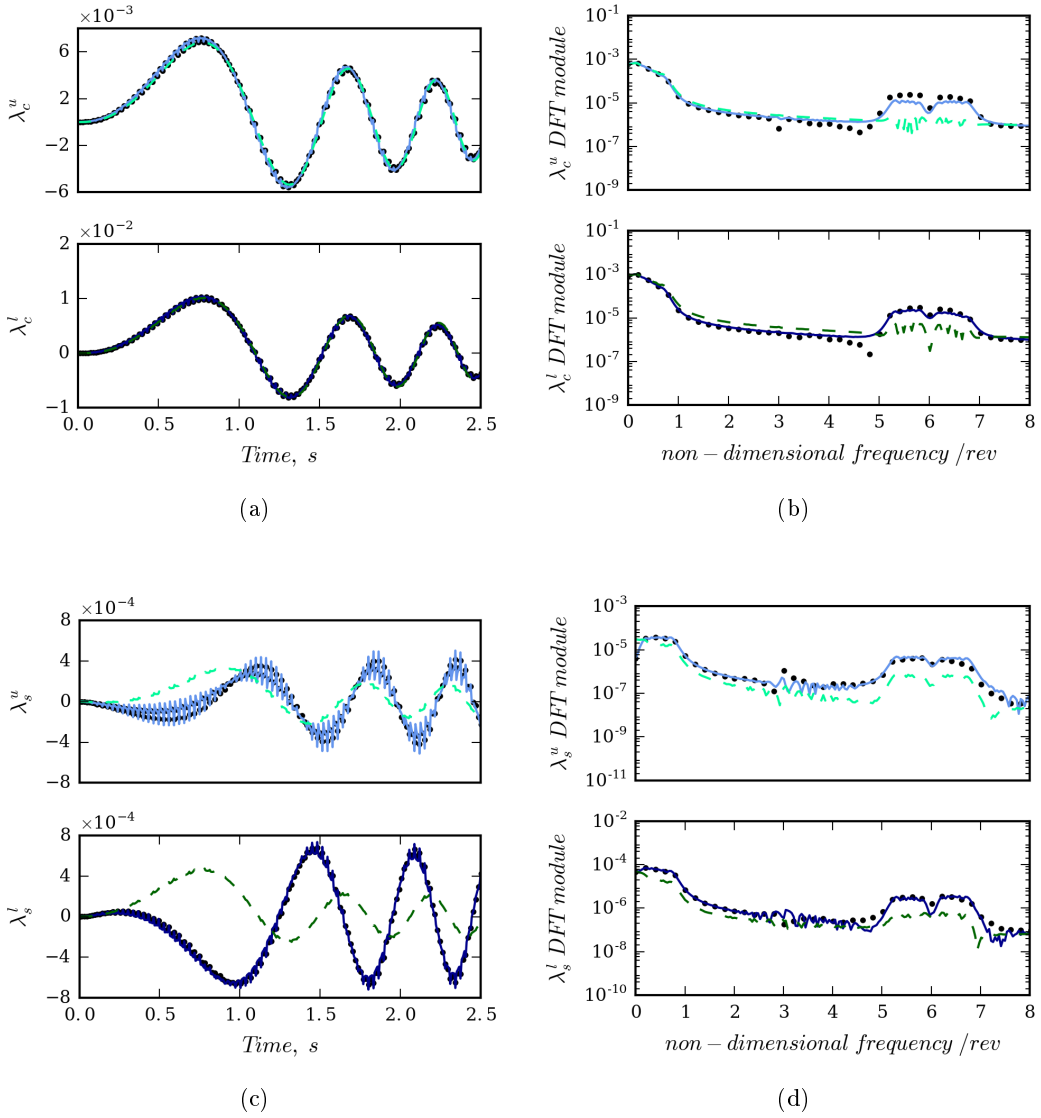

Figure 4.32: Time response and correlation of spectra response to θ_c^+ perturbation. Hovering condition. Correlation among BEM simulations and predictions given by the $\lambda - f$ state-space models. ● BEM; ——— upper rotor ——— lower rotor $\hat{\mathbf{H}}_\theta$; - - - upper rotor - - - lower rotor $\hat{\mathbf{H}}_{\Omega_V}$

As expected from the accuracy of the RMAs presented above, the predictions given by the finite-state model based on $\hat{\mathbf{H}}_\theta$ are in excellent agreement with the BEM simulations on the two rotors, for both $\lambda_c^{u,l}$ and $\lambda_s^{u,l}$, with inclusion of the small-amplitude, multi-harmonic components around the $6/rev$. Instead, when a loaded based model is identified through variables different from those perturbing the rotor, coherently with the results shown in fig. 4.24, the analytic solutions are not always in agreement with BEM's ones. Indeed, fig. 4.32(a) shows that the Pitt-Peters type model based on $\hat{\mathbf{H}}_{\Omega V}$ is capable of capturing with very good accuracy $\lambda_c^{u,l}$ responses on, whereas the simulation of $\lambda_s^{u,l}$ responses in fig 4.32(b) is of poor accuracy. Coherently with the observations of the $\lambda - q$ predictions, the analysis of the other wake inflow coefficients combined with the application of different inputs demonstrates that higher-amplitude inflow coefficients responses are predicted with similar good accuracy by both Pitt-Peters like models considered, whereas the quality of the prediction of terms of secondary importance (namely, cross-coupling terms) reveals a strong dependence on the kind of perturbation the analytical model is derived from. It is worth observing that, the presence of the higher-harmonic inflow component in the predictions by the Pitt-Peters type models is not given by the capability of the corresponding differential operator to provide multi-harmonic outputs (it is of LTI type, as well), but rather comes from the frequency content of the input loads directly derived from the BEM solver.

Also the perturbed inflow prediction capability of the state-space models of the coaxial configuration, based on free-wake high fidelity simulations is assessed. In this case, the input consists of the following blade cyclic perturbation (expressed in deg)

$$\theta_c^+(t) = [sin(0.4\Omega t) - sin(0.2\Omega t)]/2 \tag{4.2}$$

Figure 4.33 depicts the corresponding upper and lower rotor inflow components $\lambda_c^{u,l}$ as predicted by the BEM solver and by the kinematic finite-state model. The finite-state model predictions are in very good agreement with nonlinear BEM solution, except for missed small-magnitude, higher-harmonic components. These high-frequency discrepancies are similar, but a bit larger than those observed for the prescribed wake analysis in fig. 4.31. This is expected in the free-wake simulation, where higher-frequency components may arise also as wake distortion effects. Details of the discrepancies are given in fig. 4.34, which presents the comparison of the spectra of BEM and state-space model

responses, with the vertical lines indicating the harmonics of the perturbation signal, namely $0.2/rev$ and $0.4/rev$.

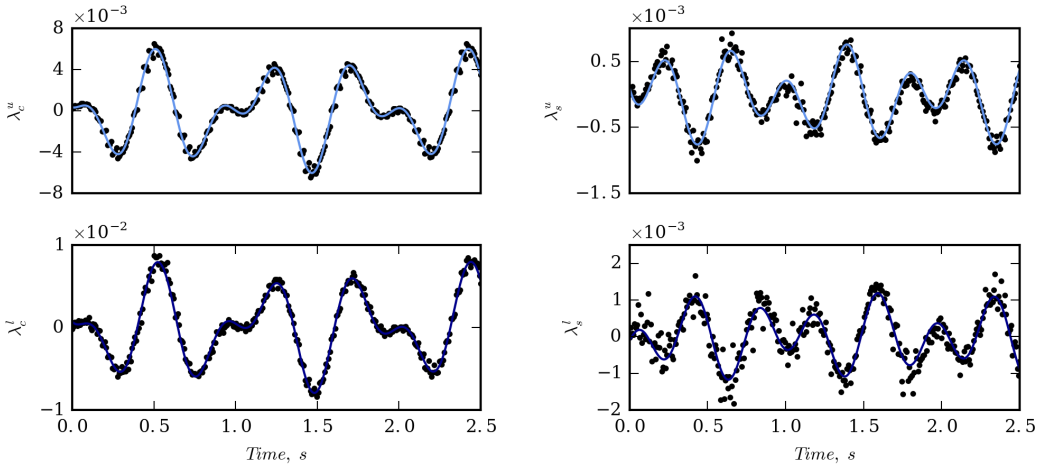

(a) (b)

Figure 4.33: Time response to θ_c^+ perturbation. Hovering condition, free wake analysis. Correlation among BEM simulations and predictions given by the $\lambda - q$ state-space model. ● BEM; ── upper rotor ── lower rotor state space model

It demonstrates that the proposed model perfectly captures the high-magnitude responses at the input frequencies (LTI component of the aerodynamic operator) whereas, as expected, it is unable to predict the high-frequency content resulting from the combination of the input frequencies with the $6/rev$ intrinsic periodicity due to upper and lower rotor interaction (LTP component of the aerodynamic operator), which generates the discrepancies appearing in Fig. 4.33.

The λ_c^u response given by the $\lambda - f$ state-space model derived from $\hat{\mathbf{H}}_\theta$ is presented in fig. 4.35, along with that provided by the BEM solver. Akin to the prescribed wake analysis, in addition to the low-frequency inflow components which are in very good agreement with the time-marching, non linear simulation, this state-space model, although of LTI type, provides high-frequency components due to the presence in the spectra of loads inputs directly given by the BEM tools.

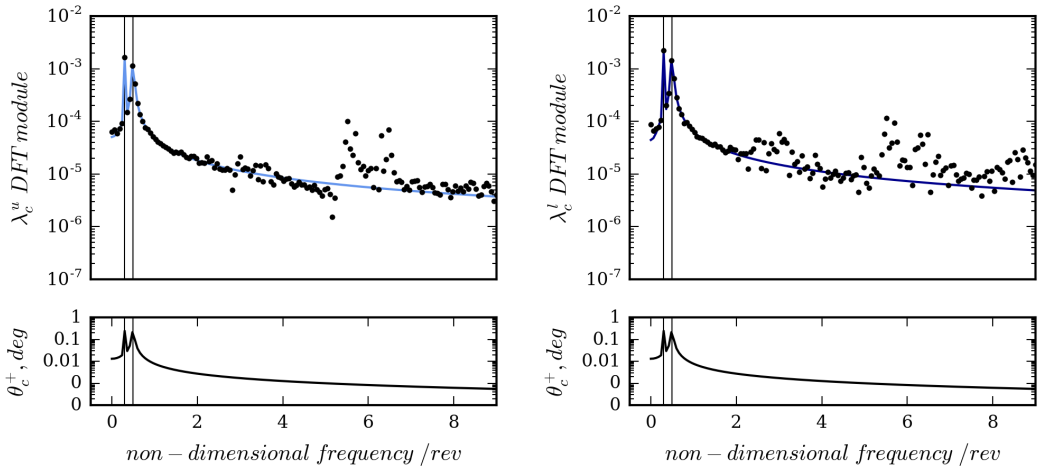

(a) (b)

Figure 4.34: Correlation of spectra response to θ_c^+ perturbation. Hovering condition. Correlation among BEM simulations and predictions given by the $\lambda - q$ state-space model. ● BEM; ——— upper rotor ——— lower rotor state space model. Vertical lines indicate the $0.2/rev$ and $0.4/rev$ harmonics of Eq. 4.2

However, as confirmed by the comparison of the spectra of BEM and state-space model responses in Fig. 4.35(b,c), these seem to be slightly overestimated, particularly the 6 ± 0.2 $/rev$ and the 6 ± 0.4 $/rev$ ones deriving from the combination of coaxial system aerodynamics intrinsic periodicity and input harmonics.

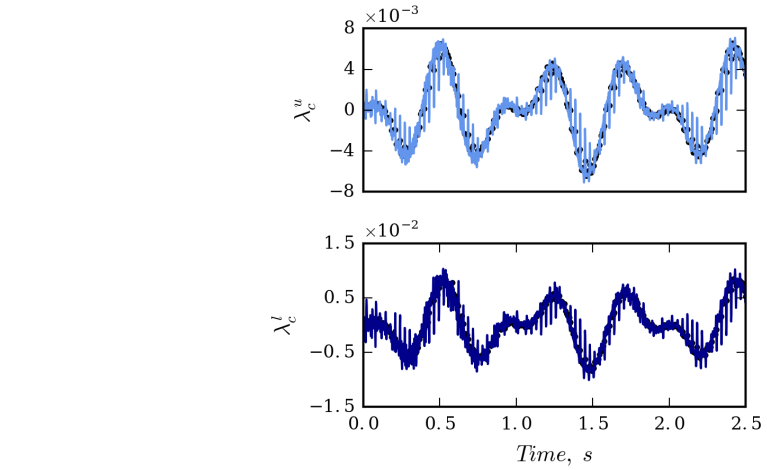

(a)

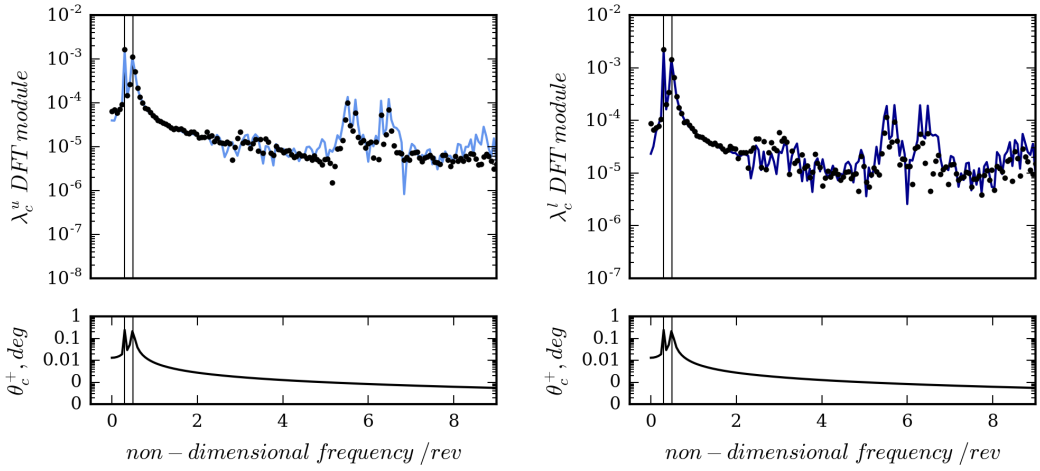

(b) (c)

Figure 4.35: Time response and correlation of spectra response to θ_c^+ perturbation. Hovering condition. Correlation among BEM simulations and prediction given by $\lambda - f$ state-space model. ● BEM; —— upper rotor —— lower rotor state space model. Vertical lines indicate the $0.2/rev$ and $0.4/rev$ harmonics of Eq. 4.2

Advancing rotor

In order to test the inflow models during forward flight condition, for a perturbation of lateral cyclic pitch on single rotor configuration, following the time evolution given in Eq. 4.1 (expressed in deg), the λ_s and λ_c responses provided by the $\lambda - q$ and $\lambda - f$

finite-state model are presented in figs. 4.36(a) and 4.36(b)

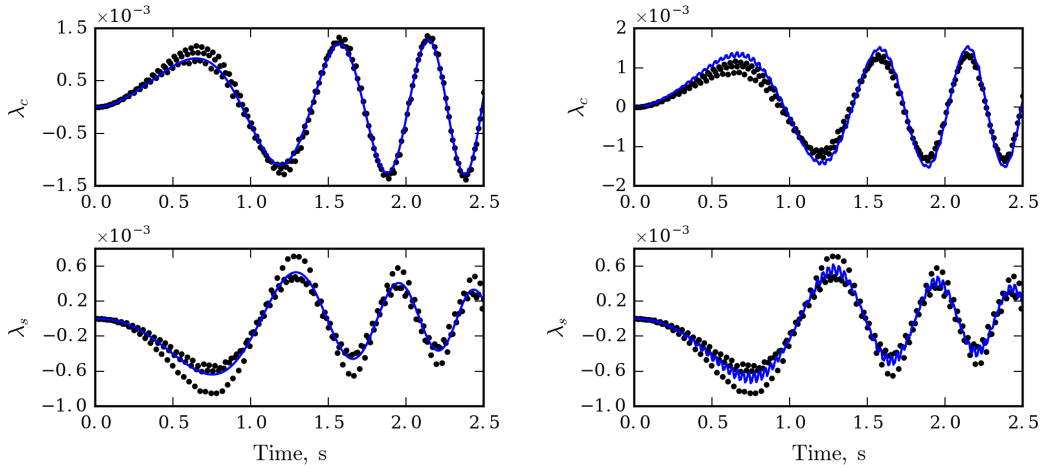

(a) $\lambda - q$ model (b) $\lambda - f$ model

Figure 4.36: Time response to θ_c^+ perturbation. Forward flight condition. Correlation among BEM simulations and predictions given by the state-space models. ● BEM; — state-space model.

The two results are in very good agreement, with the observable small discrepancies due to the lack of the multi-harmonic terms in the LTI model.

For the coaxial configuration, considering a perturbation of blade cyclic pitch, θ_c^+, following eq. 4.1, figs. 4.37(a) and 4.37(b) depicts the corresponding upper and lower rotor inflow component $\lambda_0^{u,l}$ and $\lambda_c^{u,l}$, as predicted by the BEM solver and by the kinematic finite-state model. The time responses provided by the finite-state model predict with good accuracy the low-frequency content of the nonlinear BEM solution, but again are not capable to capture the harmonic content around the $3/rev$ due to the periodicity of wake effects in forward flight combined with input frequencies (namely, $3\Omega\omega(t)$), and that around the $6/rev$ (due also to the mutual aerodynamic interference of coaxial rotors, in addition to multiple harmonic effect of forward flight wake configuration). As already observed for the hovering case analysis, these LTP output components are missing, in that the proposed model is of LTI type.

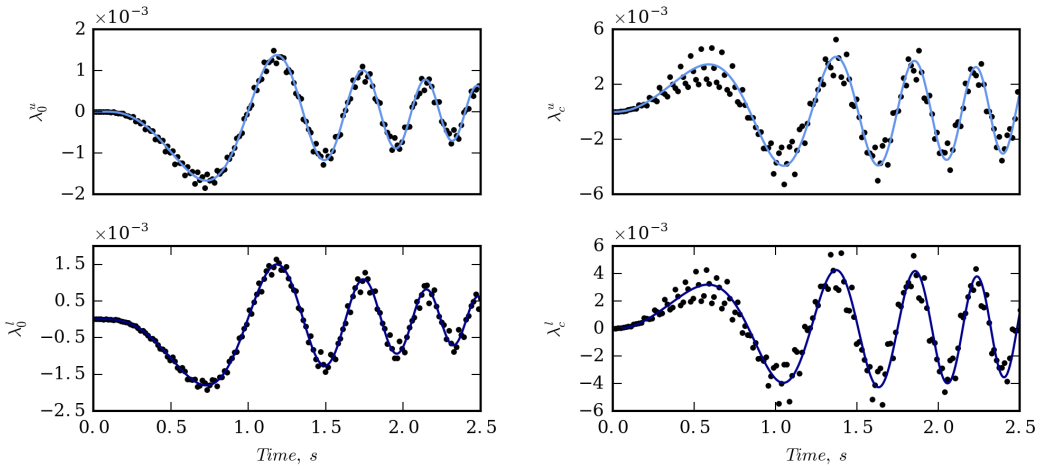

(a) $\lambda - q$ model

(b) $\lambda - q$ model

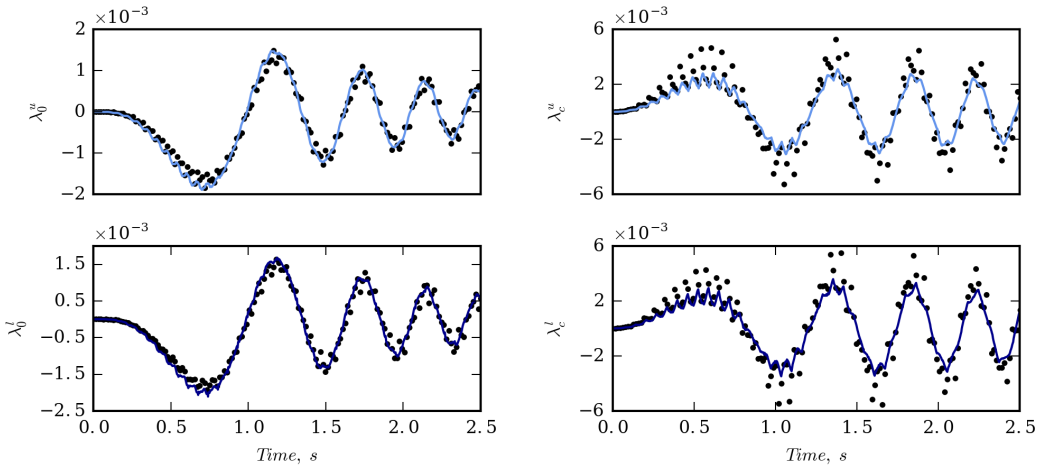

(c) $\lambda - f$ model

(d) $\lambda - f$ model

Figure 4.37: Time response to θ_c^+ perturbation. Forward flight condition. Correlation among BEM simulations and predictions given by the state-space models. ● BEM; upper rotor lower rotor state space model

Figures 4.37(c) and 4.37(d) show the $\lambda_0^{u,l}$ and $\lambda_c^{u,l}$ responses determined through the $\lambda - f$ model $\hat{\mathbf{H}}_\theta$. The $3/rev$ components included in the input loads of the model are the source of the higher frequency content observed and hence of the overall better quality of these predictions with respect to those obtained by the kinematic state-space model.

4.3 Linear Time Periodic models

The transfer functions between kinematics input and inflow coefficients of the linear time periodic model and their RMA are here examined. However it is believed that showing all the relevant transfer function of the models is useless. Some of them are showed in order to present the quality of the RMA. The main focus of this section is the quality of the inflow prediction by the finite state model based on a more accurate azimuthal and radiao inflow description.
The most accurate inflow description based on eq. 2.1 is considered with (if not otherwise specified) $N_r^0 = N_r^c = N_r^s = N_r^{N/2} = 4$, $\phi_j^0 = \phi_j^s = \phi_j^c = \phi_j^{N/2}$. Moreover even if for the single rotor configuration in hovering flight condition the aerodynamic operator is time constant for its nature, results regarding the wake inflow state space and the time marching validation are still presented here in order to test the capability of the more accurate inflow radial description. If not specified otherwise, the frequency range examined is in $[0, 2/rev]$ for both rotor configuration.

Model identification and rational matrix approximation

Hovering rotor

For the single rotor configuration in this flight condition the aerodynamic operator is of time constant nature, and thereby multi-harmonic inflow parameters are not introduced. However, considering the evolution of the inflow representation of eq. 2.1, the excellent quality of the RMA applied to the transfer functions samples extracted from the BEM solver is shown in figs. 4.38(a) and 4.38(b), which present the frequency behavior of λ_1^0 vs θ_0 and λ_1^{1s} vs θ_c , respectively. A similar high level of accuracy is observed for all of the transfer functions involved in matrix $\mathbf{H}_q$ for the hovering case.

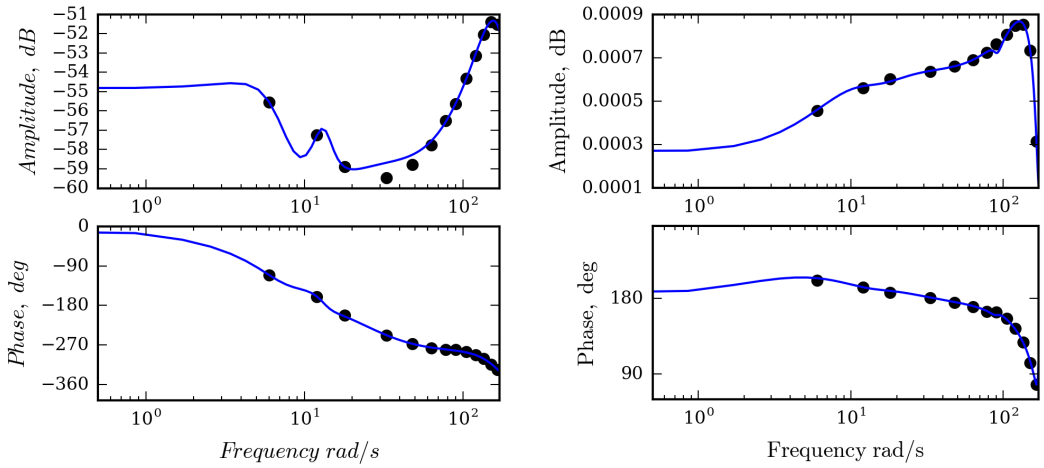

(a) λ_1^0 vs θ_0 (b) λ_1^s vs θ_c

Figure 4.38: Transfer functions between blade pitch control and inflow coefficients. ● samples; —— RMA

As confirmed by the results in the previous section, the coaxial configuration is characterized by a time periodic aerodynamic operator even for hovering flight conditions, with periodicity related to the total number of blades. The good quality of the RMA of the transfer functions extracted from the BEM solver is demonstrated in fig. 4.39, which presents the frequency behavior of $\lambda_1^{0,0}$ vs θ_0^+ for the upper and lower rotor. A similar level of accuracy is observed for all of the transfer functions in matrix **MH**.

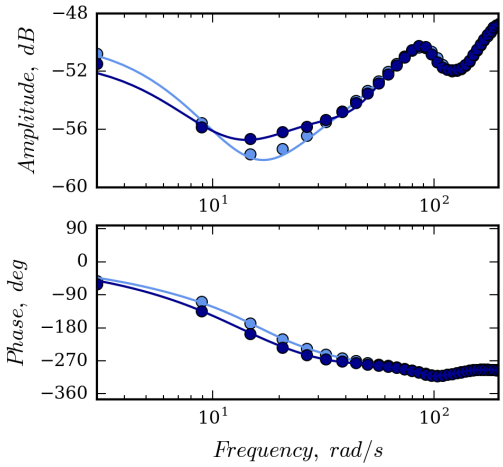

Figure 4.39: Transfer function $\lambda_1^{0,0}$ vs θ_0. Hovering condition. ● samples — RMA upper rotor, — RMA lower rotor.

Advancing rotor

Regarding the forward flight condition first, figs. 4.40(a) and 4.40(b), present two examples of transfer functions, respectively $\lambda_{0,1}^{0}$ vs θ_0 and $\lambda_{c,2}^{2c}$ vs θ_s for the single rotor configuration. These figures demonstrate that the applied RMA is of excellent accuracy

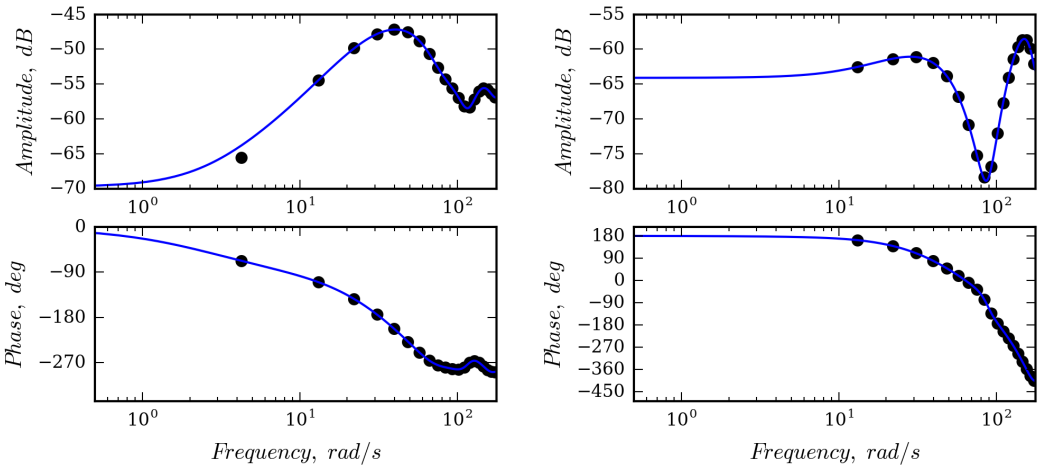

(a) $\lambda_{0,1}^{0}$ vs θ_0 (b) $\lambda_{c,2}^{2c}$ vs θ_s

Figure 4.40: Transfer functions between blade pitch control and inflow coefficients. Forward flight condition. ● BEM; — RMA

The same good agreement between the sample transfer function and its RMA approximation is showed in fig. 4.41 relating $\lambda_3^{0,0}$ vs θ_0^+ for the coaxial configuration.

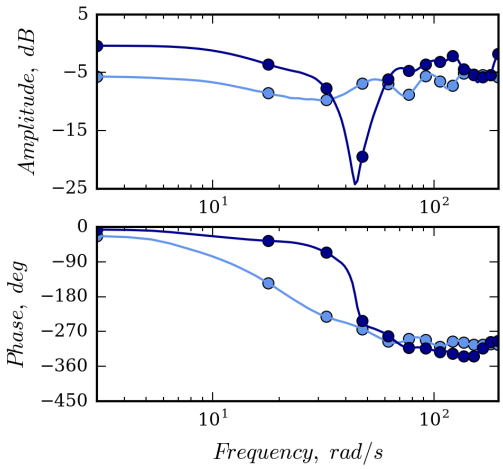

Figure 4.41: Transfer function $\lambda_3^{0,0}$ vs θ_0. Forward flight condition. ● samples — RMA upper rotor, — RMA lower rotor.

4.3.1 Time marching validation

As for the linear time invariant case, a time marching test of the proposed linear time periodic model is here presented both for the single and coaxial rotor configurations. Moreover, the differences in terms of wake inflow prediction between the approximation formulas 2.1 and 1.1 are pointed out.

Hovering rotor

Considering a collective pitch perturbation, θ_0, for the single rotor configuration following the time history of eq. 4.1, the wake inflow perturbations predicted by the finite state models are correlated with those directly computed by the BEM solver. In particular the state space deriving from the two approximating formula of the present model and the Pitt-Peters like approximation are compared. This comparison is shown in fig. 4.42 for the wake inflow evaluated at three blade sections, $r/R = [0.74, 0.9, 0.97]$. These results demonstrate the capability of the innovative approximating formula to capture

with good accuracy the radial distribution of the wake inflow that, especially at the tip of the blade, shows significant gradients.

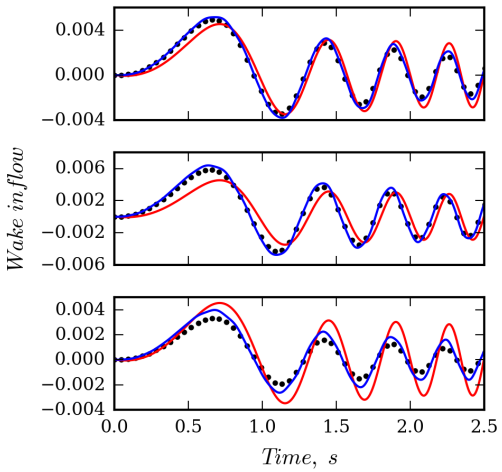

Figure 4.42: Wake inflow response at $r/R = 0.74$ **(top)**, $r/R = 0.9$, $r/R = 0.97$ **(bottom)** to θ_0 perturbation. Hovering condition. Correlation among BEM simulation and prediction given by state space models. ● BEM, —— state space present model, —— state space linear Pitt-Peters like

A more complete view of the relevant enhancements introduced by the radial approximation expressed by the series expansions in 2.6 is given in fig. 4.43. It presents the spanwise distributions of the percentage prediction error (related to the sectional inflow peak) obtained by the two approximating formulas. The improvement of the inflow prediction provided by the more accurate radial description is considerable throughout the blade span.

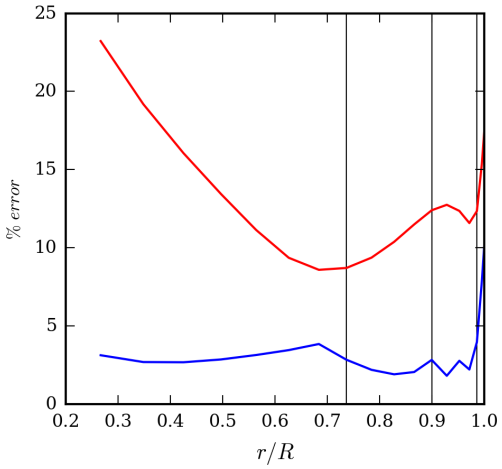

Figure 4.43: Spanwise error distribution. Hovering condition. — present model, — linear Pitt-Peters like

Next, considering the following time history of θ_0^+ perturbation

$$\theta_0^+(t) = Acos(0.1\Omega t)sin(0.3\Omega t)e^{0.25t} \tag{4.3}$$

with $A = 0.5\ deg$ applied to the coaxial configuration. The corresponding wake inflow perturbations are correlated both with those directly computed by the BEM solver. This comparison is shown in figs. 4.44(a) and 4.44(b) for the wake inflow evaluated at three blade sections, $r/R = [0.41, 0.62, 0.95]$, respectively on upper and lower rotor. Also for the coaxial configuration the Pitt-Peters like model leads to a rough approximation of the inflow velocity, especially at the tip and at the root of the blades, whereas the proposed model provides very good predictions of the inflow at any spanwise position.

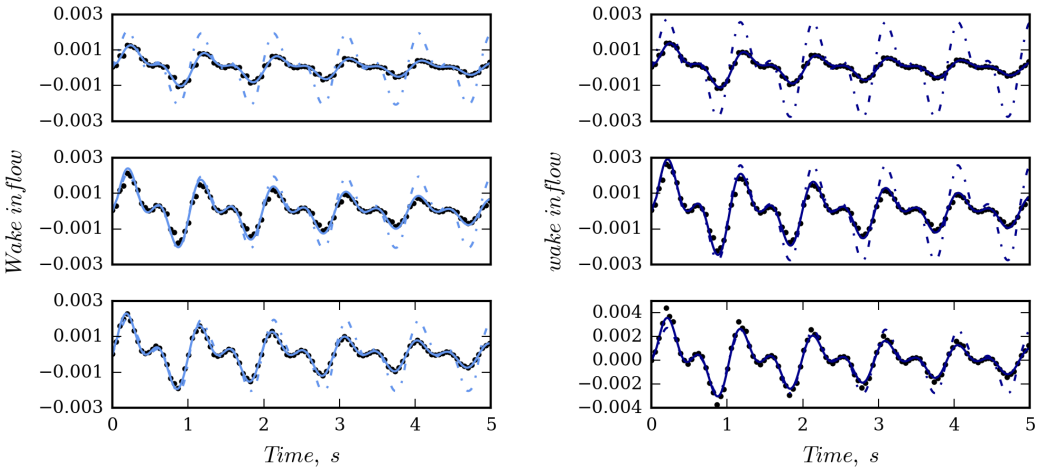

Figure 4.44: Wake inflow response at $r/R = 0.41$ **(top)**, $r/R = 0.62$, $r/R = 0.95$ **(bottom)** to θ_0^+ perturbation. Hovering condition. Correlation among BEM simulation and prediction given by state space models. ● BEM —— upper rotor state space present model, -·-·- upper rotor state space Pitt-Peters like, —— lower rotor state space present model, -·-·- lower rotor state space Pitt-Peters like

Figure 4.45 presents the spanwise distributions of the percentage of the error rms with respect to the sectional inflow peak, obtained by the approximating formulas. The improvement of the inflow prediction provided by the present radial description is considerable throughout the blade span. Note that the vertical solid lines identify the blade sections examined in fig. 4.44

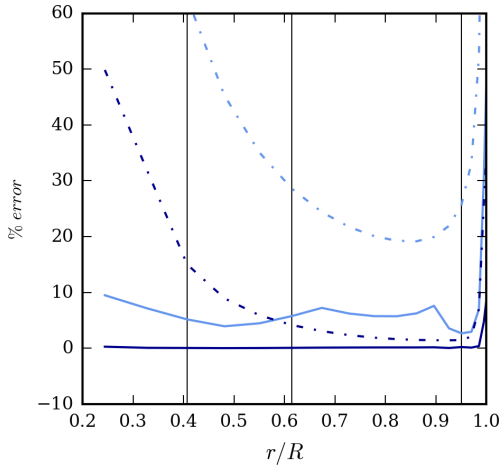

Figure 4.45: Spanwise error distribution for hovering condition. present model upper rotor, Pitt-Peters like upper rotor, present model lower rotor, Pitt-Peters like lower rotor

Advancing rotor

Considering now the following perturbation on β_0 for the single rotor configuration

$$\beta_0 = Acos(1.2\Omega t)sin(0.2\Omega t)e^{-0.25t} \tag{4.4}$$

with $A = 1\ deg$. Figure 4.46 shows the comparison between the wake inflow coefficients predicted by the finite state model and the one directly computed by the BEM solver. The results are in almost perfect agreement as attested also in fig. 4.47 that shows the spectra comparison between the finite state prediction and the computed signal on $\lambda_{0,1}$ and $\lambda_{N/2,1}$. A good agreement is also observed for all the other coefficients.

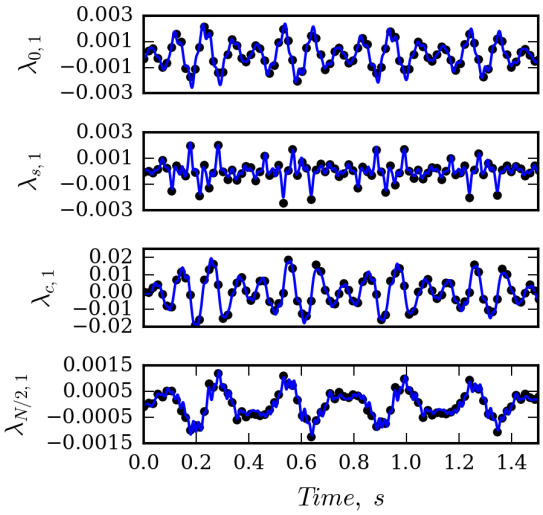

Figure 4.46: Time response to β_0 perturbation. Forward flight condition. Correlation among BEM simulations and state-space model. ● BEM, —— present model state space.

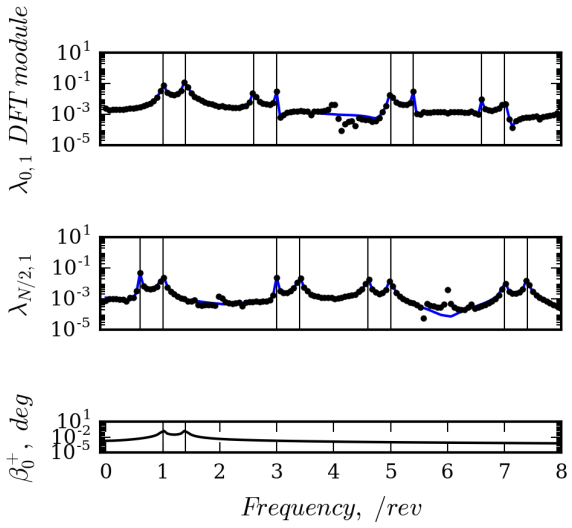

Figure 4.47: Correlation of spectra response to β_0 perturbation. Forward flight condition. Correlation among BEM simulations and prediction by the state-space model. ● BEM, —— present model state space.

Figure 4.48 shows the wake inflow evaluated at three blade sections $r/R = [0.54, 0.72, 1]$.

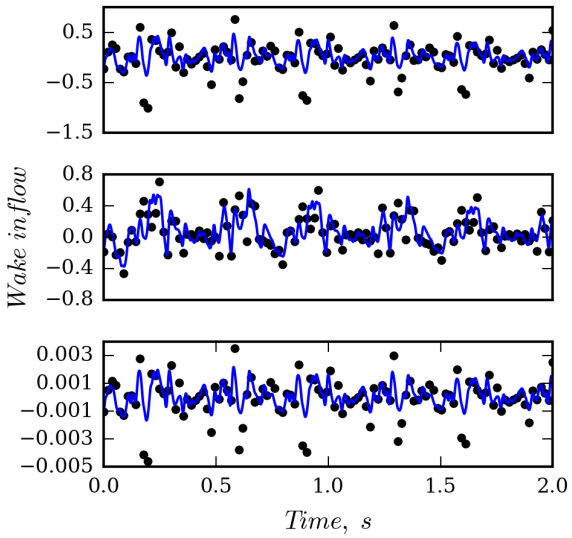

Figure 4.48: Wake inflow response ar $r/R = 0.54$**(top)**, $r/R = 0.72$, $r/R = 1$**(bottom)** response to β_0 perturbation. Forward flight condition. Correlation among BEM simulation and prediction given by state space model. ● BEM, —— present model

The quality of the finite state inflow prediction compared to the computed one is not as good as for the inflow coefficients. This is probably due to a poor radial description of the inflow. Increasing the number of the shape functions in 2.6, the spanwise error goes down as showed in fig. 4.49. Indeed utilizing $\phi^0 = \phi^s = \phi^c = \phi^{N/2}$ with $N_r^0 = N_r^s = N_r^c = N_r^{N/2} = N = 7$ there is an error reduction of 50%, while using $N = 12$ the error decrease around 65%. However fig. 4.50 presents the spanwise distributions of the percentage prediction error obtained by the present model utilizing just four shape function and the Pitt-Peters approximationn. The improvement of the inflow prediction is still considerable throughout the blade span.

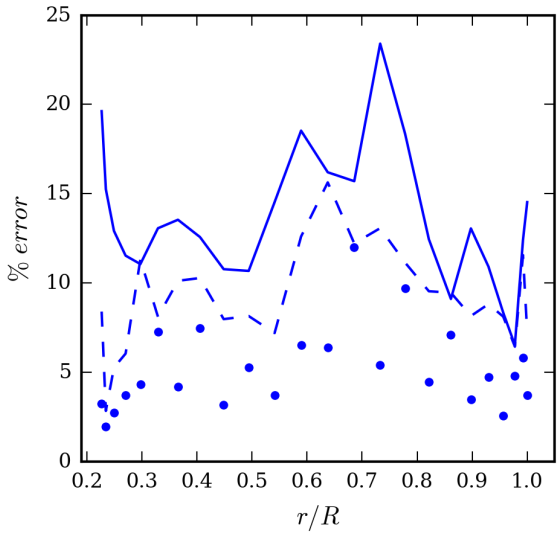

Figure 4.49: Spanwise error distribution. Forward flight condition. Infow approximation by different number of shape functions. —— $N = 4$, - - - $N = 7$, ● $N = 12$

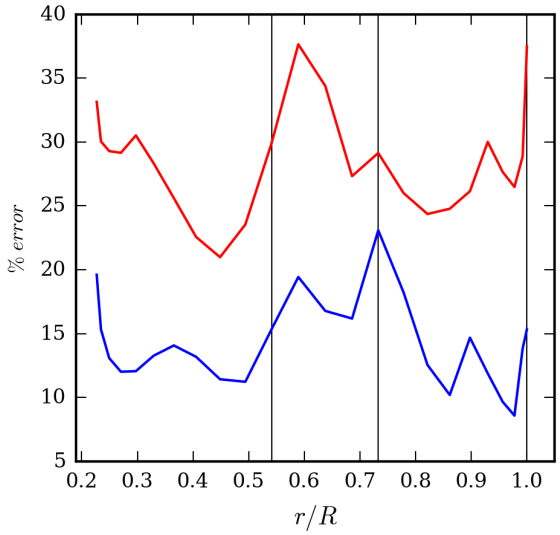

Figure 4.50: Spanwise error distribution. Forward flight condition. —— present model , —— linear Pitt-Peters like

Finally, considering a θ_0^+ perturbation for the coaxial configuration equal to that employed for the hovering case (see eq. (4.3)), fig. 4.51 shows the comparison between the wake inflow predicted by the present finite-state model and that provided by the

BEM solver at the three blade sections examined above for the hovering condition.

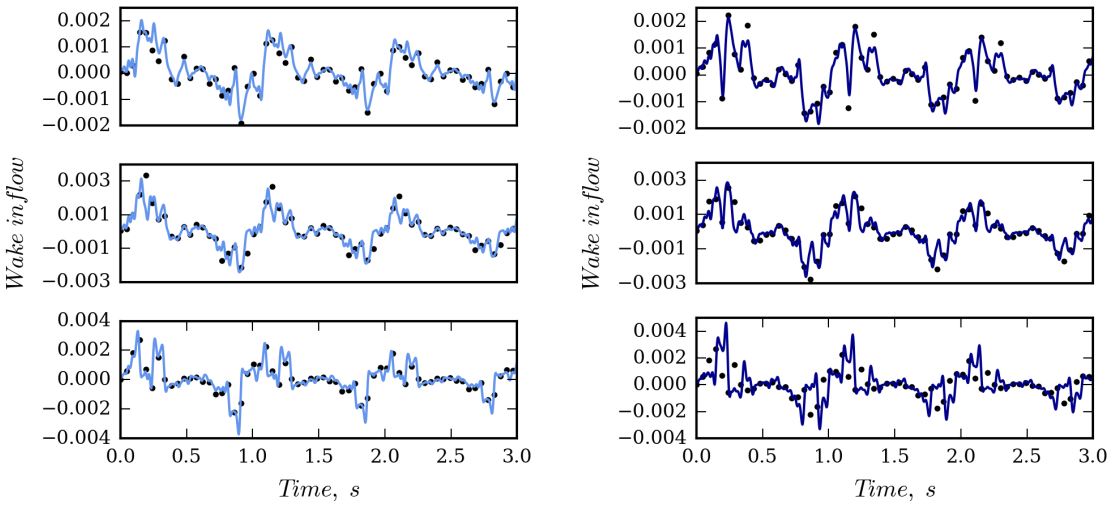

(a) (b)

Figure 4.51: Wake inflow response at $r/R = 0.7$ **(top)**, $r/R = 0.85$, $r/R = 0.95$ **(bottom)** to θ_0^+ perturbation. Forward flight condition. Correlation among BEM simulation and prediction given by state space model. ● BEM — present model upper rotor, — present model lower rotor

The two simulations are in quite good agreement, thus proving the capability of the introduced space-time-accurate finite-state model to describe with a good level of accuracy the wake inflow field over coaxial rotor systems. In forward flight the time periodicity of the aerodynamic operator heavily affects the output. This is particularly evident in Fig. 4.52 which presents the frequency spectrum of the upper rotor inflow parameter $\lambda_{s,3}$: indeed, in this case, the amplitude of the first multi-harmonic, 3/rev component is of the same order of magnitude of the LTI component (namely, that at the same frequency of the input).

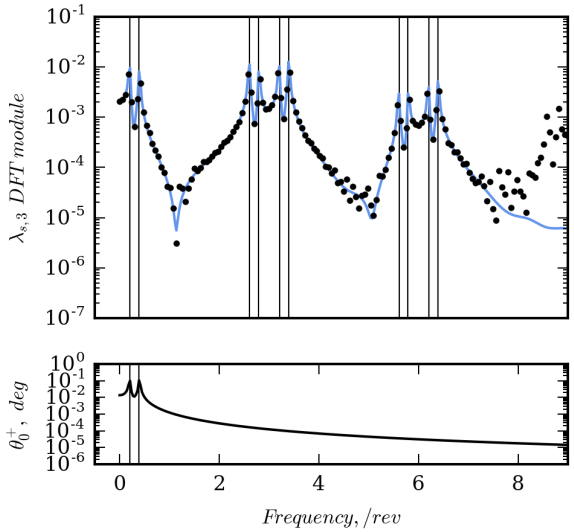

Figure 4.52: Correlation of spectra response to θ_0^+ perturbation. Forward flight condition. Correlation among BEM simulation and prediction given by state-space model prediction. ● BEM, —— present model upper rotor

In fig. 4.53 for the upper and lower rotor the spanwise distribution of the percentage prediction error is shown for (i) the inflow given by present model, with and without multi-harmonic terms, (ii) that predicted by the Pitt-Peters-like model (iii) and that directly obtained from projecting the sampled BEM inflow distribution on the radial basis functions, without using the finite-state approximation. The latter error is related only to the choice of the radial expansion employed for the wake inflow approximation.

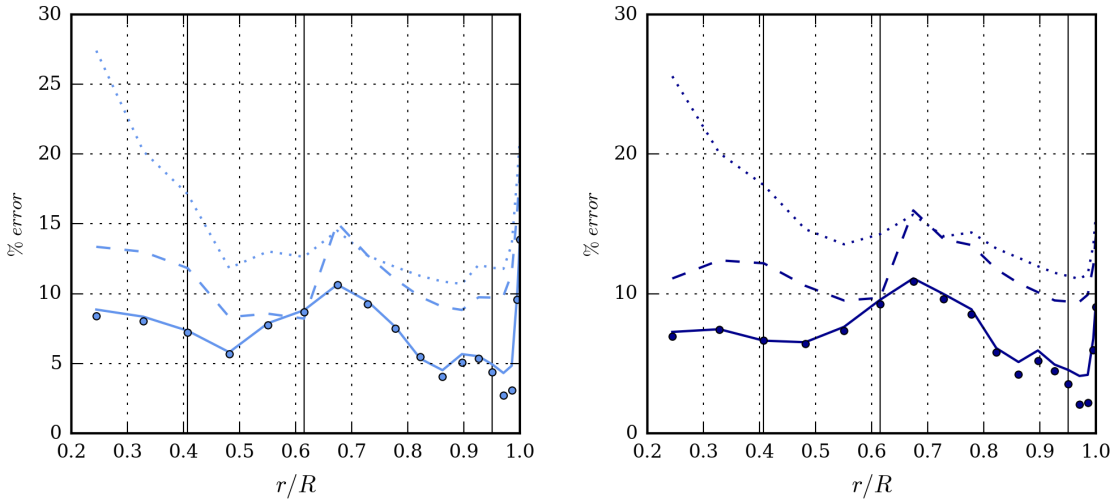

Figure 4.53: Spanwise error distributions. Forward flight condition. —— present model upper rotor —— present model lower rotor - - - w/o multi-harmonic terms; - · - · - Pitt-Peters-like model; • w/o finite-state approximation.

From these figures it can be observed that, with respect to the linear Pitt-Peters-like model, introducing only a more detailed radial description and excluding multi-harmonics contributions leads to limited improvements of the overall quality of the inflow approximation. This confirms that for forward flight conditions, combined time-space accurate descriptions are required for high quality inflow modelling. Moreover, the comparison of the bullet markers with the solid line in fig. 4.53 shows that the proposed methodology (identification process, harmonics truncation, rational matrix approximation) does not introduce significant errors.

4.4 Flight mechanics simulation results

In this section, for the single rotor configuration, the effect of the different inflow models identified on helicopter dynamics prediction is assessed. In particular, the state space of the $v-q$ and $v-f$ models based on free wake aerodynamic simulations are used. A briefly description of the flight mechanics simulation tool and the implementation of the dynamic inflow models into it is presented in appendix C

4.4.1 Helicopter aeromechanics

Then, the effect of the different inflow models considered on helicopter dynamics prediction is assessed.

First, the effect of the wake inflow models considered on aeromechanics eigenvalues and eigenvectors is examined. Figures 4.54 and 4.55 show the poles of the aeromechanics transfer functions provided by the kinematic-based wake inflow model ($\boldsymbol{H}_q$), the loads-based inflow models derived through four different kinematic perturbations ($\hat{\boldsymbol{H}}_\theta$, $\hat{\boldsymbol{H}}_\Omega$, $\hat{\boldsymbol{H}}_V$, $\hat{\boldsymbol{H}}_\beta$), and the Pitt-Peters model ($\mathbf{H}_{PP}$).

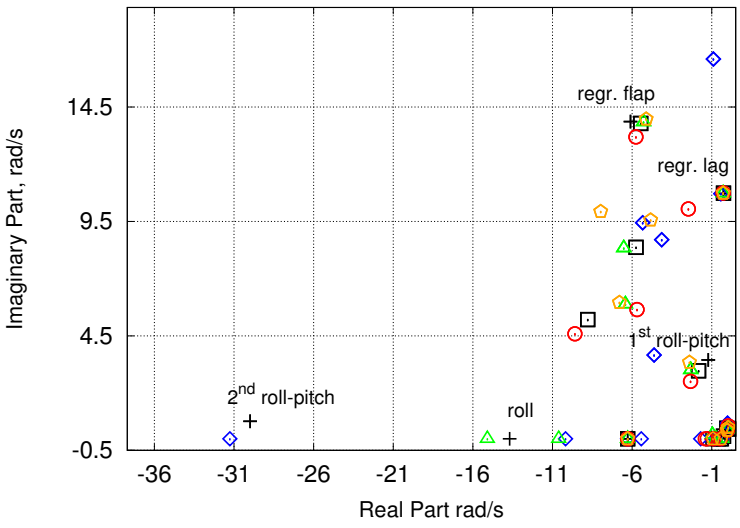

Figure 4.54: Aeromechanics roots determined by different inflow models. $\hat{\mathbf{H}}_\theta$, $\hat{\mathbf{H}}_V$, $\hat{\mathbf{H}}_\beta$, $\hat{\mathbf{H}}_\Omega$, $\mathbf{H}_q$, + $\mathbf{H}_{PP}$.

Relevant differences may be observed on some of the poles, and specifically those related to phugoid, roll-pitch oscillations, roll subsidence, dutch roll, spiral and heave

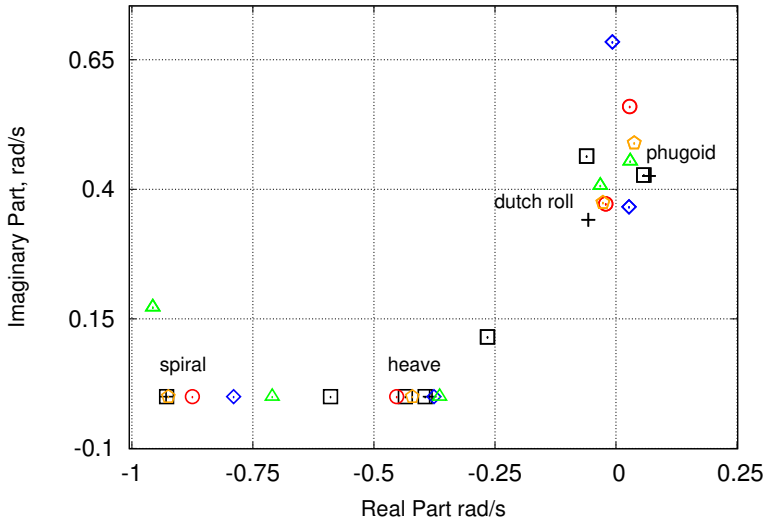

Figure 4.55: Aeromechanics roots determined by different inflow models, detail $\hat{\mathbf{H}}_\theta$, $\hat{\mathbf{H}}_V$, $\hat{\mathbf{H}}_\beta$, $\hat{\mathbf{H}}_\Omega$, $\mathbf{H}_q$, + $\mathbf{H}_{PP}$.

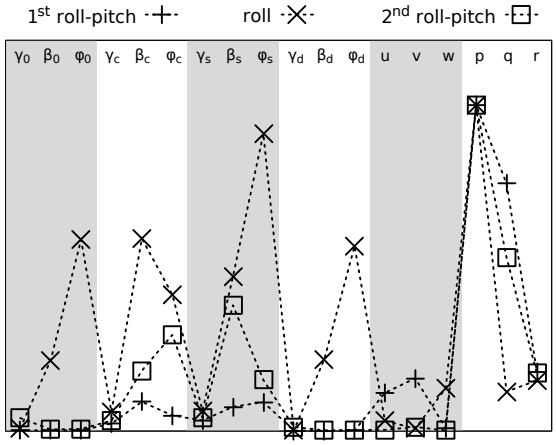

Figure 4.56: Eigenvectors associated to the poles in Fig. 4.54.

subsidence modes (figs. 4.56 and 4.57 depict the magnitude of the most relevant components of the eigenvectors associated to the flight dynamics poles, as obtained by the Pitt-Peters inflow). Note that, also low-frequency aeroelastic poles (regressive lag and regressive flap), since coupled with flight dynamics modes, are affected by wake inflow model change.

Finally, the main aeromechanics transfer functions are examined in detail. Figures 4.58 to 4.61 depict five transfer functions, respectively w vs θ_0, p vs θ_c, r vs θ_p and p vs θ_s

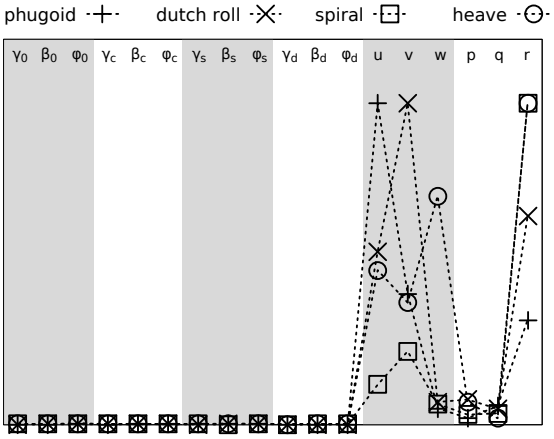

Figure 4.57: Eigenvectors associated to the poles in Fig. 4.55.

(with θ_p denoting tail rotor collective pitch), each evaluated through application of the kinematic-based, loads-based wake inflow models and the Pitt-Peters model.
The first three represent on-axis responses of the vehicle, whereas the fourth is representative of the cross-coupling typical of helicopter dynamics (due to the lack of symmetry in the xz plane). In the range of frequency examined, the most relevant discrepancies among the predictions from the different wake inflow models, are in the region of the low-damped/unstable flight dynamics poles (*i.e.* 0.6 rad/s). It is worth noting that, the presence of a stability augmentation system is expected to reduce the differences between the transfer function, due to the increase of mode damping. In some cases (w vs θ_0 and r vs θ_p), the kinematic-based inflow model produces different responses far from poles, as well. This is expected, since the kinematic model takes into account phenomena that are neglected by loads-based models like, for instance, the deformation of the rotor wake due to the motion of trailing edge [45].

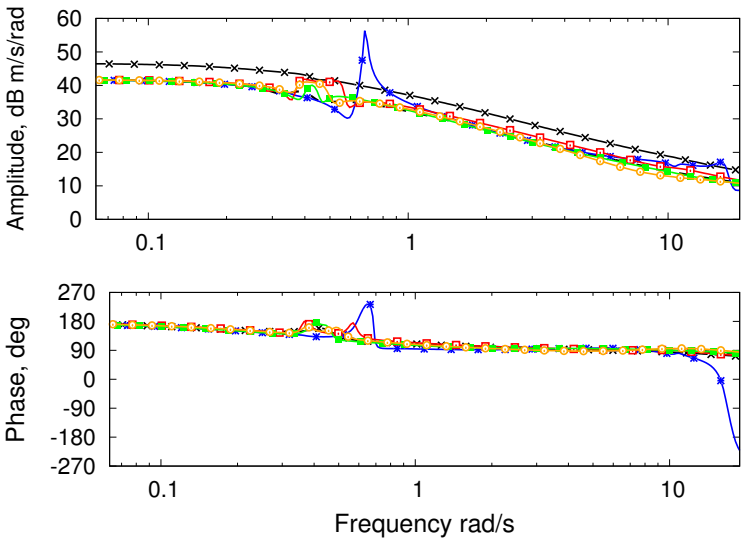

Figure 4.58: Transfer function w vs θ_0 $\hat{\mathbf{H}}_\theta$, $\hat{\mathbf{H}}_V$, $\hat{\mathbf{H}}_\beta$, $\hat{\mathbf{H}}_\Omega$, $\mathbf{H}_q$, - - -$\mathbf{H}_{PP}$.

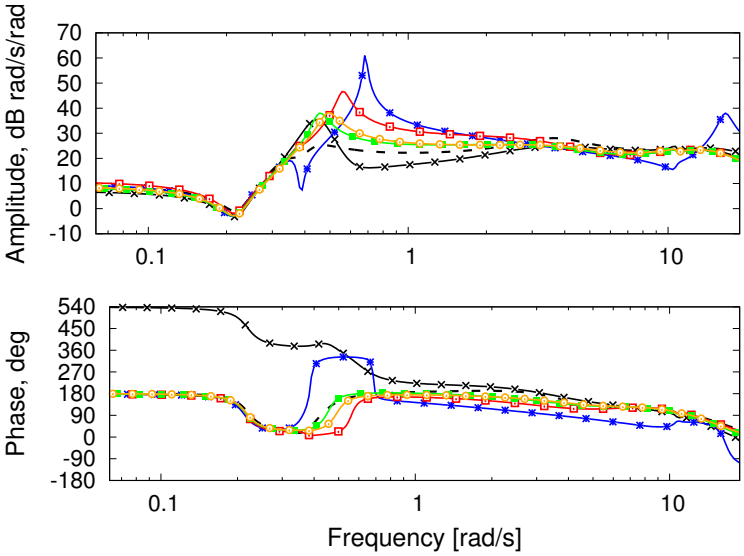

Figure 4.59: Transfer function p vs θ_c. $\hat{\mathbf{H}}_\theta$, $\hat{\mathbf{H}}_V$, $\hat{\mathbf{H}}_\beta$, $\hat{\mathbf{H}}_\Omega$, $\mathbf{H}_q$, - - -$\mathbf{H}_{PP}$.

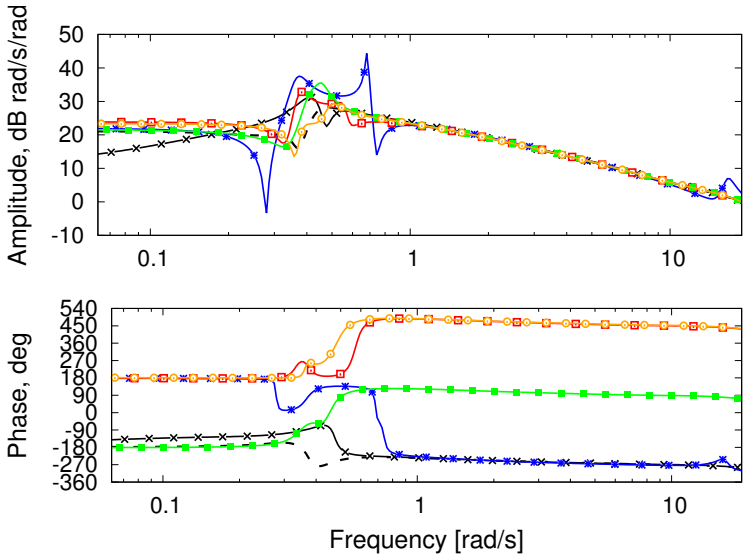

Figure 4.60: Transfer function r vs θ_p. $\hat{\mathbf{H}}_\theta$, $\hat{\mathbf{H}}_V$, $\hat{\mathbf{H}}_\beta$, $\hat{\mathbf{H}}_\Omega$, $\mathbf{H}_q$, - - -$\mathbf{H}_{PP}$.

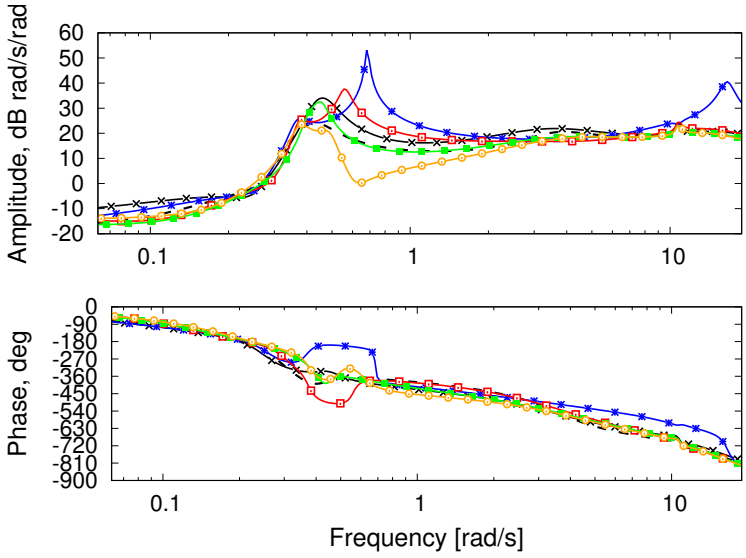

Figure 4.61: Transfer function p vs θ_s. $\hat{\mathbf{H}}_\theta$, $\hat{\mathbf{H}}_V$, $\hat{\mathbf{H}}_\beta$, $\hat{\mathbf{H}}_\Omega$, $\mathbf{H}_q$, - - -$\mathbf{H}_{PP}$.

Concluding remarks

Finite-state modeling of dynamic wake inflow on single and coaxial rotors configurations in arbitrary steady motion has been proposed. These dynamic inflow models are determined through time-transformation of the rational approximation of the corresponding transfer functions which, in turn, are extracted from a high-fidelity aerodynamic solver by system identification techniques.

The extracted models are based on an innovative wake inflow approximation formula capable of rigorously predicting the inflow flow field. Two different dynamic inflow version have been developed: a time invariant and a time periodic version (capable of taking into consideration higher harmonics behavior of the inflow). In particular, for the time invariant version two models have been presented: the $\lambda - q$ model relates inflow coefficients to flight dynamics variables, whereas the $\lambda - f$ one relates inflow coefficients to thrust and aerodynamic in-plane moments (namely, rolling and pitching). On the other hand the time periodic dynamic inflow version concerns only the of $\lambda - q$ model where the inflow coefficients are related to flight dynamics variables as well as the elastic degrees of freedom of the blades. The time invariant models have been applied to flight mechanics simulations. The following conclusions are drawn from the numerical investigation:

- The inclusion of four radial shape functions for each inflow coefficients in the innovative inflow approximating formula, gives good results when the inflow approximation is compared with induced velocity predicted by the nonlinear BEM solver. Moreover the inclusion of the differential terms in the inflow approximation is mandatory when a higher harmonic description of the inflow is needed;
- The developed tool chain for the extraction of finite state wake inflow models have

been proven to be effective for all the flight conditions (hover and forward flight) and rotors analyzed (single and coaxial).
In this contest single harmonic and chirp input based methodology have been applied for extraction. Moreover it has been developed an innovative approach for the extraction of frequency response function from time periodic operator (advancing single rotor and hover/advancing coaxial rotors.)

- The applied RMA algorithm is able to identify with excellent accuracy the sampled transfer functions of wake inflow components, independently of the flight condition examined and the solution mode applied (prescribed or free-wake analysis);

- It has been proved that the wake shape used in the aerodynamic solver remarkably affects the inflow distribution. This suggest the use of free wake algorithm for a more realistic inflow prediction;

- The $\lambda - f$ model is not unique, but rather, it is dependent on the kinematic perturbation used to identify it; this is especially true for the single rotor configuration. Indeed for the coaxial configuration, this dependency is significantly reduced with respect to what is observed for single rotors and seems to have strong effects only on the description of minor transfer functions coupling lateral and longitudinal inflow coefficients;

- The observation of the transfer functions of the coaxial configuration reveals that the proposed model is capable of capturing the effects of mutual influence occurring between the two rotors; the mutual influence is stronger in hovering conditions than in forward flight. Thus the proposed methodology is perfectly capable of modeling rotor configurations that go beyond the traditional single main rotor helicopter. Moreover it takes into account all the complex aerodynamic phenomena deriving from strong aerodynamic interference, severe blade-vortex interactions, wake roll up and wake distortion (only if present in the utilized aerodynamic tool);

- Both for single and coaxial rotors configuration the time-marching validations reveal that for hovering and forward flight conditions, the proposed finite-state $\lambda - q$

linear time invariant models provide inflow coefficients responses to arbitrary rotor perturbations that are in very good agreement with those obtained directly by the time-marching BEM aerodynamic solver;

- In the case of load based model $\lambda - f$, the accuracy of the analytic time marching predictions both for single and coaxial configuration depends on the similarity between the rotor kinematic variables considered in the model identification process and those actually perturbed in the validation test;
- The time marching validations of the finite-state linear time periodic model provide an inflow in good agreement with the one obtained directly by the time-marching BEM solver. The improvement obtained by introducing radial shape functions and multi-harmonic components is remarkable;
- Higher-harmonic components related to mutual interactions between coaxial rotors and forward flight asymmetric effects are observed in the time responses predicted by the $\lambda - f$ model: these are introduced by the spectrum of the input rotor loads;
- For the test case helicopter Bo105 it has been proved that the dynamic inflow models applied ($\lambda - q/f$) strongly affect the aeromechanics response and stability;

Appendix

A. Nonlinear, separable-variable least-square approach for RMA

In this appendix, the numerical approach applied for the rational matrix approximation of transfer matrices is outlined. Considering, for instance, the rational matrix form in eq. (2.11), the constant-coefficient matrices are obtained as solution of the following nonlinear, least-square problem

$$\min_{\boldsymbol{A}_1,\boldsymbol{A}_0,\boldsymbol{A},\boldsymbol{B},\boldsymbol{C}} \left(\sum_{n=1}^{N_f} \|\boldsymbol{Q}(i\omega_n)\|_F^2 \right) \tag{4.5}$$

where $\|\cdot\|_F$ represents Frobenius norm of a matrix, ω_n is the discrete set of N_f frequencies at which the transfer matrix, $\boldsymbol{H}(s)$, is known (samples), whereas $\boldsymbol{Q}$ is the error matrix defined as

$$\boldsymbol{Q}(s) = s\boldsymbol{A}_1 + \boldsymbol{A}_0 + \boldsymbol{C}\left(s\boldsymbol{I} - \boldsymbol{A}\right)^{-1} \boldsymbol{B} - \boldsymbol{H}\left(s\right) \tag{4.6}$$

To solve this minimization problem several methods have been proposed in the literature (see [36] for a brief review of them). The minimization problem solution proposed here is an extension of the approach of [46], that uses the separable variables approach.

Considering 4.6 it can be observed that, for a given frequency ω_i, matrix $\boldsymbol{Q}$ depends linearly on the polynomial contribution matrices (namely, $\boldsymbol{A}_k$ for $k = 0, 1$) and that, for given $\boldsymbol{C}$ and $\boldsymbol{A}$ matrices, it is linearly dependent also on matrix $\boldsymbol{B}$. This feature of the approximation rational form applied is exploited to separate the minimization variables into two sets, a linear one and a nonlinear one.

First, the linear set of unknown variables is defined as the solution of the following algebraic problem derived from 4.6

$$\begin{bmatrix} i\omega_1 \boldsymbol{I} & \boldsymbol{I} & \boldsymbol{C}\left(i\omega_1 \boldsymbol{I} - \boldsymbol{A}\right)^{-1} \\ i\omega_2 \boldsymbol{I} & \boldsymbol{I} & \boldsymbol{C}\left(i\omega_2 \boldsymbol{I} - \boldsymbol{A}\right)^{-1} \\ \vdots & \vdots & \vdots \\ i\omega_{N_f} \boldsymbol{I} & \boldsymbol{I} & \boldsymbol{C}\left(i\omega_{N_f} \boldsymbol{C} - \boldsymbol{A}\right)^{-1} \end{bmatrix} \begin{bmatrix} \boldsymbol{A}_1 \\ \boldsymbol{A}_0 \\ \boldsymbol{B} \end{bmatrix} = \begin{bmatrix} \boldsymbol{Q}\left(i\omega_1\right) \\ \boldsymbol{Q}\left(i\omega_2\right) \\ \vdots \\ \boldsymbol{Q}\left(i\omega_{N_f}\right) \end{bmatrix} + \begin{bmatrix} \boldsymbol{Q}\left(i\omega_1\right) \\ \boldsymbol{H}\left(i\omega_2\right) \\ \vdots \\ \boldsymbol{H}\left(i\omega_{N_f}\right) \end{bmatrix} \tag{4.7}$$

where equation coefficients explicitly depend on the set of nonlinear variables, the unknowns are real numbers (entries of matrices $\boldsymbol{A}_1, \boldsymbol{A}_0$ and $\boldsymbol{B}$), whereas right hand side contributions have complex values.

Then, the set of nonlinear variables is defined as solution of a separate reformulated minimization problem, thus dealing with a drastically reduced size of solution domain. Indeed, rewriting 4.7 in a more compact notation as

$$\boldsymbol{M}\, \boldsymbol{X}_{lin} = \hat{\boldsymbol{Q}} + \hat{\boldsymbol{H}} \tag{4.8}$$

where $\boldsymbol{M}$ is the coefficient matrix, $\boldsymbol{X}_{lin}$ collects the matrices of the unknown linear variables, while $\hat{\boldsymbol{H}}$ and $\hat{\boldsymbol{Q}}$ denote, respectively, transfer function and residual matrices evaluated at the sampling frequencies, the optimal value of $\boldsymbol{X}_{lin}$ (least-square solution of 4.7) is formally given by

$$\boldsymbol{X}_{lin} = \boldsymbol{M}^* \hat{\boldsymbol{H}}. \tag{4.9}$$

with $\boldsymbol{M}^* = (\boldsymbol{M}^T \boldsymbol{M})^{-1} \boldsymbol{M}^T$ denoting the Moore-Penrose pseudoinverse of matrix $\boldsymbol{M}$, and the minimization problem concerning the nonlinear variables is formulated as follows

$$\min_{\boldsymbol{C},\boldsymbol{A}} \left(\left\| \hat{\boldsymbol{Q}} \right\|_F^2 \right) \tag{4.10}$$

with $\hat{\boldsymbol{Q}}$ not depending on $\boldsymbol{X}_{lin}$, as demonstrated by the combination of **??** that yields

$$\hat{\boldsymbol{Q}} = \left(\boldsymbol{M}\boldsymbol{M}^* - \boldsymbol{I}\right)\, \hat{\boldsymbol{H}} \tag{4.11}$$

4.10 is solved by a local minimization method based on the Broyden-Fletcher-Goldfarb-Shanno (BFGS) algorithm [47]. The gradient of the objective function required by the BFGS algorithm (namely, the partial derivatives of $f_{obj} = \left\| \hat{\boldsymbol{Q}} \right\|_F^2$ with

respect to the entries of $\boldsymbol{A}$ and $\boldsymbol{C}$) is evaluated through the method developed in [**?**]. Once the solution of 4.10 is determined, 4.9 directly yields the set of linear variables.

In principle, the minimization problem should be subject to a set of constraints imposing real part of poles (namely, the eigenvalues of matrix $\boldsymbol{A}$) to be negative (in order to let the finite-state form represent a stable system behaviour). However, it is observed that such constraints are automatically satisfied: this may be considered as an indication of the robustness of the presented approach, which allows application of the convenient unconstrained version of the BFGS algorithm.

B. High-fidelity rotor aerodynamic solver

In this work, wake inflow and blade loads are evaluated by an high fidelity aerodynamic solver based on a boundary element method for the solution of a boundary integral equation approach, suited for the analysis of potential flows around helicopter rotors in arbitrary flight conditions, included those where strong blade-vortex interactions occur [48]. It introduces the decomposition of the potential field into an incident field, φ_I, and a scattered field, φ_S. The scattered potential is generated by sources and doublets over the bodies surfaces and by doublets over portions of the wakes surfaces that are very close to the trailing edges from which they emanated (near wake, S_W^N). The incident potential is generated by doublets over the complementary wake regions that compose the far wakes, S_W^F. The scattered potential is discontinuous across S_W^N, whereas the incident potential is discontinuous across S_W^F. As demonstrated in [48], for $\varphi = \varphi_I + \varphi_S$, the scattered potential at an arbitrary observer position, $\boldsymbol{y}_*$, is given by

$$\varphi_S(\boldsymbol{y}_*, t) = \int_{S_B} \left[G\,(\chi - \chi_I) - \varphi_S \frac{\partial G}{\partial n} \right] \, dS(\boldsymbol{y}) - \int_{S_W^N} \Delta\varphi_S \, \frac{\partial G}{\partial n} \, dS(\boldsymbol{y}) \tag{4.12}$$

where $G = -1/4\pi \|\boldsymbol{y} - \boldsymbol{y}_*\|$ denotes the unit-source solution of the three-dimensional Laplace equation, $\chi = \boldsymbol{v}_B \cdot \boldsymbol{n}$ accounts for the impermeability boundary condition ($\boldsymbol{v}_B$ is the body velocity due to rigid and elastic kinematics, and $\boldsymbol{n}$ is the surface outward unit normal), whereas $\chi_I = \boldsymbol{u}_I \cdot \boldsymbol{n}$, with the far wake induced velocity, $\boldsymbol{u}_I$, given by [48]

$$\boldsymbol{u}_I(\boldsymbol{y}_*, t) \approx - \sum_{n=1}^{N} \Delta\varphi_S(\boldsymbol{y}_{W_n}^{TE}, t - \tau_n) \int_{C_n} \nabla_{\boldsymbol{x}} G \times d\boldsymbol{y} \tag{4.13}$$

where C_n denotes the contour line of the n-th far wake panel, $\boldsymbol{y}_{W_n}^{TE}$ is the trailing edge position where the wake material point currently in $\boldsymbol{y}_{W_n}$ emanated at time $t - \tau_n$.
Eq. 4.13 represents the velocity field given by the Biot-Savart law applied to the vortices having the shape of the far-wake panel contours and intensity $\Delta\varphi_S(\boldsymbol{y}_{W_n}^{TE}, t - \tau_n)$; it is applied to evaluate both the term χ_I in Eq. (4.12) and, once extended to the whole wake, the velocity field for the free-wake analysis, and wake inflow over the blades. The vortices at the panels contours are assumed to have a finite-thickness core (Rankine-vortex type vortices), in order to assure stable and regular solutions even in body-vortex impact conditions [48].
Eq. 4.12 is solved numerically by boundary elements, i.e by dividing S_B and $S_W \sup N$ into quadrilateral panels, assuming φ_S, χ, χ_I and $\Delta\varphi_S$ to be piecewise constant (zero-th order BEM), and imposing the equation to be satisfied at the center of each body element (collocation method).

Once the potential field is known, the Bernoulli theorem yields the pressure distribution that, suitably integrated over the blades surfaces, provides the aerodynamic loads (see [49] for details on the application of the Bernoulli theorem to the potential field decomposed into incident and scattered components).

C. Flight mechanics simulation tool with the inclusion of dynamic inflow models from high fidelity aerodynamic solver

The flight mechanics simulation tool utilized, *HELISTAB*, is a comprehensive helicopter code developed in the last decade at Roma Tre University. It considers rigid body dynamics, blade aeroelasticity, airframe elastic motion, as well as effects from actuators dynamics and stability augmentation systems. Passive and active pilot models are included, and both linear and nonlinear analyses may be performed. *HELISTAB* has been validated and applied within the activities of the European Project ARISTOTEL, addressed to the study of Rotorcraft-Pilot Couplings phenomena [50],[51]).
The linearized equations of aeromechanics are written as a first order differential system,

$$\dot{\boldsymbol{z}} = \boldsymbol{A}^{heli}\boldsymbol{z} + \boldsymbol{B}^{heli}\boldsymbol{u} \tag{4.14}$$

where $\boldsymbol{z}$ collects Lagrangian coordinates of elastic blade and airframe deformations and their derivatives, airframe rigid-body (center-of-mass) linear and angular velocity components, Euler angles and inflow states, $\boldsymbol{x}$, whereas $\boldsymbol{u}$ collects main and tail rotor controls and their first and second order derivatives, namely, $\boldsymbol{u} = \{\ddot{\theta}_0,\, \dot{\theta}_0,\, \theta_0,\, \ddot{\theta}_s, \ldots, \theta_p\}^T$. In the following, details concerning the derivation of matrices $\boldsymbol{A}^{heli}$ and $\boldsymbol{B}^{heli}$ in eq. 4.14 are provided for aeromechanics formulations using both kinematic-based and loads-based dynamic inflow models.

Kinematic-based inflow

Recasting the vector of state variables as $\mathbf{z} = \{\mathbf{y}\ \mathbf{x}\}^T$, coupling the rotor and airframe dynamics equations with the dynamic inflow model of df yields the following aeromechanics model

$$\begin{aligned}
\dot{\boldsymbol{y}} &= \boldsymbol{A}_y^{heli}\boldsymbol{y} + \boldsymbol{C}_\lambda^{heli}\boldsymbol{\lambda} + \boldsymbol{B}_y^{heli}\boldsymbol{u} \\
\boldsymbol{\lambda} &= \boldsymbol{A}_{1y}\dot{\boldsymbol{y}} + \boldsymbol{A}_{0y}\boldsymbol{y} + \boldsymbol{C}\boldsymbol{x} + \boldsymbol{A}_{0u}\boldsymbol{u} \\
\dot{\boldsymbol{x}} &= \boldsymbol{B}_y\boldsymbol{y} + \boldsymbol{A}\boldsymbol{x} + \boldsymbol{B}_u\boldsymbol{u}
\end{aligned} \tag{4.15}$$

with $\boldsymbol{C}_\lambda$ collecting the derivatives of the aerodynamic generalized forces of the aeromechanic model with respect to $\boldsymbol{\lambda}$. In addition, the matrices of the wake inflow model in 4.15 are obtained by re-organizing those in 2.15, to be consistent with the vectors of variables of the aeromechanic model (for instance, hub linear velocities considered in 2.15 are given as a combination of the airframe dofs considered in the vector $\boldsymbol{y}$). Then, substituting the inflow model in the rotor/airframe dynamics equations, the following set of first-order differential equations governing the helicopter dynamics are obtained

$$\begin{aligned}
\dot{\boldsymbol{y}} &= \left(\boldsymbol{I} - \boldsymbol{C}_\lambda^{heli}\boldsymbol{A}_{1y}\right)^{-1}\left[\left(\boldsymbol{A}_y^{heli} + \boldsymbol{C}_\lambda^{heli}\boldsymbol{A}_{0y}\right)\boldsymbol{y} + \right. \\
&\left. + \boldsymbol{C}_\lambda^{heli}\boldsymbol{C}\boldsymbol{x} + \left(\boldsymbol{B}_y^{heli} + \boldsymbol{C}_\lambda^{heli}\boldsymbol{A}_{0u}\right)\boldsymbol{u}\right] \\
\dot{\boldsymbol{x}} &= \boldsymbol{B}_y\boldsymbol{y} + \boldsymbol{A}\boldsymbol{x} + \boldsymbol{B}_u\boldsymbol{u}
\end{aligned} \tag{4.16}$$

from which matrices $\boldsymbol{A}^{heli}$ and $\boldsymbol{B}^{heli}$ of 4.14 may be easily identified.

Load-based inflow

When load-based inflow model is used, the aeromechanics equations may be written as

$$\begin{aligned} \dot{\boldsymbol{y}} &= \boldsymbol{A}_y^{heli}\boldsymbol{y} + \boldsymbol{C}_\lambda^{heli}\boldsymbol{\lambda} + \boldsymbol{B}_y^{heli}\boldsymbol{u} \\ \boldsymbol{\lambda} &= \boldsymbol{C}\boldsymbol{x} \\ \dot{\boldsymbol{x}} &= \boldsymbol{A}\boldsymbol{x} + \boldsymbol{B}_f\boldsymbol{f} \end{aligned} \tag{4.17}$$

where the perturbative hub loads appearing in 4.17 are given by the following linearized form

$$\boldsymbol{f} = \boldsymbol{F}_y^{heli}\boldsymbol{y} + \boldsymbol{F}_\lambda^{heli}\boldsymbol{\lambda} + \boldsymbol{F}_u^{heli}\boldsymbol{u} \tag{4.18}$$

Finally, combining 4.17and 4.18 yields the following set of first-order differential equations governing the helicopter dynamics

$$\begin{aligned} \dot{\boldsymbol{y}} &= \boldsymbol{A}_y^{heli}\boldsymbol{y} + \boldsymbol{C}_\lambda^{heli}\boldsymbol{C}\boldsymbol{x} + \boldsymbol{B}_y^{heli}\boldsymbol{u} \\ \dot{\boldsymbol{x}} &= \boldsymbol{B}_f\boldsymbol{F}_y^{heli}\boldsymbol{y} + \big(\boldsymbol{A} + \boldsymbol{B}\boldsymbol{F}_\lambda\boldsymbol{C}\big)\boldsymbol{x} + \boldsymbol{B}_f\boldsymbol{F}_u^{heli}\boldsymbol{u} \end{aligned} \tag{4.19}$$

from which matrices $\boldsymbol{A}^{heli}$ and $\boldsymbol{B}^{heli}$ of 4.14 may be readily identified.

Bibliography

[1] W. Van Hoydonck, H. Haverdings, and M. Pavel, "A review of rotorcraft wake modeling methods for flight dynamics applications," 2009.

[2] A. Bagai, J. G. Leishman, and J. Park, "Aerodynamic analysis of a helicopter in steady maneuvering flight using a free-vortex rotor wake model," *Journal of the American Helicopter Society*, vol. 44, no. 2, pp. 109–120, 1999.

[3] T. Quackenbush, J. Keller, D. Wachspress, and A. Boschitsch, "Reduced order free wake modeling for near real time simulation of rotorcraft flight mechanics," in *ANNUAL FORUM PROCEEDINGS-AMERICAN HELICOPTER SOCIETY*, vol. 55, pp. 481–497, 1999.

[4] C. Theodore and R. Celi, "Flight dynamic simulation with refined aerodynamics and flexible blade modeling," in *ANNUAL FORUM PROCEEDINGS-AMERICAN HELICOPTER SOCIETY*, vol. 56, pp. 857–872, AMERICAN HELICOPTER SOCIETY, INC, 2000.

[5] M. J. Bhagwat and J. G. Leishman, "On the aerodynamic stability of helicopter rotor wakes," in *American Helicopter Society 56th Annual Forum, Virginia Beach, VA*, pp. 2–4, 2000.

[6] M. J. Bhagwat and J. G. Leishman, "Time-accurate free-vortex wake model for dynamic rotor response," in *Proceedings of the Specialist Meeting of the American Helicopter Society*, 2000.

[7] M. J. Bhagwat and J. G. Leishman, "Transient rotor inflow using a time-accurate free-vortex wake model," 2001.

[8] M. J. Bhagwat and J. G. Leishman, "Rotor aerodynamics during maneuvering flight using a time-accurate free-vortex wake," *Journal of the American Helicopter Society*, vol. 48, no. 3, pp. 143–158, 2003.

[9] M. Gennaretti, J. Serafini, P. Masarati, and G. Quaranta, "Effects of biodynamic feedthrough in rotorcraft/pilot coupling: collective bounce case," *Journal of Guidance, Control, and Dynamics*, 2013.

[10] J. Serafini, M. Gennaretti, P. Masarati, G. Quaranta, and O. Dieterich, "Aeroelastic and biodynamic modelling for stability analysis of rotorcraft-pilot coupling phenomena," 2008.

[11] V. Muscarello, G. Quaranta, P. Masarati, L. Lu, M. Jones, and M. Jump, "Prediction and simulator verification of roll/lateral adverse aeroservoelastic rotorcraft–pilot couplings," *Journal of Guidance, Control, and Dynamics*, 2015.

[12] D. M. Pitt and D. A. Peters, "Theoretical prediction of dynamic-inflow derivatives," 1980.

[13] W. Kinner, "Die kreisförmige tragfläche auf potentialtheoretischer grundlage," *Ingenieur-Archiv*, vol. 8, no. 1, pp. 47–80, 1937.

[14] K. Mangler and B. Squire, "Calculation of the induced velocity field of a rotor," *Report (Aero12247, Royal Aircraft Esta February*, 1948.

[15] P. J. Carpenter and B. Fridovich, "Effect of a rapid blade-pitch increase on the thrust and induced-velocity response of a full-scale helicopter rotor," 1953.

[16] D. A. Peters, "How dynamic inflow survives in the competitive world of rotorcraft aerodynamics," *Journal of the American Helicopter Society*, vol. 54, no. 1, pp. 11001–11001, 2009.

[17] M. M. Munk, "Some tables of the factor of apparent additional mass," 1924.

[18] D. A. Peters and C. J. He, "Finite state induced flow models part ii: three-dimensional rotor disk," *Journal of Aircraft*, vol. 32, no. 2, pp. 323–333, 1995.

[19] C. He, "Development and application of a generalized dynamic wake theory for lifting rotors," 1989.

[20] M. Takahashi, "A flight-dynamic helicopter mathematical model with single flap-lag-torsion main rotor. nasa tm-102267," *National Aeronautics and Space Administration, Washington, DC*, 1990.

[21] M. Chaimovich, A. Rosen, O. Rand, M. Mansur, and M. Tischler, "Investigation of the flight mechanics simulation of a hovering helicopter," 1992.

[22] I. A. Simons and A. N. Modha, "Gyroscopic feathering moments and the âĂIJbell stabilizer barâĂİ on helicopter rotors," *Journal of the American Helicopter Society*, vol. 52, no. 1, pp. 69–74, 2007.

[23] A. Rosen and A. Isser, "A new model of rotor dynamics during pitch and roll of a hovering helicopter," *Journal of the American Helicopter Society*, vol. 40, no. 3, pp. 17–28, 1995.

[24] J. Zhao, *Dynamic wake distortion model for helicopter maneuvering flight*. PhD thesis, Georgia Institute of Technology, 2005.

[25] R. E. Brown, "Rotor wake modeling for flight dynamic simulation of helicopters," *AIAA journal*, vol. 38, no. 1, pp. 57–63, 2000.

[26] J. Prasad, M. Nowak, and H. Xin, "Finite state inflow models for a coaxial rotor in hover," 2012.

[27] M. Innocenti, "Helicopter flight dynamics: The theory and application of flying qualities and simulation modeling," *Journal of Guidance, Control, and Dynamics*, vol. 22, no. 2, pp. 383–384, 1999.

[28] M. Gennaretti and G. Bernardini, "Aeroacousto-elastic modeling for response analysis of helicopter rotors," in *Variational Analysis and Aerospace Engineering: Mathematical Challenges for Aerospace Design*, pp. 27–50, Springer, 2012.

[29] J. M. Greenberg, "Airfoil in sinusoidal motion in a pulsating stream," 1947.

[30] M. Gennaretti, M. M. Colella, and G. Bernardini, "Prediction of tiltrotor vibratory loads with inclusion of wing-proprotor aerodynamic interaction," *Journal of Aircraft*, vol. 47, no. 1, pp. 71–79, 2010.

[31] R. Gori, M. Gennaretti, M. D. Pavel, O. Stroosma, and I. Miletovic, "Prediction and simulator verification of state-space rotor modelling on helicopter manoeuvring flight," *Proceedings of the 41st European Rotorcraft Rorum 2015, Munich (Germany), Sept. 1-4, 2015*, 2015.

[32] L. A. Zadeh and C. A. Deoser, *Linear system theory*. Robert E. Krieger Publishing Company Huntington, 1976.

[33] L. A. Zadeh, "Frequency analysis of variable networks," *Proceedings of the IRE*, vol. 38, no. 3, pp. 291–299, 1950.

[34] W. Johnson, "Helicopter theory, 1994," 1990.

[35] M. Gennaretti and D. Muro, "Multiblade reduced-order aerodynamics for state-space aeroelastic modeling of rotors," *Journal of Aircraft*, vol. 49, no. 2, pp. 495–502, 2012.

[36] R. Gori, J. Serafini, M. M. Colella, and M. Gennaretti, "Assessment of a state-space aeroelastic rotor model for rotorcraft flight dynamics," *CEAS Aeronautical Journal*, vol. 7, no. 3, pp. 405–418, 2016.

[37] J. Serafini, M. M. Colella, and M. Gennaretti, "A finite-state aeroelastic model for rotorcraft–pilot coupling analysis," *CEAS Aeronautical Journal*, vol. 5, no. 1, pp. 1–11, 2014.

[38] L. Ljung, *System identification*. Wiley Online Library, 1999.

[39] L. Rabiner, R. W. Schafer, and C. Rader, "The chirp z-transform algorithm," *IEEE transactions on audio and electroacoustics*, vol. 17, no. 2, pp. 86–92, 1969.

[40] M. B. Tischler and R. K. Remple, "Aircraft and rotorcraft system identification," *AIAA education series*, 2006.

[41] S. J. Shin, C. E. Cesnik, and S. R. Hall, "System identification technique for active helicopter rotors," *Journal of Intelligent Material Systems and Structures*, vol. 16, no. 11-12, pp. 1025–1038, 2005.

[42] A. Siddiqi, *Identification of the harmonic transfer functions of a helicopter rotor*. PhD thesis, Massachusetts Institute of Technology, 2001.

[43] A. J. Landgrebe, "An analytical method for predicting rotor wake geometry," *Journal of the American Helicopter Society*, vol. 14, no. 4, pp. 20–32, 1969.

[44] D. M. Pitt, "Rotor dynamic inflow derivatives and time constants from various inflow models.," tech. rep., ARMY TROOP SUPPORT AND AVIATION MATERIEL READINESS COMMAND ST LOUIS MO, 1980.

[45] U. T. Arnold, J. D. Keller, H. Curtiss, G. Reichert, *et al.*, "The effect of inflow models on the predicted response of helicopters," *Journal of the American Helicopter Society*, vol. 43, no. 1, pp. 25–36, 1998.

[46] L. Morino and A. Ferrante, "A method for evaluating an aerodynamic-matrix reduced-order model," in *Atti del XVIII Congresso Nazionale AIDAA, Volterra, Italy, September 19-22, 2005*, AIDAA, 2005.

[47] D. F. Shanno, "Conditioning of quasi-newton methods for function minimization," *Mathematics of computation*, vol. 24, no. 111, pp. 647–656, 1970.

[48] M. Gennaretti and G. Bernardini, "Novel boundary integral formulation for blade-vortex interaction aerodynamics of helicopter rotors," *AIAA journal*, vol. 45, no. 6, p. 1169, 2007.

[49] G. Bernardini, J. Serafini, M. M. Colella, and M. Gennaretti, "Analysis of a structural-aerodynamic fully-coupled formulation for aeroelastic response of rotorcraft," *Aerospace Science and Technology*, vol. 29, no. 1, pp. 175–184, 2013.

[50] M. Gennaretti, M. M. Colella, J. Serafini, B. Dang-Vu, P. Masarati, G. Quaranta, V. Muscarello, M. Jump, M. Jones, L. Lu, A. Ionita, I. Fuiorea, M. Mihaila-Andres,

and R. Stefan, "Anatomy, modelling and prediction of aeroservoelastic rotorcraft-pilot-coupling," in *Proceedings of 39th European Rotorcraft Forum*, (Moscow (Russia)), September 2013.

[51] J. Serafini, M. M. Colella, and M. Gennaretti, "A finite-state aeroelastic model for rotorcraft–pilot coupling analysis," *CEAS Aeronautical Journal*, vol. 5, no. 1, pp. 1–11, 2014.